Old Dominion University

ODU Digital Commons

Electrical & Computer Engineering Theses & Dissertations

Electrical & Computer Engineering

Fall 1996

Monte Carlo Simulations of Photoemission Characteristics from GaAs and Diamond

Abhishek Srivastava
Old Dominion University

Follow this and additional works at: https://digitalcommons.odu.edu/ece_etds

Part of the Computational Engineering Commons, Electrical and Computer Engineering Commons, Materials Science and Engineering Commons, Numerical Analysis and Scientific Computing Commons, and the Theory and Algorithms Commons

Recommended Citation

Srivastava, Abhishek. "Monte Carlo Simulations of Photoemission Characteristics from GaAs and Diamond" (1996). Master of Science (MS), Thesis, Electrical & Computer Engineering, Old Dominion University, DOI: 10.25777/akvy-zt53
https://digitalcommons.odu.edu/ece_etds/534

This Thesis is brought to you for free and open access by the Electrical & Computer Engineering at ODU Digital Commons. It has been accepted for inclusion in Electrical & Computer Engineering Theses & Dissertations by an authorized administrator of ODU Digital Commons. For more information, please contact digitalcommons@odu.edu.

MONTE CARLO SIMULATIONS OF PHOTOEMISSION CHARACTERISTICS FROM GaAs AND DIAMOND

by

Abhishek Srivastava
B.Tech in Electrical Engineering
Indian Institute of Technology, Bombay, INDIA

A Thesis Submitted to the Faculty of
Old Dominion University in Partial Fulfillment of the
Requirements for the Degree of

MASTER OF SCIENCE

ELECTRICAL ENGINEERING

OLD DOMINION UNIVERSITY

December, 1996

Approved by:

____
Dr. R. P. Joshi

____
Dr. L. L. Vahala

____
Dr. A. N. Dharamsi

MONTE CARLO SIMULATIONS OF PHOTOEMISSION CHARACTERISTICS FROM GaAs AND DIAMOND

ABSTRACT

Monte Carlo based numerical simulations were performed to study photoemission from GaAs and diamond. The central goal was to assess the potential for NEA photoemission from diamond, and to predict its characteristics. The GaAs material system was also included in the simulation study to provide: (i) calibration and validation of the numerical model developed by carefully matching the simulation results with available experimental data, and (ii) quantitative comparisons between the response characteristics of diamond and the better known GaAs system.

Predictions of the energy distribution, temporal response and angular distribution of emitted electrons were obtained. Effects of various parameters, such as the sample doping, material thickness, pulse width and excitation energy, on the characteristics were analyzed and predicted. The results for Cesium coated GaAs were in good agreement with the available experimental data. The emission flux for diamond was found to be substantially lower. The simulations suggest that diamond will be a poor candidate for applications requiring the production of short electron pulses on sub-nanosecond time-scales. The reduced electronic emission primarily resulted from a low surface transmission probability, and the much longer characteristic absorption length.

ACKNOWLEDGEMENTS

I take this opportunity to express my sincere gratitude to my advisor, Dr. Ravindra P. Joshi for his guidance, encouragement, and continual support during the course of my graduate studies at Old Dominion University. His help, patience, and friendship have made my education a truly rewarding experience. I also wish to thank Dr. L. L. Vahala and Dr. A. N. Dharamsi for serving on my thesis committee.

I would also like to thank all my friends, especially my roommates Srinivas Naikoti, Chandrasekhar Potluri and Ritesh Saxena, for making my stay at ODU a memorable one. A special thanks also goes to all my friends back home for keeping the long distance friendship up.

Finally, I would like to thank my family, without whose love and support, I could never have completed my education.

TABLE OF CONTENTS

Page

List of Tables vii

List of Figures viii

Chapter

1. Introduction 1

2. Literature Survey 6

2.1 Introduction 6

2.2 Photoemission from Semiconductors 6

2.3 Lowering the Work Function 7

2.3.1 Formation of Heterojunction 9

2.3.2 Surface Dipole 11

2.4 NEA Semiconductor Photoemitter 11

2.4.1 NEA and Conventional Electron Emitters 13

2.4.2 Some NEA Based Device Configurations 15

2.5 Potential for Diamond 20

2.6 Advances in Diamond Growth 21

2.7 Summary of Previous Experimental Work 22

2.8 Review of Related Simulations 25

2.9 Problem Definition and Research Issues 28

3. Numerical Simulation Scheme ... 32
3.1 Introduction ... 32
3.2 The Monte Carlo Method ... 34
3.2.1 Definition of the Physical System ... 36
3.2.2 Initial Conditions ... 36
3.2.3 Flight Duration ... 38
3.2.4 Free Flight ... 40
3.2.5 Choice of the Scattering Mechanism ... 41
3.2.6 Choice of State After Scattering ... 41
3.2.7 Collection of Results ... 45
3.3 Implementation of the Monte Carlo Technique ... 45
3.4 Quantum Mechanical Reflection at Surfaces ... 52
3.5 Scattering Mechanisms in GaAs and Diamond ... 53
3.5.1 General Theory ... 53
3.5.2 Acoustic Phonon Scattering ... 56
3.5.3 Polar Optical Scattering ... 56
3.5.4 Non-Polar Optical Phonon Scattering ... 57
3.5.5 Intervalley Phonon Scattering ... 57
3.5.6 Ionized Impurity Scattering ... 58
3.6 Grain Boundary Scattering in Polycrystalline Diamond ... 59
3.7 Orientation Dependence ... 62

4. Results and Discussion 65

4.1 Introduction 65

4.2 Results for GaAs 65

4.2.1 Electron Energy Distributions 66

4.2.2 Temporal Response Characteristics 76

4.2.3 Angular Response 85

4.3 Simulation Results for Diamond 88

4.3.1 Grain Boundary Effects in Polycrystalline Diamond . . . 88

4.3.2 Simulation Results for Diamond Photoemission 92

4.4 Discussion and Result Summary 100

5. Conclusions 103

5.1 Research Summary 103

5.2 Scope for Future Work 108

References 109

Appendix A I

LIST OF TABLES

Table Page

2.1 Input data used in simulation work by Yang *et al* 27

3.1 Parameter values used for GaAs in simulation 48

3.2 Parameter values used for diamond in simulation 49

LIST OF FIGURES

Figure		Page
2.1	Photoemission originating from valence band, conduction band and surface states	8
2.2	The heterojunction between Cs-O and p+ GaAs	10
2.3	Energy band diagram for GaAs/Cs-O surface: Double dipole model with thin Cs-O layer	12
2.4	Energy band diagram of a p-GaAs/Cs-O NEA photoemitter	12
2.5	GaAs experimental quantum yield curves measured during the activation of p-GaAs to NEA	14
2.6	Quantum efficiency of several conventional emitters as compared to NEA GaAs	16
2.7(a)	Simple p-n homojunction cold cathode energy band diagram under bias conditions	18
2.7(b)	Energy band diagram for a Ag/p-InP transferred electron (TE) cathode	18
2.7(c)	Energy band diagram for a Ag/InGaP direct emitter TE cathode under bias conditions	19
2.7(d)	Energy band diagram of a heterojunction TE cathode	19
2.8	EDC and EDC derivatives of electrons emitted from NEA GaAs at 300 K	24
2.9	EDC and EDC derivatives at 120 K	24

2.10 EDC's at 300 and 120 K for $h\nu = 1.65$ eV 26

2.11 EDC time evolution 26

2.12 Quantum photoyield from natural diamond (111) surface 26

2.13 Calculated and measured quantum efficiency curves for transmission GaAs photocathode 27

2.14 Simulated TTS of emitted electrons for 50nm thick transmission GaAs photocathode 29

2.15 Photoelectron spectra of transmission mode GaAs photocathode of thickness 2000, 150 and 40 nm 29

3.1 Flow chart of simple Ensemble Monte Carlo program 37

3.2 Flow chart of scattering mechanism selection in MC simulations 42

3.3 Geometry for determining the wave vector **k** after scattering in 3 - dimensional simulation 44

3.4 Flow chart of the implementation of MC program for study of photoemission 46

3.5 Constant energy surfaces in first Brillouin zone for GaAs and diamond 64

3.6 Different shapes of constant energy surfaces and their E-k relationships 64

4.1 Energy distribution (ED) for reflective mode (RM) at 300K for sample thickness of 10μm, photon energy of 1.55eV and pulse width of 0.05 ps 67

4.2 Energy distribution for RM for sample doping of 5×10^{18} cm $^{-3}$ and pulse width of 0.05 ps 69

4.3 Energy distribution for reflective mode for thickness of 10μm 70

4.4 ED for transmission mode (TM) for sample thickness of 1μm and pulse width of 0.01 ps 72

4.5 ED for TM for sample doping of 1×10^{18} cm $^{-3}$ 73

4.6 ED for TM for sample thickness of 1μm 75

4.7 Effect of doping on temporal response (TR) for a 10μm thick sample in reflective mode 77

4.8 Effect of sample thickness on TR for sample in RM 79

4.9 Effect of pulse width on TR for 25μm sample in RM 79

4.10 Impact of increasing pulse energy on TR in reflective mode 80

4.11 Effect of doping on TR from a 1μm sample in TM 82

4.12 Effect of varying sample thickness on TR in case of TM 82

4.13 Effect of varying sample thickness on TR in case of TM 83

4.14 Effect of pulse energy on TR for a 10 μm sample in TM 84

4.15 Comparison of TR of a sample in RM and TM 86

4.16 Angular distribution for 10 μm sample in RM 87

4.17 Angular distribution for 2 μm sample in TM 87

4.18 Drift velocity variation with electric field 90

4.19 Drift velocity variation with temperature 91

4.20 Transient response of drift velocity 93

4.21 ED from diamond for sample thickness of 1 μm and 0.1eV energy barrier 95

4.22 ED for sample thickness of 1 μm and zero energy barrier 97

4.23 Temporal response (TR) for energy barrier of 0.1 eV 98

4.24 TR for zero energy barrier 99

A.1 Transmission probability as a functin of electron energy VI

CHAPTER 1

INTRODUCTION

Photoemission has played an important role in modern science and technology. Einstein's explanation of photoemission in terms of quantized light provided one of the foundations for quantum theory. Photomultipliers and photodiodes have played essential roles in sensor and detector applications, and other fields of scientific investigations. Innumerable practical engineering devices ranging from simple optical relays to sophisticated television camera tubes have utilized photoemission. The efficiency of the process of photoemission has been dramatically improved through the advent of negative electron affinity (NEA) materials. Semiconductors with NEA surfaces are used as photoemitters, secondary emitters, and cold cathode emitters. In recent years applications of NEA photoemitters have been the subject of intensive research throughout the world.

Photoemission of electrons from a solid is a three step process and involves the following sequence:

(1) absorption of a photon and creation of an electron-hole pair,

(2) transport of the electron to the surface, and

(3) the emission of electron by passage through the surface layers and eventual escape into the vacuum.

The conditions for efficient photoemission from a solid are:

(a) The optical absorption coefficient should be high, so that incoming photons can be absorbed as close to the surface as possible. The excited electrons can then escape before making too many collisions, with the lattice atoms or with other electrons.

(b) Incoming photons should excite the electrons high into the conduction band, well above the vacuum level, so that they can escape even after losing energy during internal collisions. An additional advantage of high energy excitation is that it enhances the absorption coefficient.

(c) The probability of energy losing collisions should be minimized. Electron-electron collision effects should be avoided by using a semiconductor rather than a metal. Lower temperatures would help in reducing the electron-phonon scattering.

(d) The electron affinity should be low, to increase the number of electrons able to escape.

(e) The work function should be high, to reduce emission of electrons from filled states by purely thermal excitation.

These requirements can be met in a p-type semiconductor with a direct bandgap, like GaAs. The direct nature of the bandgap allows a sharp onset of optical absorption for photon energies just above the gap energy.

The photoemission efficiency can be drastically improved if the electron affinity can be reduced to zero or negative values. This is usually achieved by lowering the work function by adsorption of a few layers of cesium and oxygen onto the material surface. Once the work function is lowered to such an extent that the vacuum level outside the material drops below the conduction level within the bulk material, the material becomes NEA. Once the affinity is lowered to zero or negative values, the whole character of electron transport mechanism changes, from "hot-electron" transport to "minority-carrier" diffusion. For a positive affinity emitter, the electron reaches the surface by a necessarily brief random walk process, with a short mean free path of a few tens of Å in a semiconductor, and even less in a metal. The distance (escape depth) which the average hot electron can diffuse before its energy falls

below the vacuum level is therefore low. The escape depth for a positive affinity emitter is typically a few hundred Å. The equivalent lifetime during which a hot electron can hope to escape from a positive affinity emitter is less than a picosecond. In the negative affinity case, by contrast, the electrons can come to equilibrium in a set of metastable levels - the conduction band minima - where their lifetime may be limited only by recombination with holes. These lifetimes may be much longer, typically of the order of a nanosecond in the Γ-minimum for GaAs. This leads to much greater escape depths, typically of the order of a few μm. This results in much higher quantum efficiency for photoemission from NEA semiconductors. Cesium coated GaAs is the most commonly used material for NEA photoemission applications. Some other materials, like diamond, are inherently NEA and hence do not require Cs coating.

The photoemission can be made to occur either in the reflective or the transmission modes. In case of a reflective mode device, light is incident on the electron emitting surface of the photoemitter. On the other hand, light is incident on the back or substrate (non-emitting) side for the transmission mode. Photoemission yields are much better in the reflective mode, since electrons are generated close to the emitting surface and so can reach the boundary without losing much energy. The electrical response of the photoemitter is also faster, since electrons require less time to get emitted. For transmission mode, however, the emission yield is lower as the electrons are generated near the non-emitting surface and they need to travel the entire width of the sample in order to reach the emission boundary, losing much of their excess energy in the process. The response is also slower because of the time required for electron transport to the emission surface.

Aim of this project was to study photoemission from GaAs and diamond using Monte Carlo simulations. The central goal was to assess the potential for NEA photoemission from diamond, and to predict its characteristics. To facilitate meaningful comparisons, similar simulations were carried out for both diamond and GaAs. Simulations for GaAs also served as a validity check for the Monte Carlo model developed here. The numerical predictions were compared against actual available experimental data as a benchmark. Diamond has been studied as a potential material for NEA photoemission applications because of its well known desirable properties, like hardness, high thermal conductivity, high band gap, and radiation hardness, which can make diamond NEA devices extremely robust and stable.

Chapter 2 is a literature survey of the previous research work done in the field of NEA photoemission from GaAs and diamond. Results of some experimental and simulation work carried out in this field have been presented. The chapter also contains a brief discussion of the theory behind the phenomenon of photoemission. In chapter 3, the principles of Monte Carlo (MC) method, applied to the study of semiconductors, are introduced. The general features of MC algorithm used for self consistent simulation of semiconductor devices are thoroughly discussed. There is a detailed explanation of the implementation of the algorithms for simulation of photoemission. The chapter also contains a discussion on the scattering mechanisms involved in electron transport in semiconductors. The role of grain boundary scattering in the electronic transport characteristics in polycrystalline diamond has also been evaluated. Chapter 4 gives the results of Monte Carlo simulations. Specific characteristics of NEA photoemission, namely energy distribution, temporal response, and angular spread of the electron beam, have been analyzed. Effect of various physical parameters on the above characteristics have been studied. Potential of NEA

photoemission from diamond has also been assessed, and a comparison with GaAs-Cs photoemitters has been carried out. Chapter 5 contains a summary of the conclusions obtained for photoemission from GaAs and diamond based on the Monte Carlo simulations. Also, recommendations for future research, which could produce improvements in photoemission from diamond, have been outlined.

CHAPTER 2

LITERATURE SURVEY

2.1 INTRODUCTION

This chapter is an overview of the research work that has been done in the field of Negative Electron Affinity (NEA) photoemission. Development of semiconductor NEA devices has been discussed, with reference to the progress that have been made in this field over the past few decades. There is a brief discussion of the theory behind this phenomenon. Measured data on different NEA photoemission devices has also been provided. Discussions pertaining to the influence of various parameters on the characteristics of these devices have been given. We have examined the potential of using diamond as a possible source of electrons in the NEA devices, comparing it with GaAs. In the end, various research issues involved in getting an optimum performance for the NEA devices have been discussed.

2.2 PHOTOEMISSION FROM SEMICONDUCTORS

Photoemission from p-type semiconductors is the basis for most conventional (polycrystalline) and the newer (single-crystal) photoemissive devices. Semiconductor photoemission is conceptually a three-step process consisting of photoexcitation of an electron from a filled electron energy state to a an excited state above the vacuum level, transport to the surface, and escape over a surface barrier into vacuum [1,2].

In general, photoemission from a semiconductor can originate from filled valance band states within the flat band bulk or the space charge surface region, processes (1) and (2) in figure 2.1; or from conduction band states (bulk or near the surface) and the surface states,

processes (3) and (4) in figure 2.1. In almost all the cases, however, excitation from the valance band dominates. Even in the case of an N^+ semiconductor, the density of electron states in the conduction band is still small relative to the valance band. Photoemission from surface states has been observed [3] , but is also very small due to their local distribution in space (~10 - 20Å) and small density of these states (less than 10^{15} cm^{-2}). Similar arguments hold for emission from defects or deep levels.

As we can see from figure 2.1, the internal field within the band-bending region is more favorable for electron emission for p-type case, since the field tends to accelerate photoexcited electrons into vacuum rather than back into the bulk. Therefore, from the simple energy-band model semiconductor photoemission, p-type semiconductors will have a lower photon energy (longer wavelength) threshold response and will likely have a higher magnitude of yield than n-type semiconductors [4].

2.3 LOWERING THE WORK FUNCTION

Due to high values of work function of metals and semiconductors, these simple solids in themselves are incapable of photoemission in the visible or infrared region of the spectrum, i.e., $h\nu = 1.0\text{-}3.0$ eV. However, adsorption of approximately a monolayer thickness of cesium onto the atomically cleaned surface of most metals and semiconductors dramatically lowers the work function to ~1.6 eV. Although cesium is the most effective element in lowering the work function, other alkali metals, like lithium, sodium, potassium, and rubidium, are also effective [5]. It has also been known for a long time that theadsorption of small amounts of oxygen onto a cesiated surface can reduce the work function slightly further [6]. Therefore, in order to achieve the NEA condition, the work function of a

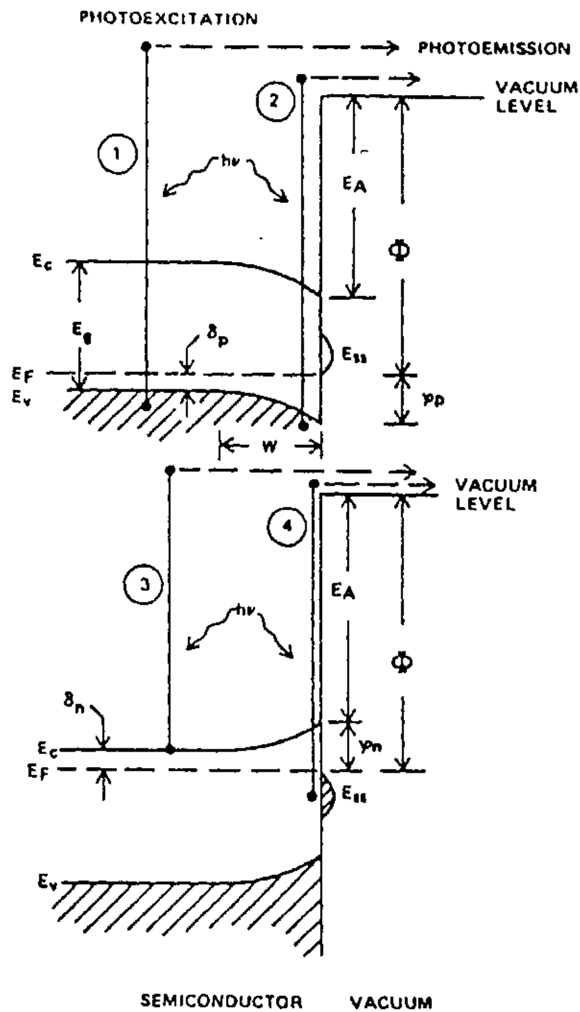

Fig. 2.1 Photoemission originating from valence band, conduction band and surface states

semiconductor is reduced by the adsorption of Cs, and in some cases by a combination of Cs and O, to the atomically clean surfaces - the process is called "activation" of the surface. The most commonly used semiconductors are III-V compounds and silicon. III-V compounds are usually cleaned by vacuum heat treatments. Once the surface is atomically cleaned, the adsorbates are added in monolayer quantities. About one monolayer of Cs is sufficient to achieve NEA on GaP. For GaAs, both Cs and O_2 are required to obtain the most sensitive NEA surfaces [7]. These two elements can be added alternatively or simultaneously. The adsorbed Cs-O is 2 to 3 atomic layers thick [8]. The relative amounts of Cs and O_2 added during activation process are determined empirically by the magnitude of the photoemission, and the adsorbates are deposited until a maximum in the photoresponse is reached.

For the III-V NEA emitters, there are two models for the mechanisms of work function reduction. These are briefly discussed below.

2.3.1 FORMATION OF HETEROJUNCTION

In this model, Cs-O layer is assumed to have the characteristics of bulk n-type Cs_2O [9]. The utilization of many monolayer Cs_2O coating implies the necessity to consider the solid-solid heterojunction which exists at the interface with the substrate. The band profiles of the Cs_2O and the substrate (Cs covered GaAs) adjust at the interface so as to satisfy equilibrium charge conditions, as shown schematically in figure 2.2(a) and 2.2(b). In the absence of appreciable densities of states near the midgap in Cs_2O, it is readily seen that energy V_b in figure 2.2 (b) is given by: $V_b = \phi_{Cs} - \chi_{Cs2O}$ which is of the order of 1.0 eV. For p-type GaAs this is lower than the bandgap, and the heterojunction barrier therefore does not

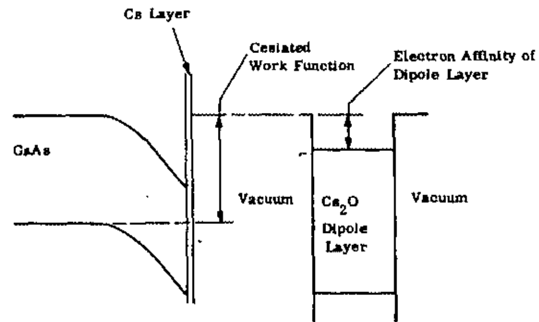

(a)

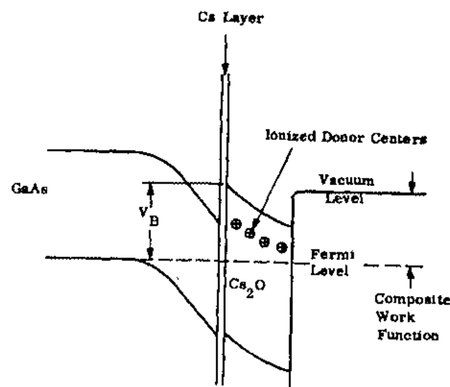

(b)

Fig. 2.2 The heterojunction between Cs_2O and p+ GaAs

(a) Approach of Cs_2O layer to cesiated GaAs surface

(b) Resulting heterojunction model of the photoemitter

noticeably interfere with photoemission from GaAs/Cs_2O. Bulk generated electrons must either overcome or tunnel through this barrier. Once in the Cs_2O, they can be emitted as "hot" electrons over the small 0.4 - 0.6 eV positive electron affinity barrier of the Cs_2O. This model, however, cannot be applied in case of a monolayer Cs-O deposition.

2.3.2 SURFACE DIPOLE

According to this model, NEA is achieved through a surface double dipole mechanism [10], as shown schematically in figure 2.3. The initially adsorbed Cs atoms, being highly electropositive, readily give up their valance electrons to the substrate. There is an image charge induced in the substrate from the positive ions on the surface producing a dipole layer, thereby lowering the work function. In this model, the dipole thickness (~8 Å) is consistent with the monolayer dimension of the Cs-O layer.

2.4 NEA SEMICONDUCTOR PHOTOEMITTER

The NEA semiconductor photoemitter is a P^+ semiconductor with $E_g > 1.0$ eV whose atomically clean surface been suitably activated with cesium and oxygen to reduce the work function below the level of the conduction band in the bulk. figure 2.4 shows a schematic diagram of a NEA photoemitter. The p-type doping concentration is kept nearly degenerate (~10^{18}-10^{19} cm^{-3}), so that the band bending region width "W" is on the order of the optical-phonon mean free path, ~< 100 Å. As a result, photoexcited electrons which thermalized into quasiequilibrium in the lowest conduction band minimum (e.g., Γ in GaAs) near the surface can escape. These electrons dominate the photoemission threshold yield. The photoelectron escape depth is no longer limited by the hot-electron scattering length L_e, but rather the

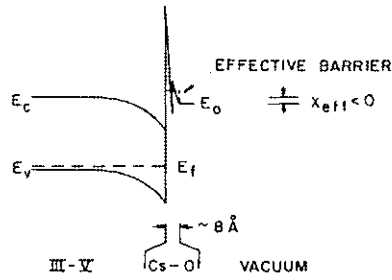

Fig. 2.3 Energy band diagram for GaAs/Cs-O surface: Double dipole model with thin (~8Å) Cs-O laler

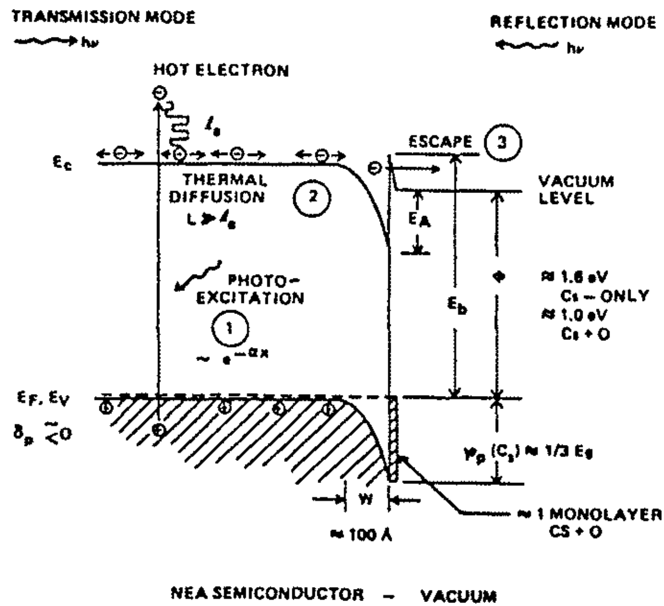

Fig. 2.4 Schematic energy-band diagram of a p-GaAs/Cs-O NEA photoemitter

minority carrier diffusion length "L". The increase in escape depth leads to higher quantum yield. The activation of p+ GaAs to NEA is shown in the experimental reflection mode quantum yield curves in figure 2.5.

The earliest developments of the NEA semiconductor photoemitters, covering the period from about 1965 to 1973 are reviewed in a number of articles [11-13]. Review articles by Martinelli and Fisher [14] cover most of the developmental NEA devices. The influence of surface electronic structures, together with results on some devices, are summarized by Spicer [15].

2.4.1 NEA AND CONVENTIONAL ELECTRON EMITTERS

In case of conventional electron emitters, photons excite electrons from the valence band into the conduction band, and the energy of the electrons must be greater than the vacuum level if they are to escape into vacuum. The photothreshold for this emitter is $X + E_g$. The excited electrons migrate to the surface, losing energy to the lattice through collisions at the rate of about 50 meV per collision with mean free paths between collisions of 25 to 50 Å. Therefore, to reach the surface before losing 1 eV, for example, the excited electrons can make only 20 collisions. This means that, if they execute a random walk to the surface, their escape depth is of the order of 100 Å. The escape depth depends on the excitation energy of the radiation, the details of the absorption process, and the energy dependence of the transport process, with the typical value being a few hundred angstroms for conventional cathodes [16].

In NEA cathodes, the excited electron loses energy to the lattice while travelling a mean distance of a few hundred angstroms, decaying in energy to the bottom of the

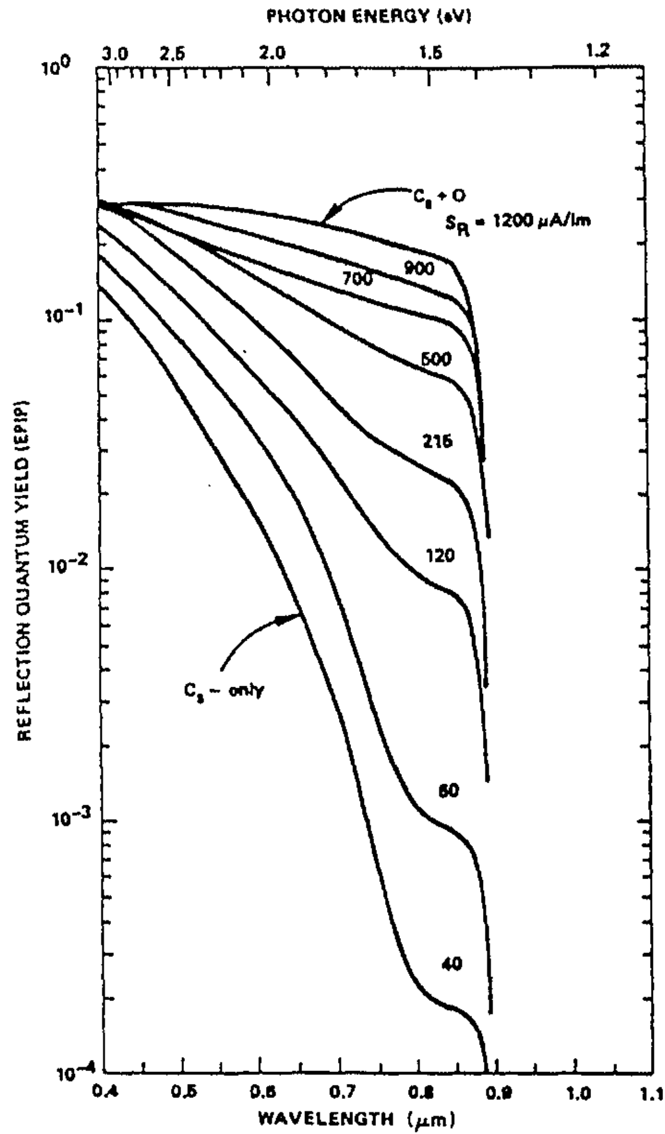

Fig. 2.5 GaAs experimental quantum yield curves measured during the activation of p-GaAs to NEA

conduction band. At this point, the electron is in thermal equilibrium with the lattice. Thermalized minority electrons survive for relatively long times before they recombine across the band gap. During this time, known as minority electron lifetime τ, the electron diffuses over distances "L" as long as several micrometers. These diffusion lengths are several orders of magnitude longer than the escape depths for conventional emitters, and herein lies one of the great advantages of NEA emitters. Electrons diffuse to the NEA surface from relatively deep in the material and escape into vacuum, thus increasing the emission efficiency in regions of the spectrum where optical absorption is weak. Figure 2.6 compares the quantum efficiency (emitted electrons per incident photon) of several conventional emitters with NEA GaAs [17]. The NEA cathode has a higher quantum efficiency throughout the visible and near the infra-red (IR) region.

2.4.2 SOME NEA BASED DEVICE CONFIGURATIONS

A variety of device structures which utilize the NEA concept have been proposed and developed [14,18]. These devices were designed for photo-emission, as secondary electron emitters, or to function as cold-cathodes. NEA GaAs photomultipliers and Cs/p-GaAs dynodes have been available for a number of years. The NEA GaAs surface has also been found to be a good source of spin-polarized electrons with applications to spectroscopy. A number of heterojunction device structures based on III-V compounds have been realized as well. Four simple NEA device structures are given below as illustrative examples.

Figure 2.7(a) shows the energy band diagram of a simple p-n junction cold cathode [1]. The substrate is n-type and provides a source of electrons. Under forward bias, electrons are injected from the substrate into a thin p-type emitter region which has an activated NEA

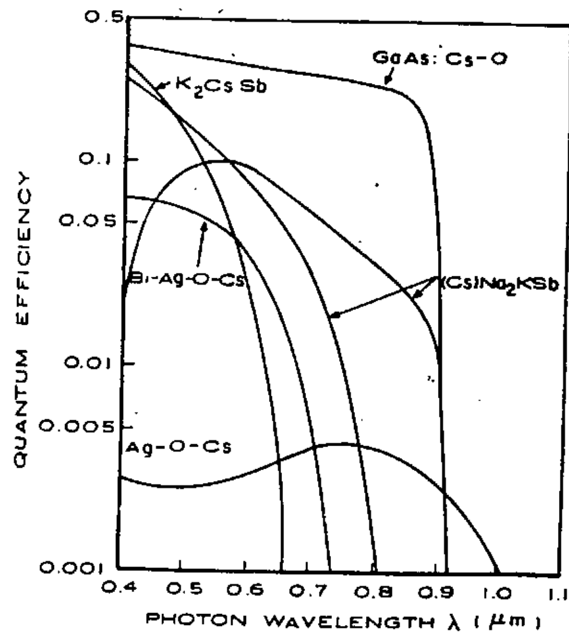

Fig. 2.6 Quantum efficiency of several conventional emitters as compared to NEA GaAs

surface. If the p-region is made sufficiently thin (about the diffusion length), then a large fraction of the injected electrons are able to diffuse-drift and be emitted into the vacuum. Another device scheme involves bias-assisted photoemission [18] as shown in figure 2.7b. This approach for long wavelength emission is based on the fact that electrons generated in certain III-V semiconductors (such as InP, InGaAsP alloys, and GaAs) can be promoted to upper conduction band valleys in the presence of an applied field. In the energy-band diagram of figure 2.7(b), photoexcited electrons are generated in the InP bulk by photons incident upon a thin semi-transparent Schottky barrier. Some of these minority carriers diffuse to the InP/Ag interface, where most are collected by the surface Schottky contact. However, on application of a reverse bias at the Schottky contact, a small fraction of the photogenerated electrons can be made to escape into the vacuum. Finally, the concept of a heterojunction NEA based electron emitter [1] is shown schematically in figure 2.7(c). A bias is applied as before, to induce field-assisted electron emission. Photons are absorbed within the InP region at the back. The heterojunction serves to provide an additional build-in field to accelerate the minority electrons towards the surface. Another device concept [1] shown in figure 2.7(d) utilizes a heterojunction to separate the device into photon absorbing and electron emitting regions. Ordinarily with no applied bias, the minority electrons are prevented from reaching the surface by the potential barrier at the heterojunction. However, applying a reverse bias facilitates the transport of minority electrons from the absorbing region towards the emitter; and also provides a surface field for emission.

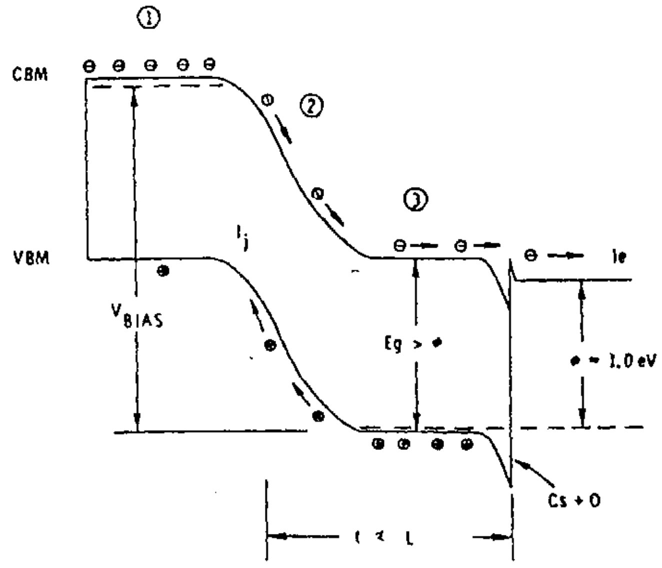

Fig. 2.7(a) Simple p-n homojunction cold cathode energy band diagram under bias conditions

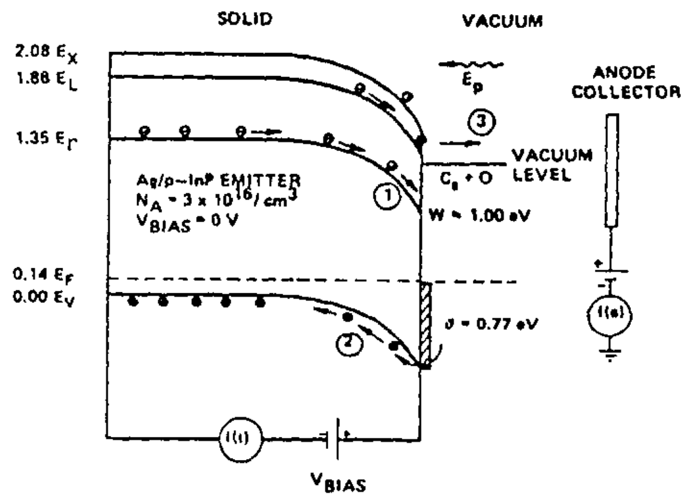

Fig. 2.7(b) Schematic energy band diagram for a Ag/p-InP transferred electron (TE) cathode

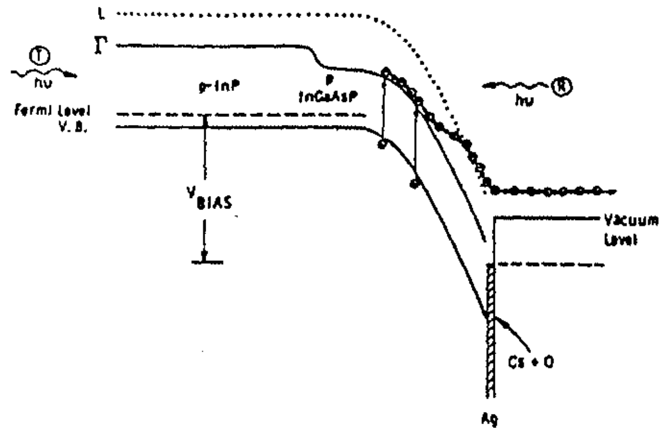

Fig. 2.7(c) Energy band diagram for a Ag/InGaP direct emitter TE cathode under bias conditions

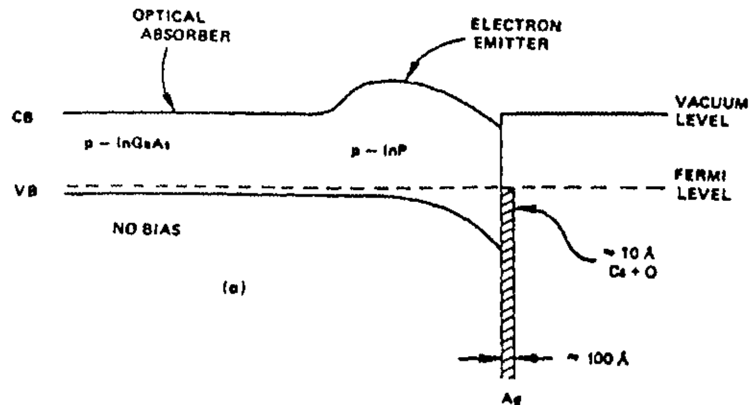

Fig. 2.7(d) Energy band diagram of a heterojunction TE cathode

2.5 POTENTIAL FOR DIAMOND

In the past few years, researchers have started looking towards diamond as a potential material for NEA photoemission applications. Diamond has several well known desirable properties. It is the hardest known substance and is a better conductor of heat at room temperature than any other material [19]. But even more striking are its electrical properties and radiation hardness. It can be doped p-type [20] and grown with low trap densities and high carrier mobilities, making it a semiconductor. Its high band gap makes it ideal for high temperature and high voltage applications. Due to such properties, it is by far the most desirable material for high power electronic devices [21]. Diamond is also relatively unusual among semiconductors in its ability to form high-quality interfaces with silicon dioxide and several metals [19]. Due to these attributes, diamond NEA devices can be extremely robust and stable. They can be especially useful for defence and space applications which usually require operation under high temperature and radiation conditions. Diamond NEA photoemitters can also be used in electron guns for TV and computer monitors, as well as flat panel displays. Another possible use could be that as a photodetector. High band-gap of diamond will allow it selectively detect high energy radiation.

Although diamond looks a very promising material for NEA photoemitters due to its obvious advantages over GaAs and Si, it has yet to prove its usefulness in practical devices. Most of the relevant work is still in the experimental phase. We have also studied NEA photoemission in diamond using Monte Carlo simulation technique. The later chapters will give results of these studies, along with a comparison with those of GaAs devices.

2.6 ADVANCES IN DIAMOND GROWTH

As mentioned above, diamond is a promising material for many specialized electronic device applications due to its unique combination of physical and electrical properties. Most semiconducting devices are fabricated in single crystal material. Unfortunately, the high cost, limited availability and small size of natural or synthetic single crystal diamonds hinders the development of commercial homoepitaxial single crystal diamond devices. The state of affairs, however, is changing. During the past few years, researchers have developed a wide range of techniques for laying down diamond films ranging in thickness from more than a millimeter to as little as a few hundred atoms. Plasma enhanced chemical vapour deposition (CVD) is the most commonly used technique for this.

The breakthrough in synthesis of diamond was mainly a result of work by Soviet scientists in the late 1970's and early 1980's which indicated that gas activation techniques can greatly increase the growth rate of diamond while suppressing the graphite deposition. Derjaguin and Fedoseev [22] outlined three approaches to produce higher concentrations of atomic hydrogen than that resulting from the thermal dissociation of hydrocarbon hydrogen gases: catalytic, electric discharge, and heated tungston filament approaches. Since then, various techniques for low-pressure growth of diamond, such as RF or microwave plasma enhanced CVD and hot filament CVD have been developed [23,24]. All the techniques were based on generation of atomic hydrogen near the growing surface. The growth rate has steadily increased with the development of new techniques. These growth techniques can be grouped into four major categories [25]: (i) thermally activated CVD; (ii) high frequency plasma activated CVD; (iii) direct current (dc) discharge assisted CVD; and (iv) combustion flame growth. Besides these, several hybrid methods have been developed, like hot filament

CVD assisted by a RF plasma and hot filament and dc plasma co-enhanced CVD [25]. The objective of developing hybrid techniques is to take full advantage of each method with goals of large area deposition and rapid growth. However, the CVD films grown have been polycrystalline in nature and exhibit granular structure. The measured electrical properties of the CVD films have generally been inferior to those of natural diamond. The most important affect is on free carrier mobility due to the grain boundaries. Grain boundaries contain high densities of traps which capture carriers, resulting in a depletion region around the boundary and reduced free carrier concentration in the film. The build-up of charge at the grain boundary leads to the formation of a potential barrier, which reduces the mobility of free carriers crossing the grain boundary [26]. The free carrier mobilities in thin film diamond are therefore lower, and strongly dependent on grain size and film thickness [27].

Despite the tremendous progress in the last decade, the vapour phase diamond growth technology is still far from being capable of large scale commercialization to realize many of the attractive potential applications. Many issues and problems attendant to the CVD of diamond, as critically examined by Yarbrough and Messeir [28] remain to be solved.

2.7 SUMMARY OF PREVIOUS EXPERIMENTAL WORK

This section gives summarizing results of the experimental work carried out on GaAs and diamond NEA devices. The results have also been analysed briefly to give some insight into the photoemission process.

Photoemission from GaAs was reported in a pioneering study by James *et al.* [29]. They measured the energy distribution curves of the photoemitted electrons and deduced some transport properties of GaAs. Their experimental studies yield a benchmark against

which results of theoretical simulations can be compared. Predictions for GaAs obtained from our numerical model were matched with the measured data for purposes of validating the present simulation approach. Other experimental groups in the past, have studied NEA based emission of spin-polarized electrons from GaAs [30,31]. Experiments to determine the temporal response of photoemission and the transient shape of the emitted electronic packets have also been carried out for GaAs [32]. These results again provide a basis for comparing predictions of the numerical model developed in this thesis.

In the most recent detailed study, Drouhin *et al.* [33] investigated the energy distribution curves (EDC's) of the photoelectrons emitted from the (100) face of a p-type doped (~ 10^{19} cm^{-3}) GaAs crystal, activated to negative electron affinity in ultrahigh vacuum conditions. The study was performed at 300 and 120 K under well-focused Kr+ laser excitation and with a very high 20 meV, energy resolution. Figure 2.8 shows an EDC and its derivative recorded for a photon energy $h\nu = 2.18$ eV at 300 K. Electron energy is referred from the valance band maximum E_{tau}. An intense low energy peak is observed, lying at an energy lower than the bulk E_{tau} position. It is due to the electrons which, in bulk crystal, were thermalized at the bottom of the conduction band. The results for low temperature (120 K) have been shown in figure 2.9. At low temperature, all structures become sharper and as energy gain is much less probable than energy loss during a collision, a steep starting point is observed on the high energy side of the EDC derivative. Figure 2.10 gives EDC's at 300 K and 120 K for $h\nu = 1.65$ eV. The temperature variation of the "Tau peak" is evident from the graph. Very narrow EDC were seen to result under near-bandgap excitation at 120 K. Figure 2.11 shows EDC's obtained under the same experimental conditions as a function of

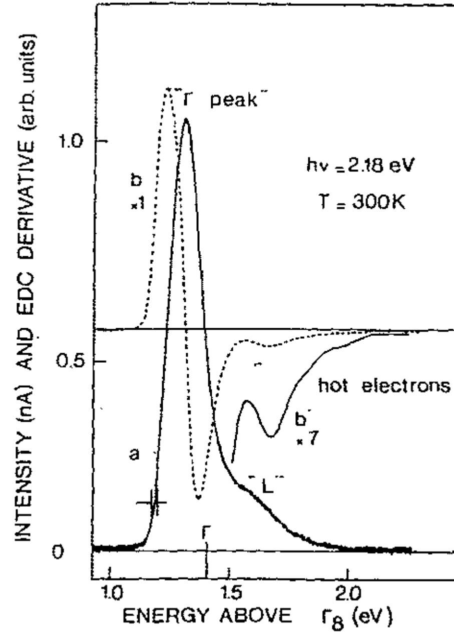

Fig. 2.8 EDC (curve a) and EDC derivatives (curves b and b') of electrons emitted from NEA GaAs at 300K

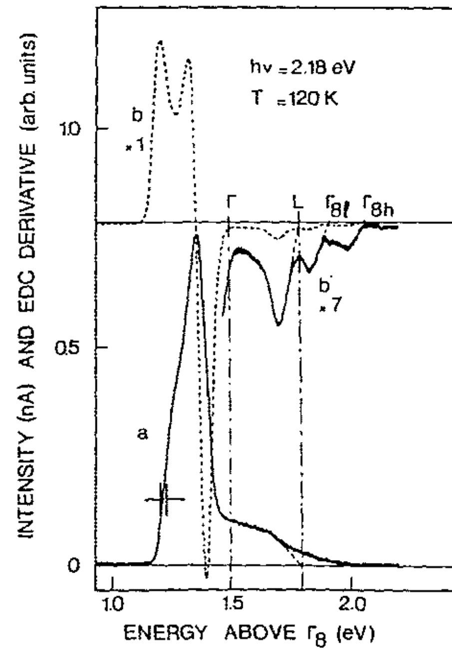

Fig. 2.9 EDC (curve a) and EDC derivatives (b and b') at 120K

time. The rise of electron affinity decreases the total current. This can be attributed either to cesium desorption or to surface pollution.

Himpsel *et al.* [34] studied NEA photoemission from an unreconstructed diamond (111) surface. They were the first to demonstrate the NEA property in diamond. Figure 2.12 shows the quantum yield obtained in the range $5 \leq h\nu \leq 35$ eV. Subsequent experimental studies on diamond focussed on "cold-cathode" emission based on its NEA property [35]. A comprehensive study on photoemission from diamond was reported very recently by Pate *et al.* [36]. They concluded that the emission process is the combined result of free electron-hole generation and excitonic formation during the photoexcitation process.

2.8 REVIEW OF RELATED SIMULATIONS

This section primarily discusses the previous Monte Carlo simulation work done in the context of GaAs NEA photoemitters. Historically though, drift-diffusion approaches were used to model electronic transport and emission from NEA material [37]. However, the drift diffusion methods are known to be inaccurate and to suffer from a number of simplifying assumptions. Only the Monte Carlo method provides accurate analysis of ultrafast transient phenomena, such as NEA based photoemission following pulsed laser excitation. Yang *et al.* [38] very recently were the first to perform such Monte Carlo simulations for NEA electronic emission in GaAs. They obtained numerical predictions of the temporal response times of NEA GaAs transmission photo-cathodes. Incident light of 650 nm wavelength was chosen. Table 2.1 contains the other input data used in their simulation work. Figure 2.13 shows the quantum yield as a function of incident photon energy. Figure 2.14 shows the transit time and transit time spread plotted for a 50nm thickness transmision photocathode.

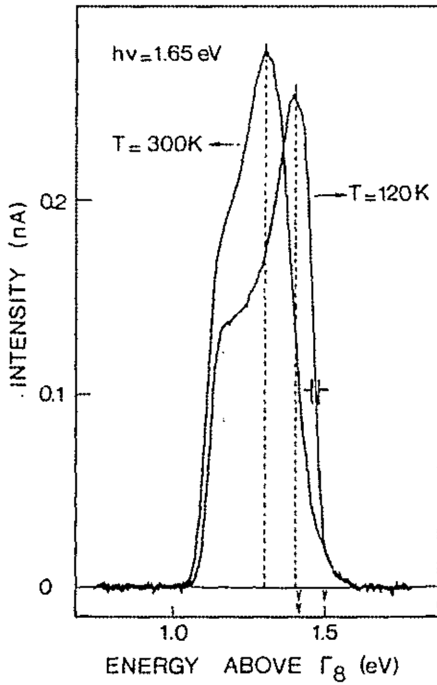

Fig. 2.10 EDC's at 300 and 120K for

$h\nu = 1.65\text{eV}$

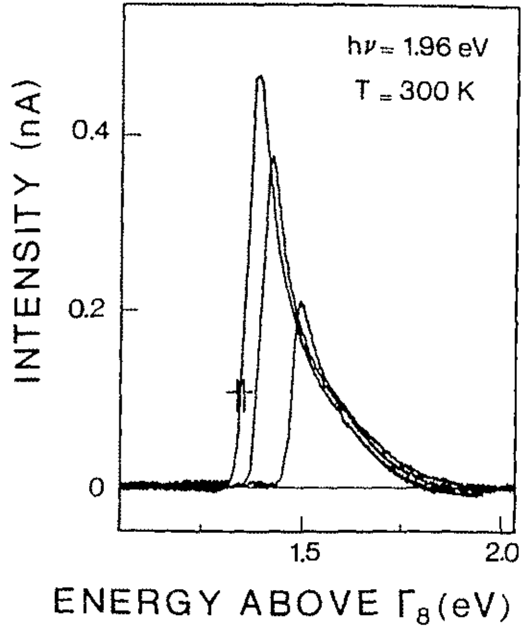

Fig. 2.11 EDC time evolution

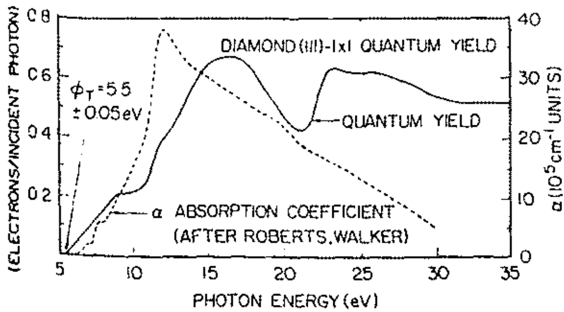

Fig. 2.12 Quantum photoyield from natural diamond (111) surface

Parameter	(000) valley		(100) valley
doping concentration (cm^{-3})		1×10^{19}	
surface recombination velocity (m/s)		2×10^{5}	
surface-escape probability	0.04		1.0
phonon speed (m/s)		7×10^{3}	
effective mass, m^*/m_0	0.067		0.35
intervalley separation (eV)		0.36	
electron mean free path (nm)	70		4.3
electron life-time (s)	1×10^{-9}		3×10^{-12}

Table 2.1 Input data used in simulation work

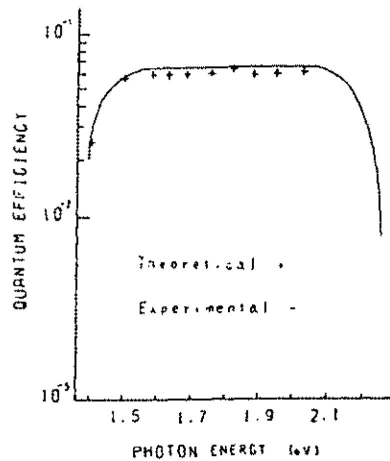

Fig. 2.13 Calculated and measured quantum efficiency curves for transmission GaAs photocathode

Photoelectron spectra of transmission mode GaAs photocathodes for various thicknesses, obtained from another simulation experiment [38] has been shown in figure 2.15. Other transit time distributions of emitted electrons for a couple of other photon energies were also reported by Yang *et al.* [39].

However, these calculations contained a number of assumptions, and hence cannot be considered very accurate. For instance, the kinetic energy of the photoexcited electrons was taken to equal the photon energy. This is clearly unphysical since it neglects the energy bandgap. Instead, the electron energy should be measured from the valley minima. The transmission probability for electron emission was taken to be constant for a valley instead of calculating it on the basis of electron energy. This simplification can result in serious errors for electrons residing in the satellite valleys due to the existence of a large transverse momentum component. Details of the calculations with regard to this point, have been presented in the Appendix. Furthermore, their Monte Carlo simulations did not consider the energy dependence of the electronic scattering processes. Instead, a constant scattering time independent of the carrier kinetic energy was assumed. We have attempted to address all of the above shortcomings in our Monte Carlo simulations in order to obtain more reliable predictions.

2.9 PROBLEM DEFINITION AND RESEARCH ISSUES

This thesis research focusses on the numerical simulation of photoemission from NEA based GaAs and diamond materials. Though the Cs-GaAs NEA system has been extensively studied and commercial NEA based devices have successfully been manufactured, details of ultrafast transient response in the sub-nanosecond regime remain

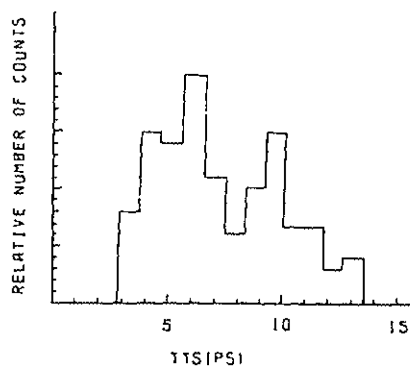

Fig. 2.14 Simulated TTS of emitted electrons for 50nm thickness transmission GaAs photocathode

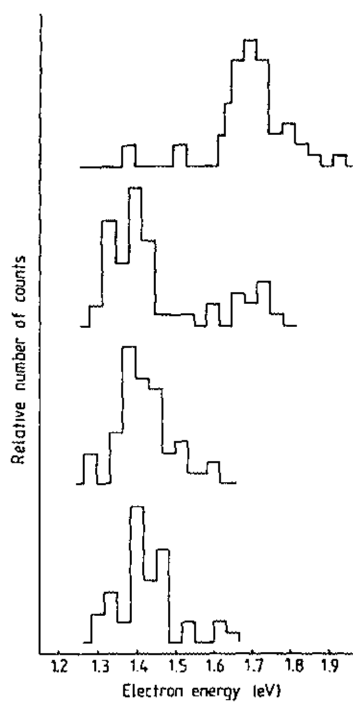

Fig. 2.15 Photoelectron spectra of transmission mode GaAs photocathode of thickness (from bottom to top) 2000, 150, 100 and 40 nm

unexplored. Experimental data pertaining to the electronic pulse shape and beam characteristics for picosecond pulsed laser excitation is not readily available. Given the recent development of picosecond lasers, an evaluation of such ultrafast response characteristics becomes a germane issue.

One of the fundamental questions considered in this research, is to ascertain the sharpness limits of electron beams that can be generated by using such ultrafast photoexcitation sources. Generation of narrow pulses of electrons is important for several applications, including the development of free-electron lasers (FEL). The spread in the energy distribution is also a critical aspect, since efficient FEL action requires a narrow bunching of electrons in energy space. Typically, one expects the dynamics of the internal carrier transport and the delay associated with multiple quantum mechanical reflections, to determine the width and sharpness of the emitted electron pulse. A secondary goal here is to obtain meaningful predictions of the electron beam characteristics such as the energy distribution and angular spread. The angular dispersion plays a role in determining the required degree of focussing and influences the overall system efficiency. The e-beam characteristics depend on a variety of parameters such as: the excitation wavelength, operating temperature, doping density, and sample thickness. Since these characteristics have not been studied to date for ultrafast photo-excitation, our aim is to obtain quantitative predictions through numerical modeling, and analyse the effect of these parameters.

Next, numerical studies of photoemission for the diamond NEA system are non-existent. An important research task in this thesis research, therefore, is to evaluate the potential of this material as a photoemitter. Details of carrier transport in diamond have also not been investigated in great detail. Hence, accurately modeling the process of electronic

flow towards the emitting surface, constitutes another important issue. The effect of an indirect conduction valley on the quantum mechanical transport at the surface will also be evaluated. This is necessary since diamond, unlike GaAs and the other III-V compounds, is a material with an indirect bandgap.

In order to understand and evaluate the transient response and photo-emission characteristics such as the energy distribution, temporal shape and angular profiles from GaAs and diamond photoemitters; numerical simulations based on the Monte Carlo approach have been developed. As an initial validity check of the Monte Carlo model developed in this research, simulations have been carried out for GaAs material to facilitate direct comparisons with available experimental data. Subsequently, simulations have been performed to evaluate the diamond NEA system. For simplicity, pure crystalline material has been assumed in this research, without any internal defects or graphitic clusters. Predictions of photo-emission yield a useful comparison of the performance capabilities between GaAs and diamond.

CHAPTER 3

NUMERICAL SIMULATION SCHEME

3.1 INTRODUCTION

The study of charge transport in semiconductors is of fundamental importance both from the point of view of basic physics and for its application to electronic devices. Charge transport is in general a tough problem, from both the mathematical and physical points of view. Calculations of transport properties in semiconductors have most commonly been approached by attempting to solve the Boltzmann Transport Equation (BTE). The BTE describes the dynamic evolution of the distribution function, f, under non-equilibrium conditions. The total rate of change of distribution function f can be expressed as:

$$\frac{\partial f}{\partial t} = -\mathbf{v} \cdot \frac{\partial f}{d\mathbf{r}} - \frac{e}{\hbar}\mathbf{F} \cdot \frac{\partial f}{\partial \mathbf{k}} + \left[\frac{\partial f}{\partial t}\right]_{coll} , \tag{3.1}$$

where **F** is the applied external field, **v** is the velocity, and $\left[\frac{\partial f}{\partial t}\right]_{coll}$ is the change in f due to collision and scattering. The first and second terms of the equation describe the effects of the density gradient and of the external electric field respectively on the distribution function. The collision term in the equation involves an integral. This yields a complicated integro-differential form for the BTE, which does not offer simple (or even complicated) analytical solutions except for very few cases, and these cases usually are not applicable to real systems. Furthermore, since transport quantities are derived from the averages over many physical processes whose relative importance is not known *a priori*, the formulation of reliable microscopic models for the physical system under investigation is difficult [40].

Approximate analytical solutions involve either approximations on the form of the scattering rates, or assumptions on the distribution function. The two most used techniques are the Legendre polynomial expansion [41] and the displaced Maxwellian approximation [42]. In most cases of interest the approximations are so drastic that it is no longer clear whether the features of interest in the results are due to the microscopic model or to mathematical approximations.

To circumvent the problems associated with analytical solution of the Boltzmann transport equation, numerical techniques have been developed to obtain an exact solution for the distribution function. With the aid of modern large and fast computers, exact numerical solutions of the BTE can be obtained for microscopic physical models of considerable complexity in a relatively short computer execution time. The two most important numerical techniques are the iterative method [43] and the Monte Carlo technique [44]. The Monte Carlo technique is by far the more popular of the two. This technique is easy to implement and offers the following advantages:

- The microscopic interpretation of the physical details is quite transparent.
- Stochastic calculation is achieved at a minimum level of difficulty while incorporating memory effects.
- Time and space dependent phenomena can be easily simulated.
- No arbitrary assumption regarding the distribution function needs to be made.

Monte Carlo is a statistical numerical method used for solving mathematical problems. It was born well before its application to the transport problems, and has been applied to a number of scientific fields. In the case of charge transport, however, Monte

Carlo approach to the solution of the Boltzmann equation proves to be a direct simulation of the dynamics of charge carriers inside the crystal, so that, while the solution of the equations is being built up, any physical information required can be easily extracted. This method was first applied to transport in semiconductors by Kurosawa [44] to study steady-state hole transport in Ge. Fawcett *et al.* [45] extended this method for use in GaAs where different scattering processes and band structures must be incorporated.

3.2 THE MONTE CARLO METHOD

The Monte Carlo method, as applied to charge transport in semiconductors, consists of simulation of the motion of one or more electrons inside the crystal, subject to the action of external forces due to applied electric and magnetic fields and of given scattering mechanisms. In the frame of semiclassical approximation, the motion consists of a sequence of free flights interrupted by instantaneous scattering events. The approach is semi-classical in the sense that the particles are treated as classical point-like objects, but the scattering rates are determined using quantum mechanical theory. During the free flight, electrons obey classical laws of motion and drift in the electric field. The free flight time, the type of scattering event, and the final state of the electron after the scattering are random quantities which are selected stochastically in accordance with some given probabilities. The probability distributions for these random quantities can be expressed in terms of the transition rates due to the various processes and the strength of the electric field. In practice, the physical distributions may be quite complex and difficult to manipulate even with a computer. The manipulation can be simplified by mapping the complex distributions on to a simple pseudo-random distribution [46]; the most convenient pseudo-random distribution

is the uniform distribution, which is readily available on most computer systems. In general, if p(q) and p(r) are the respective probability densities, associated with q in the physical distribution and r in the pseudo-random distribution, then:

$$\int_0^q p(q')\ dq' = \int_0^r p(r')\ dr' \quad . \tag{3.2}$$

In a uniform distribution p(r) = 1, so we get :

$$r = \int_0^q p(q')dq' \quad . \tag{3.3}$$

Hence, provided that this integral can be evaluated in a simple closed analytic form, inversion will yield a random value for the physical variable q in terms of the uniformly distributed random number r. As a consequence, any Monte Carlo method relies on the generation of a sequence of uniformly distributed random numbers corresponding to various random processes involved in the phenomenon of interest.

When the purpose of analysis is the investigation of a steady-state, homogeneous phenomenon, it is sufficient in general to simulate the motion of one single electron; from ergodicity we may assume that a sufficiently long path of this simple electron will give information on the behavior of the entire electron gas. When, on the contrary, the transport process is not homogeneous or stationary, it is necessary to simulate the motion of an ensemble of charge carriers and evaluate over the time the ensemble average of the physical quantities of interest. The method is known as Ensemble Monte Carlo (EMC) method. A flow chart of a simple EMC program is shown in figure 3.1. The structure of the program is summarized below, describing various steps involved in the procedure.

3.2.1 DEFINITION OF THE PHYSICAL SYSTEM

The starting point of the program is the definition of the physical system of interest, which includes the parameters of the material and the values of physical quantities, such as lattice temperature and electric field. The parameters that control the simulation are also defined, such as the number of electrons simulated, duration of each subhistory, total time of simulation, the desired precision of results, and so on. The next step in the program is a preliminary calculation of the scattering rates as a function of electron energy. The scattering rates are normalized and stored in a tabulated form.

3.2.2 INITIAL CONDITIONS

This step involves choosing the initial position, momentum, and energy of the electrons. Uniformly distributed random numbers are used to select the initial position and direction of motion of the electrons, if required. The valley of the electrons in the conduction band is also chosen. Usually, the electrons all reside in the lowest valley and are assumed to be in a state of initial thermal equilibrium. For simulations involving photoexcitation, the initial state lies in the lowest direct valley with an energy equal to the excess energy of the external excitation. The momentum at this initial energy is usually distributed randomly. This is reasonable for unpolarized light. However, in situations involving polarized radiation or in case of electrical carrier injection from a contact, the distributions would be suitably modified.

For example, electronic energies associated with injection from a contact would correspond to a heated Maxwellian with a semi-hemispherical distribution for the momenta.

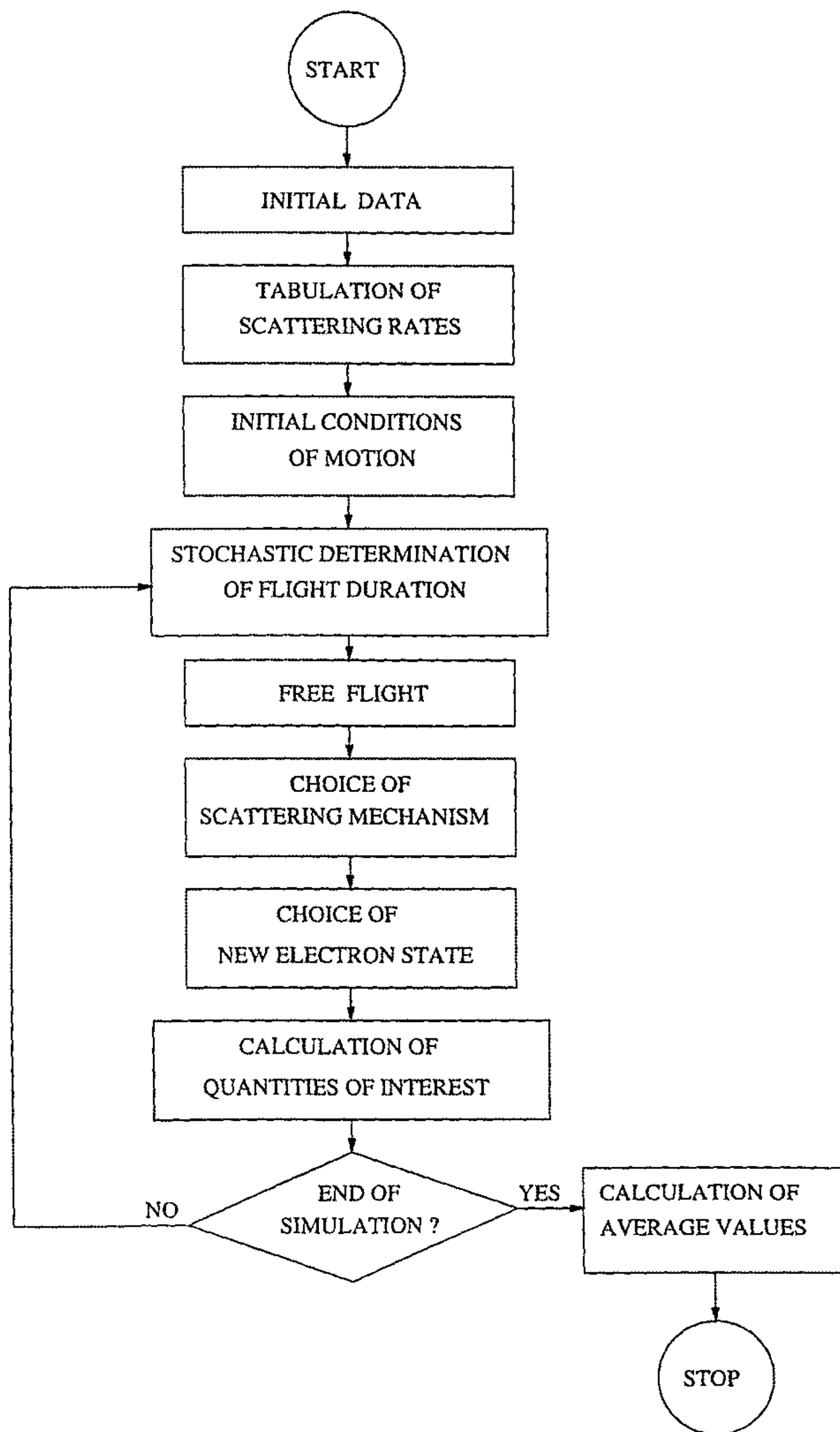

Fig. 3.1 Flow chart of a simple Ensemble Monte Carlo program

3.2.3 FLIGHT DURATION

The next step is to determine the free flight time for each electron. The flight time depends on the scattering probability. Each process that can scatter the electron at the end of a free flight is characterized by a transition rate $S_n(\mathbf{k}, \mathbf{k}')$, from the momentum state $\hbar\mathbf{k}$ to $\hbar\mathbf{k}'$. Here the subscript n denotes an individual scattering process and can take values n = 1,2,...,N if there are N possible processes. The total scattering rate from the state **k**, because of the nth process, is given by:

$$\lambda_n(\mathbf{k}) = \int S_n(\mathbf{k},\mathbf{k}')\, dk' \quad . \tag{3.4}$$

Hence, the total scattering rate, due to all processes, is

$$\lambda(\mathbf{k}) = \sum_{n=1}^{N} \lambda_n(\mathbf{k}) \quad , \tag{3.5}$$

where **k** is a function of time. In practice the total scattering rates are only functions of $|\mathbf{k}|$, so $\lambda(\mathbf{k})$ can be easily transformed to $\lambda(E)$. Thus, if $\lambda(\mathbf{k})dt$ is the probability that an electron in the state **k** suffers a collision during the interval dt, the probability that an electron which suffered a collision at time t=0 has not yet suffered another collision after a time "t" is:

$$\exp\left(-\int_0^t \lambda[\mathbf{k}(t')]\, dt' \right) \quad . \tag{3.6}$$

Consequently, the probability the electron will suffer its next collision during interval dt around t is given by :

$$P(t)\, dt = \lambda[\mathbf{k}(t)] \exp\left(-\int_0^t \lambda[\mathbf{k}(t')] dt' \right) dt \, . \tag{3.7}$$

The probability density P(t) is, therefore:

$$P(t) = \lambda[\mathbf{k}(t)]\ \exp\left(-\int_0^t \lambda[\mathbf{k}(t')]dt'\right)\ . \tag{3.8}$$

Using eq.(3.8) and eq.(3.3), a uniformly distributed random number r can be used to describe the process, which gives:

$$r = 1 - \exp\left(-\int_0^t \lambda[\mathbf{k}(t')]dt'\right)\ . \tag{3.9}$$

Eq.(3.9) is very complicated and cannot, for practical scattering mechanisms, be solved analytically for t. Numerical integration can be performed to produce r and t in tabular form for each value of electron energy, but this approach is time consuming and rather impractical.

A new technique for circumventing this difficulty has been found [47,48]. It involves supplementing the real scattering processes with a virtual scattering process that does not affect the state of the electron. This scattering mechanism is usually referred to as "self scattering" or "null collision". The virtual scattering rate $\lambda_V(\mathbf{k})$ is chosen such that total scattering rate becomes a constant. Thus, total scattering rate for the electron which includes the virtual process is simply:

$$\lambda_T(\mathbf{k}) = \lambda(\mathbf{k}) + \lambda_V(\mathbf{k}) = \Gamma\ . \tag{3.10}$$

Eq.(3.8) now reduces to the elementary form

$$r = 1 - e^{-\Gamma t}\ . \tag{3.11}$$

Solving for t gives:

$$t = -\frac{1}{\Gamma}\ln(1-r) = -\frac{1}{\Gamma}\ln(r) \quad . \tag{3.12}$$

Flight time "t", can thus be determined form the uniformly distributed random number r. Γ is chosen to be the maximum value of $\lambda(\mathbf{k})$ in the region of k space of interest. This is done to avoid negative values for $\lambda_v(\mathbf{k})$. If an electron undergoes a self scattering, its state **k** after the collision is taken to be equal to its state **k** before the collision, so that in practice the electron path continues unperturbed as if no scattering at all had occurred. The computer time wasted in taking care of self scattering events is more than compensated for by the simplification of the calculation of the free flight time.

3.2.4 FREE FLIGHT

The electrons are allowed to drift freely under the influence of the electric field. During the free flight, the electron wave vector **k** changes continuously according to Newton's law of motion for the frictionless regime in the absence of magnetic fields or any thermal gradients:

$$\hbar\frac{\partial \mathbf{k}}{\partial t} = e\mathbf{E} \quad . \tag{3.13}$$

The flight is terminated after the free flight time with a scattering event. The parameters of interest like position, momentum and energy of the electron are recorded at the end of the free flight.

3.2.5 CHOICE OF THE SCATTERING MECHANISM

The scattering rates of the various mechanisms are tabulated as function of energy and normalized to Γ. Thus for a given E, the normalized probability $P_j(E)$ for the scattering mechanism j is $\lambda_j(E)/\Gamma$. The selection of scattering mechanism is made by generating a random number r between 0 and 1. If $\sum_{i=1}^{i=j-1} P_i(E) < r < \sum_{i=1}^{i=j} P_i(E)$, then the jth scattering mechanism is selected. If $r > \sum_{i=1}^{N} P_i(E)$, where N is the total number of scattering mechanisms, then self scattering occurs. The procedure is shown in the flow chart of figure 3.2. The inequality

$$r < \sum_{i=1}^{i=m} P_i(E) \quad , \tag{3.14}$$

is tested for all possible values of m, starting from 1 and going up to N, and scattering process m is selected once the inequality is satisfied.

3.2.6 CHOICE OF STATE AFTER SCATTERING

Once the scattering mechanism that caused the end of the flight has been determined, the new state after the scattering of the electron, $\mathbf{k}'$ must be chosen. If a self scattering has occurred, $\mathbf{k}'$ is taken equal to $\mathbf{k}$, the flight is not terminated and a new flight time Δt is chosen and added to t. This goes on until a real scattering event is selected. When a real scattering event occurs, $\mathbf{k}'$ is chosen stochastically according to the differential cross-section of that particular mechanism. Energy of the electron is altered if an inelastic process such as polar optical, or intervalley scattering has occurred. On the other hand, for ionized impurity scattering or acoustic scattering, the final energy equals the initial energy because of the elastic nature of the collision. A change in momentum will always occur, however, the

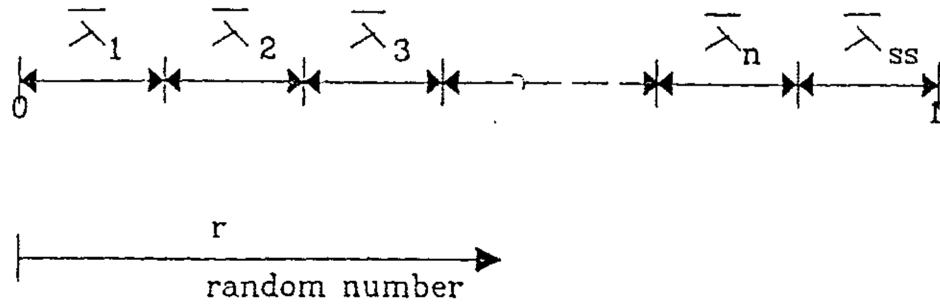

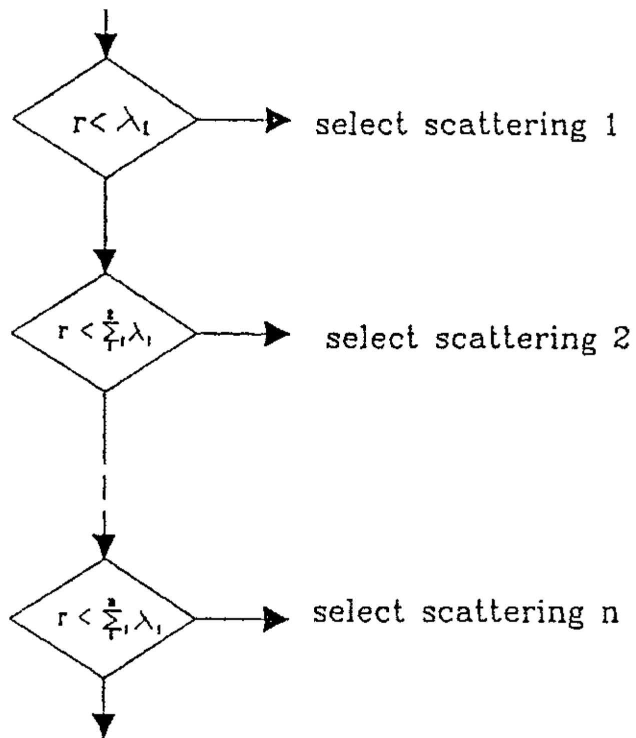

Fig. 3.2 Flow chart of scattering mechanism selection in Monte Carlo simulations

scattering mechanism could be either a momentum randomizing (acoustic, intervalley scattering) or non-momentum randomizing (polar optical, ionized impurity scattering) process. Optical phonons add or extract a constant quanta of energy "hω" through emission or absorption. Such a fixed energy quanta is a direct consequence of the ω-k dispersion curves for optical phonons in semiconductor materials. The determination of the new wave vector **k** after the phonon scattering requires further generation of random numbers. These random numbers are used to determine the azimuthal angle θ and angle ϕ according to the angular dependence of the selected scattering mechanism. The angle ϕ after the scattering can take any value between 0 to 2π with equal probability. So ϕ is chosen using a random number r as:

$$\phi = 2\pi r \quad . \tag{3.15}$$

On the other hand, the angle theta depends on the nature of the scattering process. For momentum randomizing processes, θ is given by:

$$r = \frac{1}{2}(1-\cos\theta) \quad . \tag{3.16}$$

For other scattering mechanisms, that have directional dependence P(θ), one can select θ by generating a random number and mapping the distribution P(θ) to a uniform distribution [47]. An illustrative diagram of these angles is shown in figure 3.3.

After the scattering event, the momentum and energy of the electron are updated. The position of the electron remains unchanged as the collisions are considered to be instantaneous. The electron begins its next flight and drift-scatter mechanism repeats until the end of the simulation.

Fig. 3.3 Geometry for determining the wave vector **k** after scattering in 3 - dimensional simulation

3.2.7 COLLECTION OF RESULTS

The data collected at each free flight forms the base for the determination of the quantity of interest. Synchronous ensemble method is used to determine the average values of desired quantities. The average value of a quantity A is defined as the ensemble average at time t over the N electrons of the system

$$<A(t)> = \frac{1}{N} \sum_{i=1}^{N} A_i(t_i=t) \quad . \tag{3.17}$$

N is chosen large enough so that the simulated electrons represent the behavior of the entire electron gas.

3.3 IMPLEMENTATION OF THE MONTE CARLO TECHNIQUE

The study of photo-emission from GaAs and diamond has been done using the Monte Carlo technique. This section discusses the implementation of the technique for the given case. Figure 3.4 shows the flow chart of the program used.

The first step in the program is initialization of various physical quantities involved. Table 3.1 and 3.2 show various parameter values used for GaAs and diamond. The parameters controlling the simulation are also initialized. The number of electrons is taken large enough (10000) so as to represent the entire electron gas. This number is based on tradeoff between the computer time taken for simulation and accuracy of the results. Total time of simulation is chosen long enough to give sufficient time for the process of photo-emission to get completed. This time is chosen depending on the energy and width of the optical pulse. The duration of single time step of simulation is chosen based on the average value of the free flight time. The next step is calculation of scattering rates as a function of

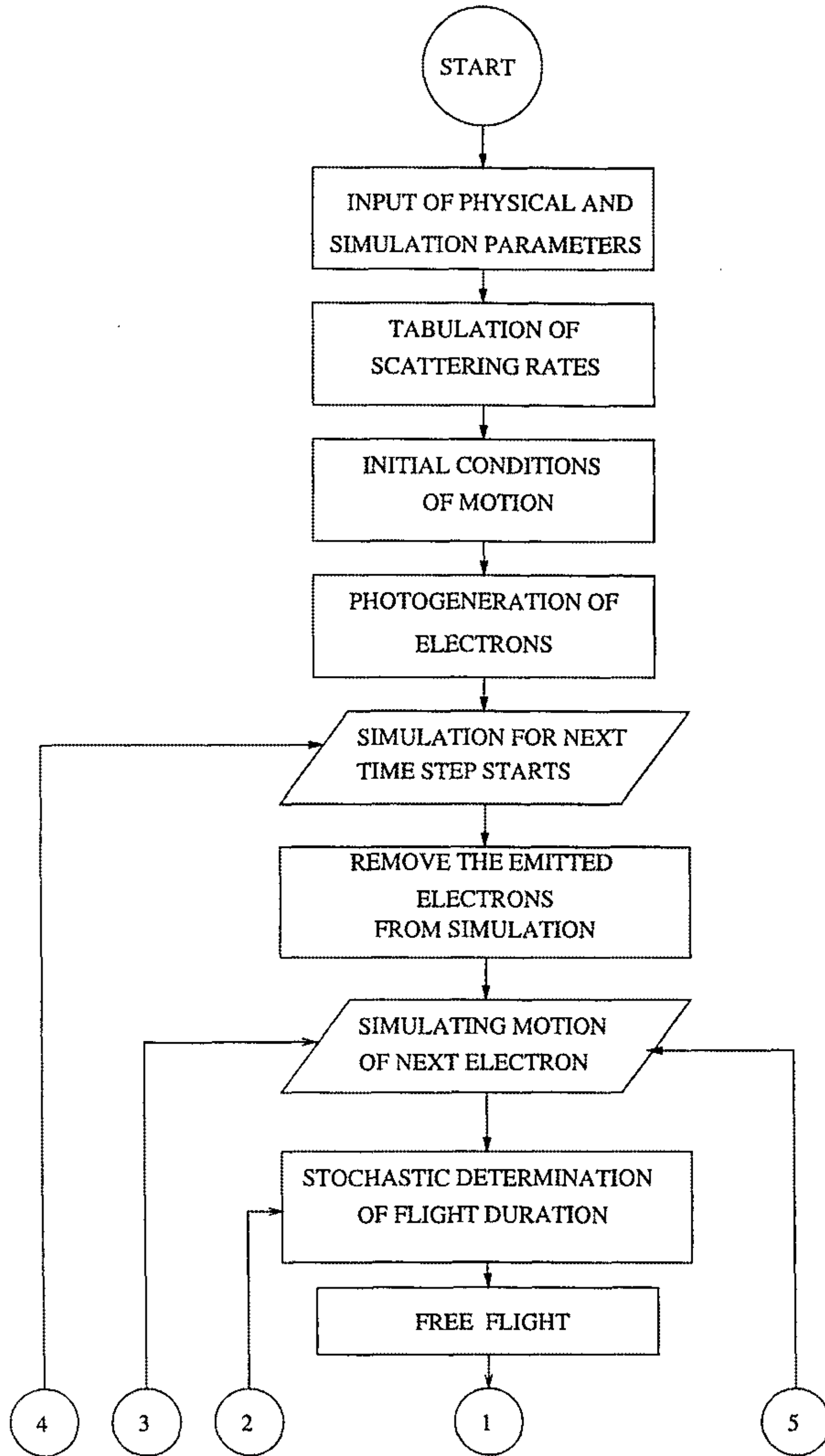
START
INPUT OF PHYSICAL AND SIMULATION PARAMETERS
TABULATION OF SCATTERING RATES
INITIAL CONDITIONS OF MOTION
PHOTOGENERATION OF ELECTRONS
SIMULATION FOR NEXT TIME STEP STARTS
REMOVE THE EMITTED ELECTRONS FROM SIMULATION
SIMULATING MOTION OF NEXT ELECTRON
STOCHASTIC DETERMINATION OF FLIGHT DURATION
FREE FLIGHT
4
3
2
1
5

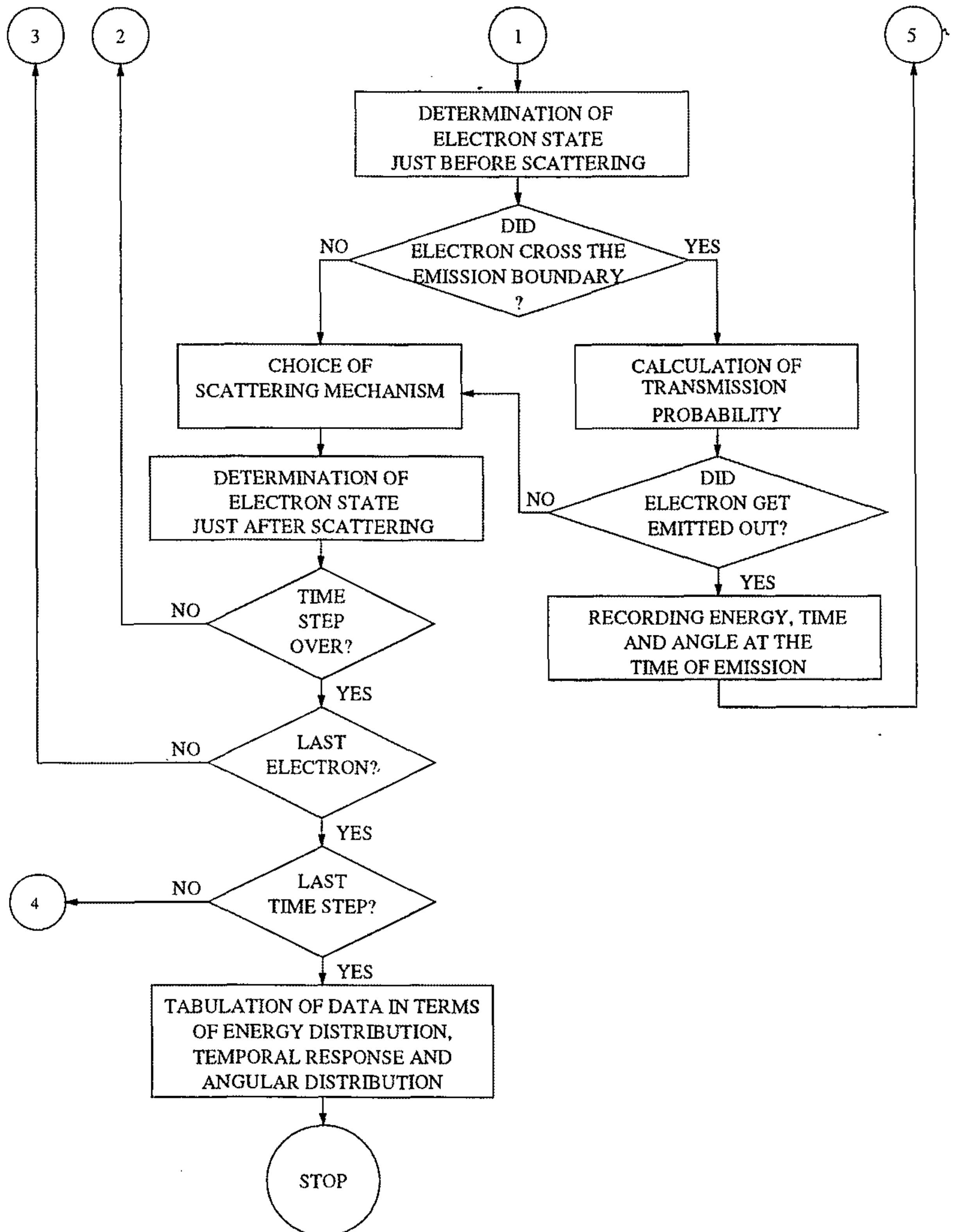

Fig. 3.4 Flow chart of the implementation of MC program for study of photoemission

Table 3.1 Parameter values used for GaAs in simulation

Parameter	Value
Lattice constant (a)	5.63Å
Density (ρ)	5.37 g/cc
Work-Function (W)	1.0 eV
V band bending (Vbb)	0.45eV
E-bar	0.25eV
High frequency dielectric constant	10.92
Static dielectric constant	12.9
Temperature	300K
Length of sample in x and y directions	1μm

Table 3.2 Parameter values used for diamond in simulation

Lattice constant (a)	3.5668Å
Density (ρ)	3.51g/cc
Bandgap	5.5eV
V band bending	0.45eV
Transverse effective mass of electron	0.36
Longitudinal effective mass of electron	1.42

electron energy. The rates due to various scattering mechanisms are normalized with respect to the maximum rate and stored in arrays. Different scattering mechanisms involved in GaAs and diamond are discussed later in this chapter.

The next step involves the choice for the initial distribution of the electrons. The x and y coordinates of the electrons are chosen randomly, since there is no particular preference for the position of the electrons in the x and y directions. The z coordinate of the electrons depends on the absorption of optical pulse along the z-direction in the sample (we assume that the pulse is incident along the z-direction and photo-emission takes place from the surface perpendicular to the z-direction). The distribution of electrons in z-direction also depends on whether the emission occurs in the transmission or reflective mode. In either case, the electron positions are distributed in accordance with the Beer-Lampert law which leads to a decaying exponential. However, the maximum initial density occurs at the front emitting surface for the reflective mode. For the transmission mode, the highest density is at the back surface and with the lowest value at the front emiting surface. The initial energy of the electrons is chosen based on the photon energy and the bandgap. Initially all the photo-excited electrons are placed in the Γ valley. The momenta of the electrons are calculated from their energies. The initial direction of motion of the electrons is chosen randomly. Now the number of electrons excited into the conduction band in each time step is calculated. The conduction band is assumed to be empty before photo-excitation. The fraction of excited electrons in each time step depends on the duration of the time step and total pulse width.

The simulation of the first time step begins now. We start with the first electron. The free flight time for the electron is determined. The electron starts with its initial position, energy and momentum and drifts in the electric field for the duration of free flight time.

Electric field is present due to the band bending near the surface. The free flight ends with a scattering event. The position, energy, and momentum of the electron are recorded at the end of the free flight. If the electron goes out of bound in the x or y direction, is reinjected from the opposite direction, so that the simulation remains unaffected. In z-direction, if the electron goes out of the emitting surface, the probability of the electron getting emitted out is calculated. Based on the transmission probability and a random number selected, the electron is either emitted out or reflected back from the surface. In case the electron gets emitted out, its energy, direction and time of emission are recorded, and the electron is removed from simulation. Otherwise a scattering mechanism is selected stochastically based on the energy of the electron. The state of the electron after the scattering is determined based on the scattering mechanism chosen. The electron starts next free flight with its new position, energy, and momentum. The above mentioned procedure is repeated. The sequence of free flights interrupted by scattering events continues until either the electron gets emitted out, or the end of the time step is reached.

The simulation procedure is repeated for each electron in the conduction band. At the end of first time step, the electrons for the second time step are generated and added to the simulation. Simulation is carried out for the second time step in the same way. The procedure continues till the end of the simulation time, adding electrons generated by photo-excitation, and removing those which got emitted out. Energy, time of emission, and angle made with z-axis at the time of emission are recorded for each emitted electron. At the end of the simulation, the photo-emission data is arranged in a more interpretable form, showing the number of emitted electrons for different ranges of energy, time and angle.

3.4 QUANTUM MECHANICAL REFLECTION AT SURFACES

When an electron inside the sample reaches the photoemission surface, there is a finite probability of it getting reflected back from the boundary into the sample. This occurs because of quantum mechanical reflection of electron from the sample-Cs-vacuum boundary. A quantum mechanical treatment of the problem, involving electron wave functions across the boundary region based on the effective mass approximation, has been done in Appendix A. The transverse component of the electron momentum is conserved across the boundary. Based on these calculations, a transmission probability for the electron is determined based on its energy, parallel momentum, and occupied valley, whenever it crosses the photoemission surface. Then, depending on a random number selected and value of the transmission probability, the electron is either emitted out or reflected back from the surface. This is an important step in simulation since practical NEA emitters have Cs coating on the surface and exclusion of this step will lead to an unrealistically large number of electrons getting emitted.

Quantum mechanical reflections are similarly very important for diamond because of its bandstructure. Diamond is an indirect bandgap material and has six equivalent valleys along [100]. The conduction band minima in diamond are located at about 76 % of the X-point within the Brillouin zone. Consequently, the wavevectors of an oncoming electron near the surface would approximately be either: $[\pm\pi/a,0,0]$, or $[0, \pm\pi/a,0]$, or $[0, 0, \pm\pi/a]$ depending on its resident valley. As a result, values of the transverse momentum associated with electrons at the surface would have a wide range. Now given in Appendix A, the quantum mechanical transmission probability strongly depends on the value of the transverse momentum of an incoming electron. The essence of the detailed calculations of AppendixA,

is that the probability sharply decreases with the transverse electronic momentum. As a result, the overall probability of electronic emission will have a wide range corresponding to the variations in transverse momenta. It is therefore critical to include the quantum mechanical transmission calculations for an accurate quantitative analysis.

3.5 SCATTERING MECHANISMS IN GaAs AND DIAMOND

Calculation of scattering rates is an important step in the Monte Carlo method. It requires knowledge of quantum mechanics behind each scattering mechanism involved. The aim is to determine the various scattering probabilities as a function of electron energy. This section contains a brief discussion of the scattering mechanisms and the underlying quantum mechanics. A detailed treatment of the issue can be found elsewhere [40].

3.5.1 GENERAL THEORY

The transitions of interest for electron transport in semiconductors can be classified as intervalley, if both initial and final states of the electron lie in the same valley, or intervalley, if the final state lies in a valley different from that of the initial valley. The transitions are induced by different scattering sources present in the crystal of which the most important are phonons, impurities and other electrons.

In the Born approximation, the scattering process only consists of a transition between two definite momentum states for the electron involved. One has to make the assumption that the system can be separated into the electron of interest and rest of the crystal, the so called quasi-particle approximation. The vector state for such a combined system can be written as the direct product [40]:

$$|\mathbf{k}, c\rangle = |\mathbf{k}\rangle |c\rangle \tag{3.18}$$

where $|\mathbf{k}\rangle$ and $|c\rangle$ represent the unperturbed states of the electron and the crystal, respectively. The transition probability per unit time for scattering from a state $\mathbf{k}$ to $\mathbf{k}'$, due to a perturbation Hamiltonian H, is given by the Fermi Golden rule

$$S(\mathbf{k},\mathbf{k}') = \frac{2\pi}{\hbar} |<\mathbf{k}|H'|\mathbf{k}'>|^2 \delta(E'-E) \quad , \tag{3.19}$$

where $|<\mathbf{k}|H'|\mathbf{k}'>|^2$ is the matrix element of H' between the initial and final states and the delta-function expresses the conservation of energy, E and E' being the eigenenergies of the initial and final states, respectively. For a transition due to a phonon with wavevector $\mathbf{q}$ and frequency ω, we have:

$$E' - E = \pm\hbar\omega , \tag{3.20a}$$

$$\mathbf{k} - \mathbf{k}' \pm \mathbf{q} = \mathbf{G} , \tag{3.20b}$$

where $\mathbf{G}$ is a reciprocal lattice vector. When $\mathbf{G}$=0, we have an Umklapp process. By integrating over all possible final states $\mathbf{k}'$, the total scattering rate out of state $\mathbf{k}$ is obtained.

$$\Gamma(\mathbf{k}) = \frac{2V}{8\pi^3}\int dk'\int d\phi\int d\theta\, S(\mathbf{k},\mathbf{k}')\, k'^2 \sin\theta \quad , \tag{3.21}$$

where V is the volume of the crystal, θ is the angle between $\mathbf{k}$ and $\mathbf{k}'$, and ϕ is the azimuthal angle. The factor of "2" comes from the spin-degeneracy of the electronic states. The angular dependence of the scattering is obtained directly from the angular dependence of $S(\mathbf{k}, \mathbf{k}')$. For non-Umklapp process, the matrix element in eq.(3.19) can be factorized as

$$|\langle \mathbf{k}|H'|\mathbf{k}'\rangle|^2 = V(\mathbf{q})\, G(\mathbf{k}, \mathbf{k}') \ , \tag{3.22}$$

so that the transition rate is :

$$S(\mathbf{k},\mathbf{k}') = \frac{2\pi}{\hbar} V(\mathbf{q})\, G(\mathbf{k},\mathbf{k}')\, \delta(E'-E) \ , \tag{3.23}$$

where $V(\mathbf{q})$ contains the dependence upon $\mathbf{q} = \mathbf{k}' - \mathbf{k}$ of the square Fourier transform of the interaction potential. The manner in which $V(\mathbf{q})$ depends on the momentum transfer depends on the nature of scattering. Here $G(\mathbf{k}, \mathbf{k}')$ is the overlap factor integral

$$G(\mathbf{k},\mathbf{k}') = \left|\int_{cell} U^*_{\mathbf{k}'}(\mathbf{r})\, U_{\mathbf{k}}(\mathbf{r})\, d\mathbf{r}\right|^2 \ , \tag{3.24}$$

between the periodic part of the Bloch wave functions of the initial and final states. The overlap factor is exactly equal to one for parabolic bands. However, when the non-parabolicity of the bands is taken into account, the overlap integral is always less than one and is usually expressed as a function of the non-parabolicity coefficients.

Now we consider the different scattering mechanisms individually. The electron-phonon interaction is due to the deformation associated with phonon vibrations, of the otherwise perfect crystal. In covalent semiconductors it is described in the framework of the deformation-potential method [49] for both acoustic and optical phonons. As regards impurities, they can be ionized or neutral. In the former case the interaction is of long-range Coulomb type, while in the latter, the interaction is of much shorter range. The overall effect of neutral impurities is, in general, much weaker. Hence the neutral impurities are not included in the Monte Carlo calculations. The electron-electron collisions are also not

considered for the simulation process since their effect is also very limited at the low carier densities being considered here.

3.5.2 ACOUSTIC PHONON SCATTERING

The energy change in acoustic phonon scattering is negligible and it is treated as an elastic process. However, for nonlinear transport problems in low fields or temperature, the small energy dissipation is needed to establish a smooth distribution function. The squared matrix element V(q) (eq. 3.22) is given by:

$$V(q) = \frac{E_a^2 \hbar q}{2\rho s}\left(N_q + \frac{1}{2} \pm \frac{1}{2}\right) , \tag{3.25}$$

with the plus (minus) sign in ± referring to phonon emission (absorption) process. E_a is the acoustic deformation potential, ρ the crystal density, s the speed of sound, and N_q the Bose-Einstein distribution given by:

$$N_q = \left(\exp\left[\frac{\hbar\omega}{kT}\right] - 1\right)^{-1} , \tag{3.26}$$

where $\hbar\omega$ is the phonon energy. The acoustic phonon scattering rate can be determined by substituting V(q) in eq.(3.23) and using eq.(3.21) for integrating over all $\mathbf{k}'$.

3.5.3 POLAR OPTICAL SCATTERING

In optical phonon mode of vibration the two oppositely charged unit cells oscillate out of phase. The displacement during the oscillation sets up a polarization field that scatters the electron. The square of matrix element for this process is given by:

$$V(q) = \frac{4\pi e^2}{4\pi\epsilon q^2}\frac{\hbar\omega}{2}\left(\frac{1}{\epsilon_\infty}-\frac{1}{\epsilon_0}\right)\left(N_q+\frac{1}{2}\pm\frac{1}{2}\right) , \tag{3.27}$$

where ϵ_∞ and ϵ_0 are the high frequency and static dielectric constants respectively. N_q is again given by the Bose-Einstein distribution.

3.5.4 NON-POLAR OPTICAL PHONON SCATTERING

The non-polar optical phonons generate a short range potential that causes a shift in the electronic band states. In the long wavelength optical mode of vibration, one set of atoms moves as a body against the second set of atoms which creates a strain in the lattice. The scattering of electrons by this strain is known as deformation potential scattering. The square of matrix element is given by:

$$V(q) = \frac{D_0^2\hbar^2}{2\rho\hbar\omega}\left(N_q+\frac{1}{2}\pm\frac{1}{2}\right) , \tag{3.28}$$

where D_0 is the deformation optical potential.

3.5.5 INTERVALLEY PHONON SCATTERING

The transitions between different valleys involve a large amount of momentum transfer so that the polar interactions play a negligible role. The wave-vector **q** of the phonons causing the transitions is nearly the same as the distance between the minima of the initial and final valley in the Brillouin zone. This fixes **q** for a given pair of valleys, so that the energy change in these transitions is constant for a given phonon mode. Consequently the

intervalley transitions can also be treated using the deformation potential concept. The squared matrix element is given by:

$$V(q) = \frac{D_{ij}^2 \hbar^2}{2\rho\hbar\omega_{ij}} \left(N_q + \frac{1}{2} \pm \frac{1}{2} \right) \quad , \tag{3.29}$$

where D_{ij} is the deformation potential for scattering from the ith valley to the jth valley induced by a phonon of energy $\hbar\omega_{ij}$.

3.5.6 IONIZED IMPURITY SCATTERING

The ionized impurity scattering is elastic in nature and cannot control the transport by itself in the presence of an external field. It must be accompanied by some dissipative scattering mechanism to obtain the proper energy distribution. The scattering source for an ionized impurity is a screened Coulombic potential. A purely Coulombic potential distorts a plane electron wave at all distances, and consequently the scattering cross section is effectively infinite. Several models have been used to overcome this problem [50], and the two most important ones are the Conwell-Weisskopf model [51] and the Brooks-Herring formulation [52]. The squared matrix element in the Brooks-Herring case is given by:

$$V(q) = \frac{NZ^2 e^4}{(4\pi\epsilon)^2 (q^2+\beta^2)^2} \quad , \tag{3.30}$$

where Z is the number of unit charge in the impurity, and β is a constant screening parameter.

Electron transport in polycrystalline diamond involves one more type of scattering mechanism, which is discussed in detail in the next section.

3.6 GRAIN BOUNDARY SCATTERING IN POLYCRYSTALLINE DIAMOND

The practical utility of diamond has been enhanced by recent improvements in the growth of synthetic diamond films through chemical vapor deposition (CVD). However, the CVD films grown have been polycrystalline in nature and exhibit a granular structure. The measured electrical properties of the CVD films have generally been inferior to those of natural diamond [53], and have shown strong finite size effects. For example, free carrier mobilities were found to be lower in thin film diamond, and strongly dependent on the grain size and film thickness [27]. These findings suggest that electronic transport in polycrystalline diamond is strongly influenced by scattering mechanisms other than those normally encountered in bulk material. Most important of these is the scattering associated with the grain boundaries, which can strongly affect the charge transport in thin diamond films. The grain boundaries (and defects), in general, give rise to a distribution of scatterers within the material, and can produce internal band bending [54]. The band bending contributes to reductions in the free carrier mobility and imparts a strong temperature dependence.

In our calculations of field field transport in polycrystalline diamond films, the grain boundaries are treated as a series of parallel planes oriented perpendicular to the direction of the applied field. The diamond films are assumed to have thicknesses exceeding 1.0 μm in keeping with experimental data [55-57]. At these thicknesses, quantization effects on the phonon and carrier subsystems are negligible. The average separation between adjacent grain boundaries is taken to be "d" coinciding with the x-direction. The actual position "x_n" of the nth grain boundary is assumed to fluctuate in accordance to a normalized Gaussian distribution $f(x_1, x_2, \ldots x_N)$ given as:

$$f(x_1, x_2, \ldots x_N) = \frac{\exp[-\sum_{i=1}^{N-1} \frac{(x_{i+1}-x_i-d)^2}{2\sigma^2}]}{L_x [(2\pi\sigma^2)^{(N-1)/2}]} , \tag{3.31}$$

with "σ" being the standard deviation associated with the Gaussian distribution, "L_x" the longitudinal length of the film, and "N" (= L_x/d) the total number of grain boundaries encountered. We model the grain boundaries as delta-shaped scattering potentials of strength "S" located at positions x_n to yield a perturbing Hamiltonian V(x) given by:

$$V(x) = S \sum_{n=1}^{n=N} \delta(x-x_n) . \tag{3.32}$$

Physically, the strength "S" corresponds to a product of the energy perturbation and its spatial dimension. The value of "S" therefore depends on the magnitude of the band-bending and the spatial extent of the depletion (or accumulation) regions associated with a grain boundary. For plane wave unperturbed free electron states, the square of the matrix element $|\langle k'|V|k\rangle|^2$ can be evaluated, and yields the following expression in the Born approximation:

$$|\langle k'|V|k\rangle|^2 = (\frac{S}{L_x})^2 \delta(k_y-k_y)\delta(k_z-k_y) \sum_{n,n'} \exp[-j(k_x-k_x)(x_n-x_{n'})] . \tag{3.33}$$

The average scattering rate <S(k)> can then be calculated by applying the Fermi Golden rule and averaging the matrix element over the Gaussian distribution. This yields:

$$\langle S(k)\rangle = \frac{2\pi}{\hbar} \frac{2\,A\,L_x}{(2\pi)^3} \int d^3k' \, \delta(E'-E) \iint\ldots\int f(x_1, \ldots x_N) \, |\langle k'|V|k\rangle|^2 \, dx_1 \ldots d \tag{3.34}$$

Carrying out the integrations over the final momentum states then leads to:

$$<S(k)> = \frac{S^2\, m_x}{2\pi^2\hbar^3\, |k_x|\, L_x}\Big[\sum_{n,n'=1}^{N} \int\cdot\int f(x_1, ..x_N)\exp[2jk_x(x_n - x_{n'})]dx_1 ..dx_N\Big], \tag{3.35}$$

with m_x being the effective mass in the direction of the applied field. The spatial integrations can easily be performed. The double summation then yields the following result :

$$<S(k)> = \frac{S^2\, m_x}{2\pi^2\hbar^3\, |k_x|\, d}\Big[1 + 2\sum_{p=1}^{N-1} \{(1 - \frac{p}{N})\, \exp[-2pk_x^2\sigma^2]\, \cos(2pk_x d)\}\Big]. \tag{3.36}$$

In the limit of large "N", the above summation can be evaluated exactly [58] and yields:

$$<S(k)> = \frac{S^2\, m_x}{2\pi^2\hbar^3\, |k_x|\, d}\Big[\frac{1 - \exp(-4k_x^2\sigma^2)}{1 + \exp(-4k_x^2\sigma^2) - 2\exp(-2k_x^2\sigma^2)\cos(2k_x d)}\Big]. \tag{3.37}$$

The scattering rate of equation (7) depends on the average grain size "d", the standard deviation characterizing the actual grain boundary distribution, and the wavevector component parallel to the applied field. In the σ --> 0 limit, the scattering rate tends to zero. This is expected since the grain boundaries then become a perfectly periodic array of evenly spaced planes and can offer no resistance. Furthermore, the scattering is seen to be enhanced with increased non-uniformity of the grain boundary distribution, and also due to decreases in the grain size. This should lead to reductions in the mobility and drift velocity in samples having smaller inhomogeneous grains, a trend that has actually been observed in diamond and other materials [54,59]. Finally, equation (7) also predicts that carriers with low energy and momentum should be scattered more strongly than those having a large momentum parallel to the applied field. Classically, this implies that the effective reflection coefficient

at the grain boundaries is wavevector dependent, and that the motion of the fast, high energy carriers is least affected by the grains. As a result, the drift velocity and carrier mobilities are expected to increase with increasing temperature, which is consistent with the low temperature experimental trend of Pan et al. [59]. Finally, the smallest reductions in the drift velocity are expected for field orientations along the direction of the lowest effective mass. However in a many-valley semiconductor such as diamond, the anisotropy effect should average out and have an insignificant impact.

3.7 ORIENTATION DEPENDENCE

The transport of electrons within the sample depends on the orientation of the photoexcitation surface. This effect is especially pronounced in diamond due to directional dependence of the electronic mass. Figure 3.5(a) and (b) show the constant energy surfaces in the first Brillouin zone for GaAs and diamond. For diamond these are six ellipsoids along the <100> axes, with centers of the ellipsoids located at about three-fourths of the distance from the Brillouin zone center. For GaAs the constant energy surface is a sphere at the zone center. This gives one value of effective mass for GaAs at each valley, and two values for diamond - m_l^* along the symmetry axis (longitudinal mass), and m_t^* perpendicular to the symmetry axis (transverse mass). Figure 3.6 shows three different shapes of the constant energy surfaces and their respective E-k relationships. In case of diamond, drift of the electrons inside the sample depends on the component of the effective electronic mass along the applied field. The direction of the electric field (due to band bending), in turn, depends on the orientation of the photoexcitation surface. Hence the characteristics of photoemission will be orientation dependent, and the results for <111> surface will be different from, say,

the <100> surface. The orientation can also affect the optical absorption coefficient of the sample. The affect of orientation has been taken into account in the simulation and results for different photoexcitation orientations have been obtained.

Apart from the anisotropy in the material parameters such as the effective masses, the presence of conduction band minima at the L- and X-points also imparts a strong orientation dependence. This arises from the overall electronic wavevectors associated with the equivalent L- and X-valleys. When such electrons are incident on a given surface, the magnitude of the transverse momentum depends on the orientation of the particular valley in which they reside. For example, consider two electrons residing within the equivalent [100] and the [010] valleys, to be incident across the [100] emitting surface. The [100] electron has negligible transverse momentum, while that of the [010] equivalent valley electron would approximately be: π/a units. Here "a" is the lattice constant. Since the quantum mechanical transmission probability strongly decreases with the transverse momentum, the prospects of emission for the two incident electrons in the above example would be widely dissimilar. The orientational dependence is expected to be stronger in diamond rather than GaAs, since electrons incident on a GaAs surface would predominantly occupy the low energy, symmetric T-valley.

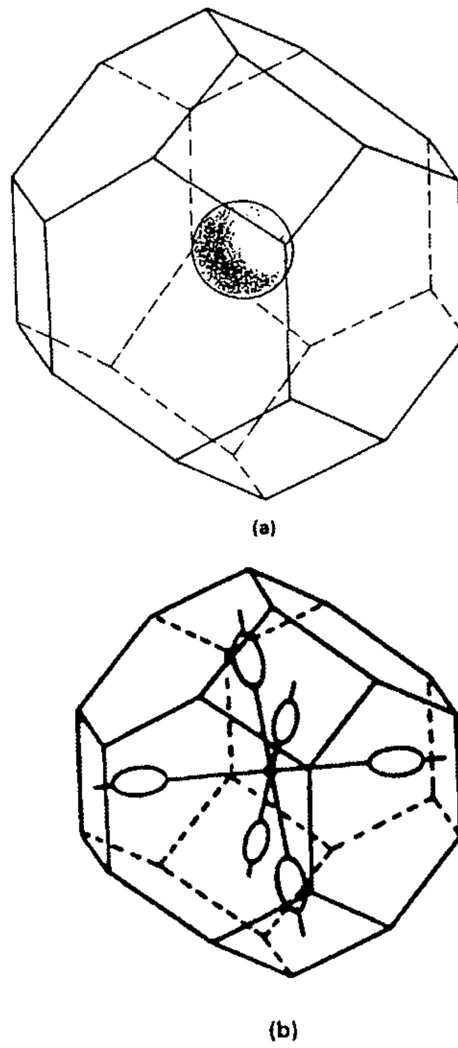

Fig. 3.5 Constant energy surfaces in first Brillouin zone for (a) GaAs and (b) diamond

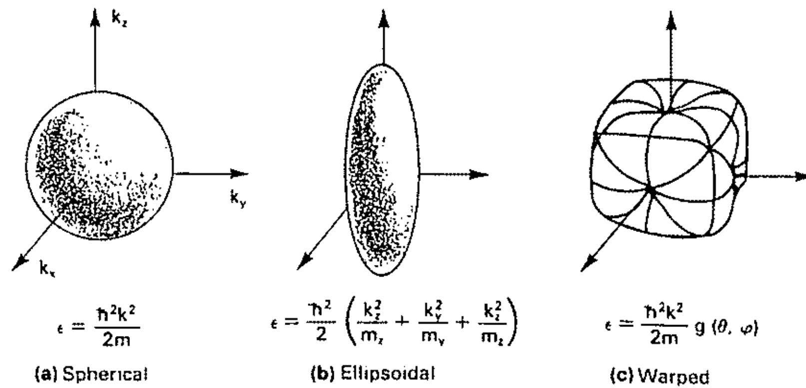

Fig. 3.6 Different shapes of constant energy surfaces and their E-k relationships

CHAPTER 4

RESULTS AND DISCUSSION

4.1 INTRODUCTION

This chapter gives the results of Monte Carlo simulations for NEA photoemission from GaAs and diamond. The calculations were carried out to probe and analyze three specific characteristics of NEA photoemission, namely: (i) The temporal response and sharpness of the emitted electron pulse, (ii) the energy distribution, and (iii) the angular spread of the beam. Since a variety of physical parameters affect the above characteristics, a number of simulations were carried out to explore the effect of each variable. The set of simulation results obtained have been shown in the following sections. The chapter also includes discussion of the results, and explanation of the various features of NEA emission. The potential for NEA photoemission from diamond has also been assessed on the basis of Monte Carlo simulations, and a comparison with GaAs-Cs photoemitters has been carried out. The role of grain boundary scattering on the electronic transport characteristics in polycrystalline diamond has also been evaluated. Such grain boundary effects are expected to become dominant in the less expensive, but more practical polycrystalline diamond material.

4.2 RESULTS FOR GaAs

Monte Carlo simulations were performed to predict and gauge the behavior of three specific output characteristics. These were: the energy distribution, temporal response and angular distribution of emitted electrons. Affect of various parameters, such as the impurity

doping, sample thickness, pulse width, excitation energy and temperature on these NEA photoemission characteristics were simulated. The results for each of these characteristics are discussed next.

4.2.1 ELECTRON ENERGY DISTRIBUTIONS

Energy of electrons emitted across the GaAs surface was obtained from the Monte Carlo simulations developed at 300 K. An energy range between 0.0-1.0 eV was chosen, and the entire interval was divided into 40 boxes of 0.025 eV each. Individual electrons moving within the GaAs were tracked, and energies of those crossing the surface were recorded. These energies were assigned to one of the 40 boxes in order to construct a histogram. The number of emitted electrons was then plotted against energy. The plots thus obtained, illustrate the effect on the energy distribution, produced by varying some of the input parameters.

Figure 4.1 shows the affect of impurity doping on the energy distribution of emitted electrons for the case of reflective mode photoemission. A 1.55 eV, 0.05 ps laser pulse was assumed to photogenerate the electrons internally within a 10 μm device. The 1.55 eV energy is close to the band edge, and was chosen since it is of interest for producing spin-polarized electrons in GaAs. The characteristic photon absorption length at this energy is 1.66 μm. Doping levels of 10^{18} cm^{-3} and 5 x $10^{18} cm^{-3}$ were used, and are typically of the values encountered in actual samples. As seen from the plot, an increase in the p-doping of GaAs leads to a decrease in the peak by about 20%, and a slight broadening of the distribution. The energy broadening is a direct result of increased impurity scattering which works to randomize the momentum. Increase in the sample doping also has the effect of reducing the

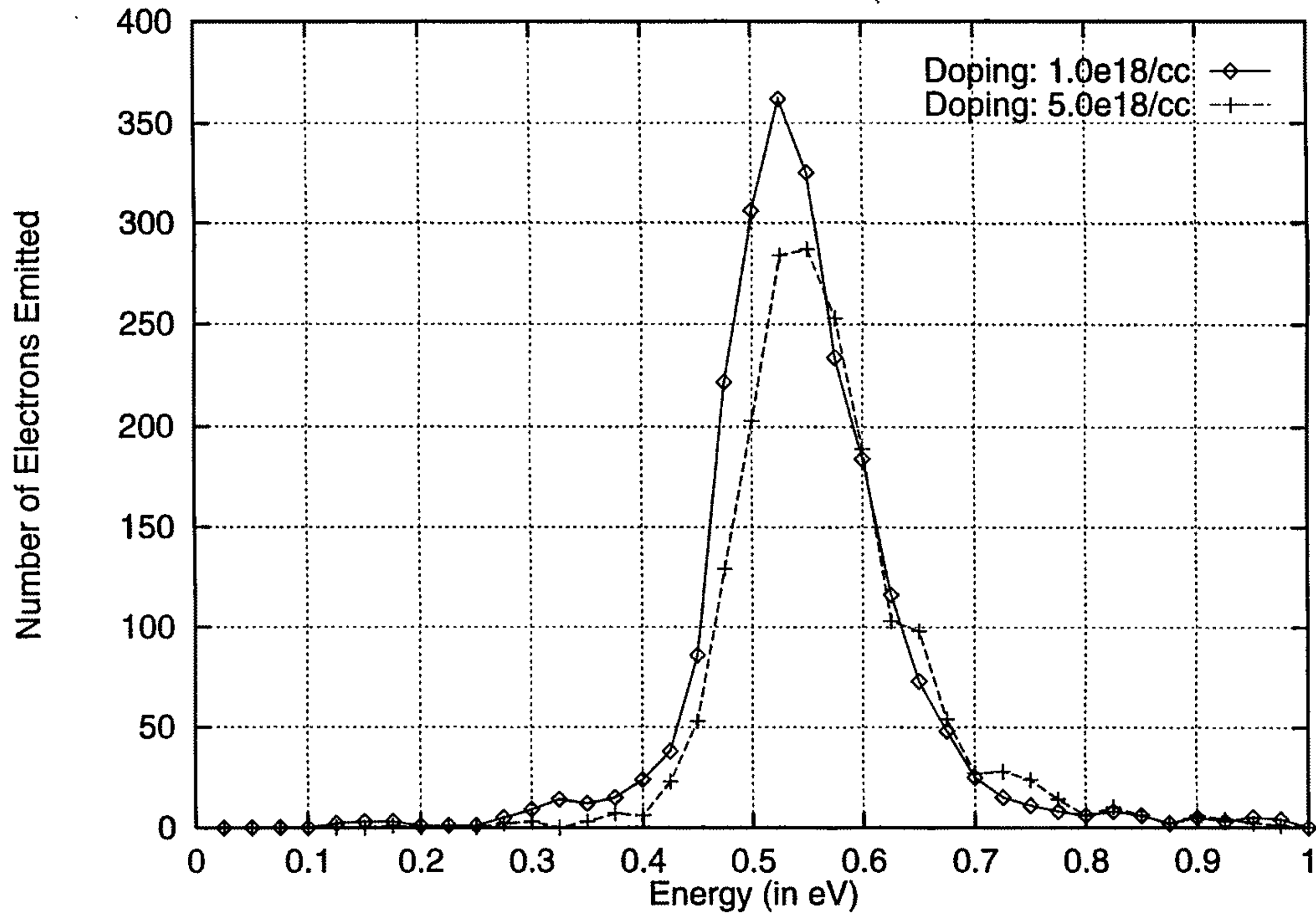

Fig. 4.1 Energy distribution (ED) for reflective mode (RM) at 300K for sample thickness of 10μm, photon energy of 1.55eV and pulse width of 0.05 ps

width of the band-bending region. As a result, a lower fraction of electrons are within the space charge region near the surface. This leads to a decrease in the number of electrons that encounter the electric field and get swept towards the emitting surface. The outcoming flux is therefore smaller. Figure 4.2 shows the effect of varying sample thickness on the energy distribution for a reflective mode NEA device for the same 1.55 eV, 0.05 ps photogenerating pulse. The peak of the distribution reduces by a small amount as the sample thickness is increased from 10 μm to 25 μm. Increase in sample thickness causes electrons to travel a longer distance, on an average, before they can get to the sample boundary. This longer traversal time results in greater number of collisions and energy losses, on an average. This has two consequences: (a) A slightly lower number of electrons are able to get across the sample and be collected across the surface in a given time, and (b) the most frequently occurring energy cannot be preserved as easily within the electron swarm. The peak energy, therefore, shifts to a lower magnitude in case of a thicker sample as obtained in figure 4.2. However, the shifts obtained between the two samples are not very strong because the characteristic absorption length at 1.55 eV is relatively small in comparison to the device dimensions. At lower photon energies, the absorption lengths would be much larger, and could lie between the 10 μm and 25 μm device lengths. In such a situation, one would expect to find a much stronger reduction in the number of emitted electrons for the 25 μm sample. Figure 4.3 shows the energy distribution for reflective mode NEA obtained by varying the pulse width of the photogenerating laser. Laser pulses of 0.01 ps and 0.05 ps were assumed at 1.55 eV for a 10 μm sample. The results show that the energy distribution is not a strongly dependent on the pulse width and the effects are almost negligible. Logically, one expects

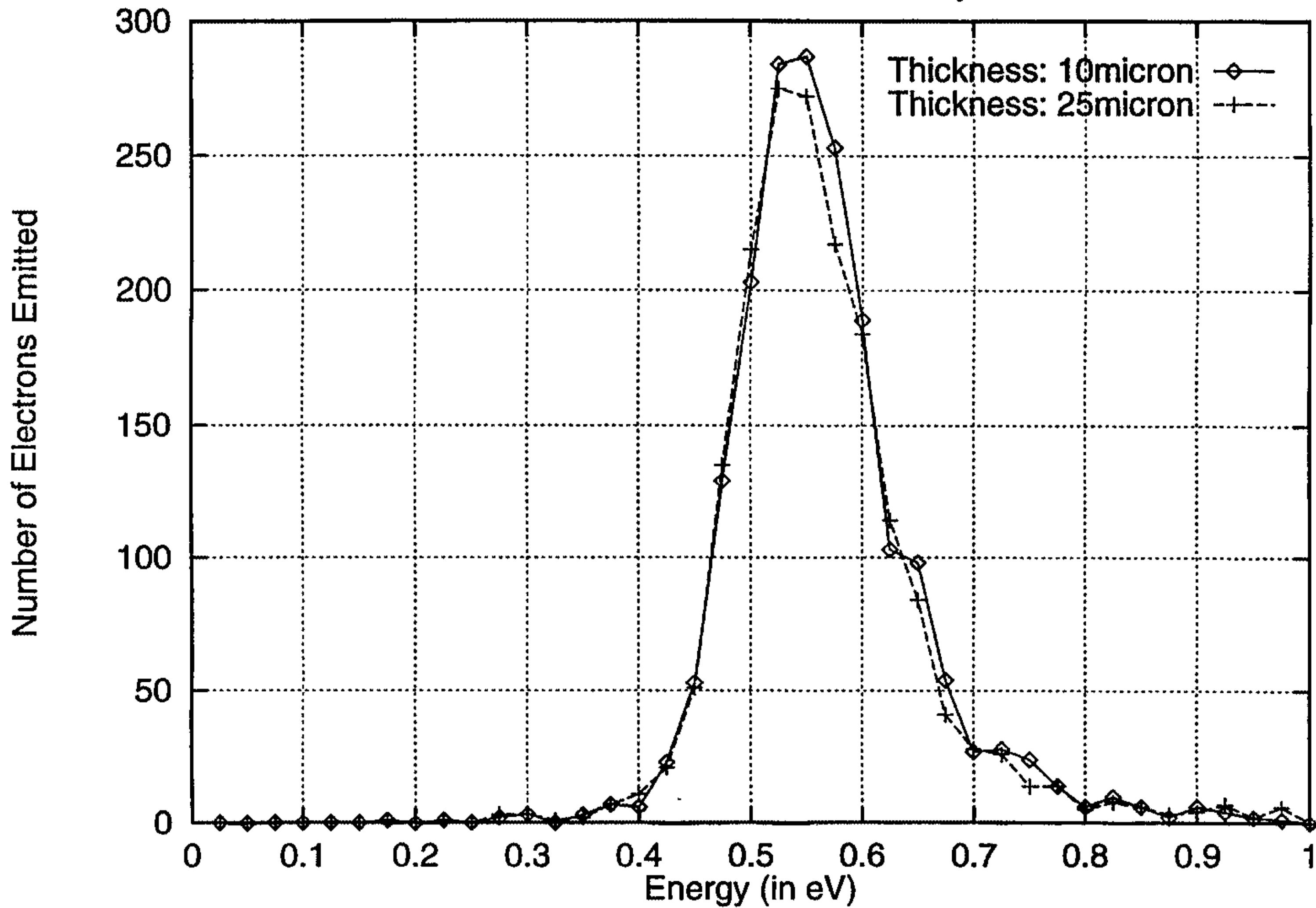

Fig 4.2 Energy distribution (ED) for RM for sample doping of $5\times10^{18}\,cm^{-3}$ and pulse width of 0.05 ps .

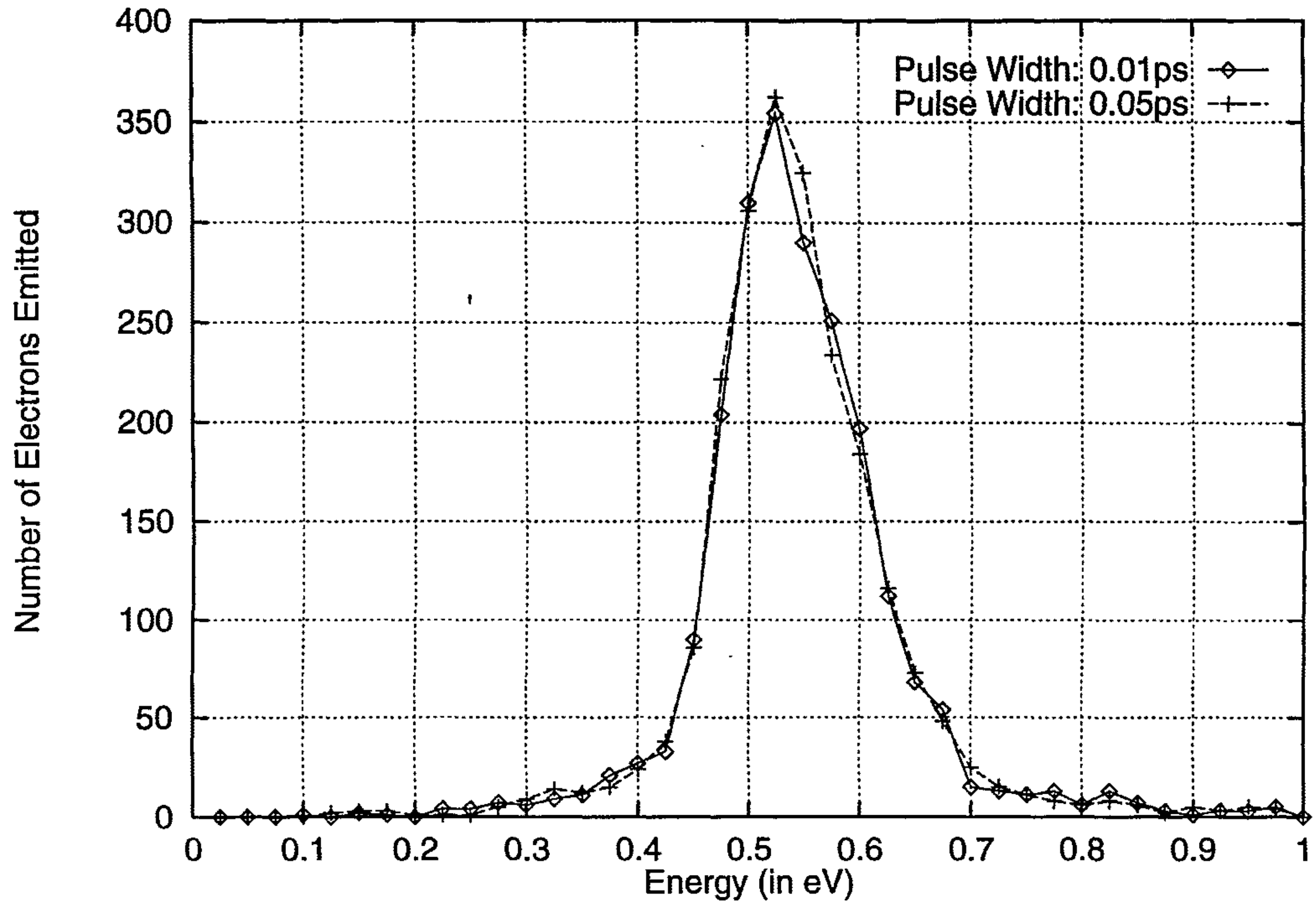

Fig 4.3 ED for RM for thickness of 10μm

such behavior as long as the pulse widths remain substantially lower than the average electron transit time to the surface following bulk generation.

Next, a discussion of the energy distribution for transmission mode photoemission is presented. Figure 4.4 shows the energy distribution for two values of doping at 300 K for 1 μm samples. The samples were assumed to be p-type with concentrations of 10^{18} cm^{-3} and 5 x 10^{18} cm^{-3}. As for the reflective mode case, an increase in the doping is seen to reduce the peak amplitude. The effect, however, is more pronounced in case of the transmission mode as evident from a comparison of figures 4.1 and 4.4. This more pronounced effect for the transmission mode is associated with the spatial location of electronic photogeneration. In the transmission mode, electrons are generated close to the back surface of the sample, rather than the front face. As a result, they need to travel a much longer distance before they can reach the front surface and get emitted. This longer transit magnifies the effect of increased ionized impurity and phonon scattering. Furthermore, the collection efficiency suffers at the higher doping for two reasons. The first is due to the smaller space charge region associated with a larger doping. Consequently, a lower fraction of photogenerated electrons are able to be swept towards the surface. Secondly, the higher probability of a scattering event related with the longer transit time, tends to make the flow less "streamlined". This again reduces the collection efficiency, leading to lower numbers of emitted electrons at higher doping.

Figure 4.5 (a) and (b) show the result of increasing the sample thickness from 1μm to 2μm, and from 2μm to 3μm for a transmission mode device. A 1.55 eV, 0.05 ps pulse was again chosen with a sample doping of 10^{18} cm^{-3}. In this mode, the average distance travelled by the electrons (and hence the number of scattering events) before being emitted out, is roughly proportional to the sample thickness. Hence, even a small increase in the thickness

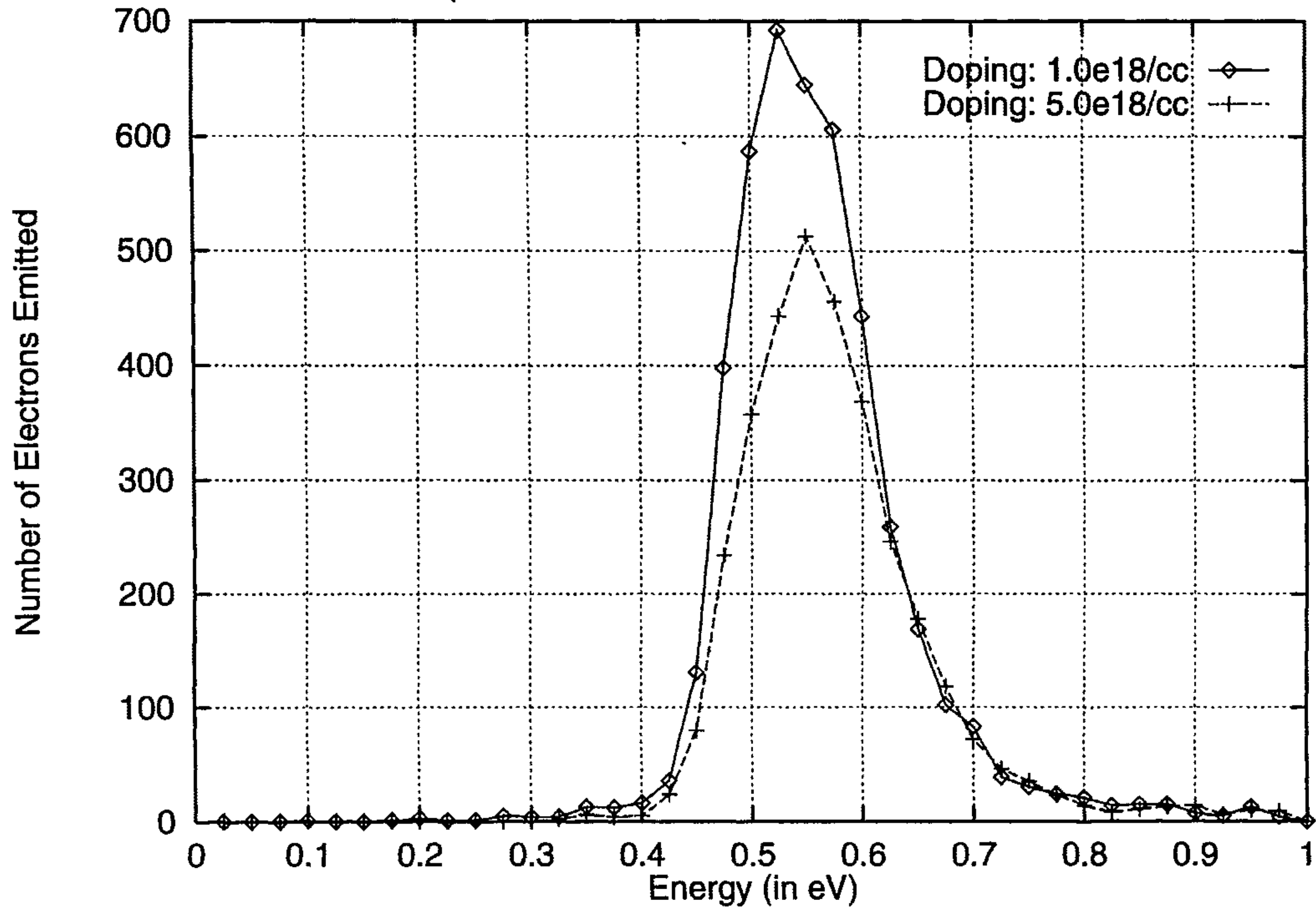

Fi.g 4.4 ED for transmission mode (TM) for sample thickness of 1μm and pulse width of 0.01 ps

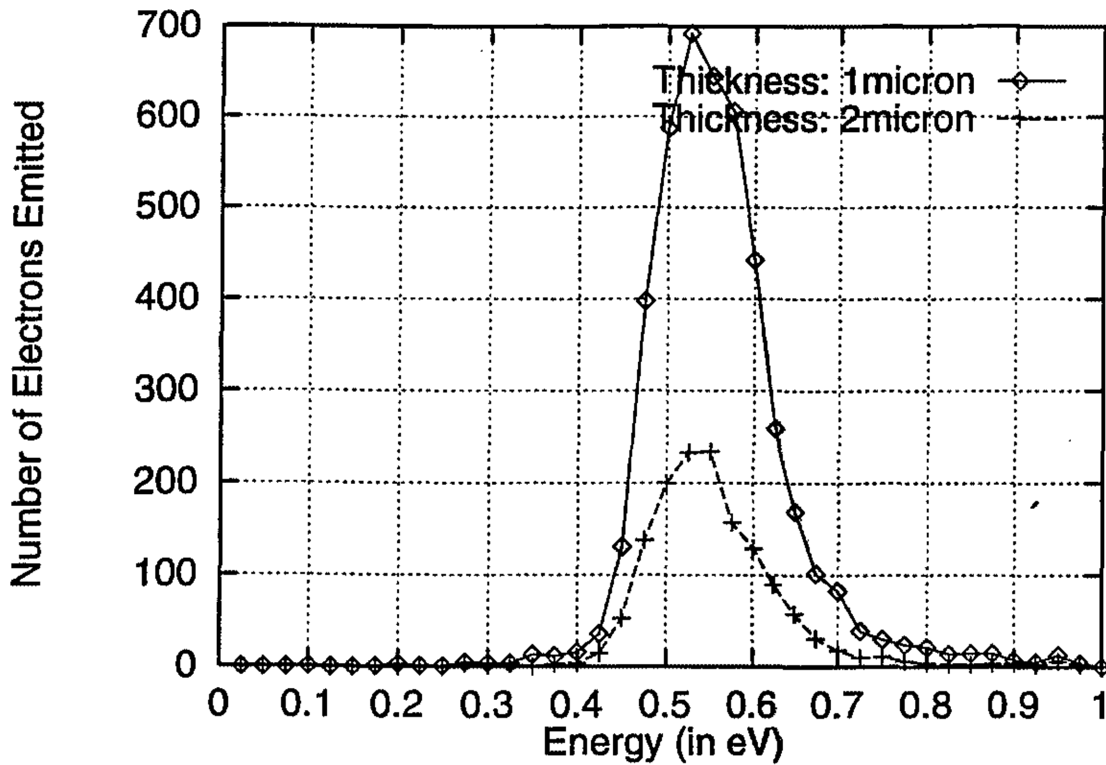

Fig 4.5(a) ED for TM for sample doping of $1\times10^{18}cm^{-3}$

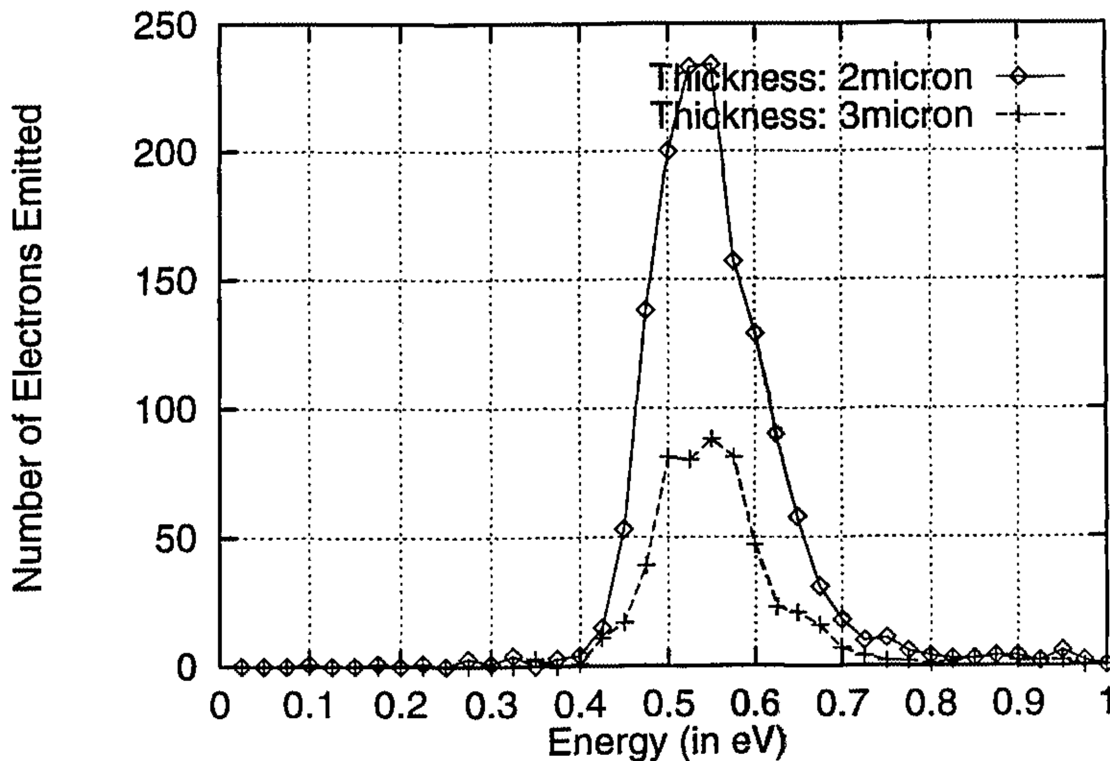

Fig 4.5(b) ED for TM for sample doping of $1\times10^{18}cm^{-3}$

results in a substantially larger randomization of the carrier energies. Consequently, the energy distribution of the emitted particles can be expected to have a less sharp and "peaky" characteristic. Furthermore, the number of electrons emitted from the surface during a specific time interval, would become smaller as the transit time increased. For a thicker device, one therefore expects fewer electrons to come out during a given time span. This result is seen in the curves of figures 4.5a and 4.5b which were obtained by running the simulations for 10 ps. For a much larger 10 μm sample, Monte Carlo simulations carried out to 10 ps did not yield any electron emission from the sample. Apart from the longer transit time, a thicker sample also causes the electrons to lose greater energy during their transit towards the surface. As a result, the fraction of electrons with sufficient energy to cross the potential barrier at the boundary would be lower for a longer device. This would contribute to a smaller number of electronic emissions. It may also be mentioned, that the above trends would continue to hold for larger photon energies, since the characteristic absorption lengths continue to decrease. For very small, near band-edge excitation, on the other hand, differences due to variations in the sample lengths would be much less pronounced. This would occur because the absorption lengths would be much larger, perhaps approaching the device dimension. Finally, figure 4.6 shows that the pulse width does not have a perceptible effect on the energy distribution even for the transmission mode. This result is expected to hold for as long as the pulse width was smaller than the average transit time across the device.

As evident from the previous plots, the peak kinetic energies of the out-going electrons for 1.55 eV photoexcitation occur approximately at 0.55 eV. Furthermore, the full width at half maxima (FWHM) spread in energies is roughly 150 meV. These results hold

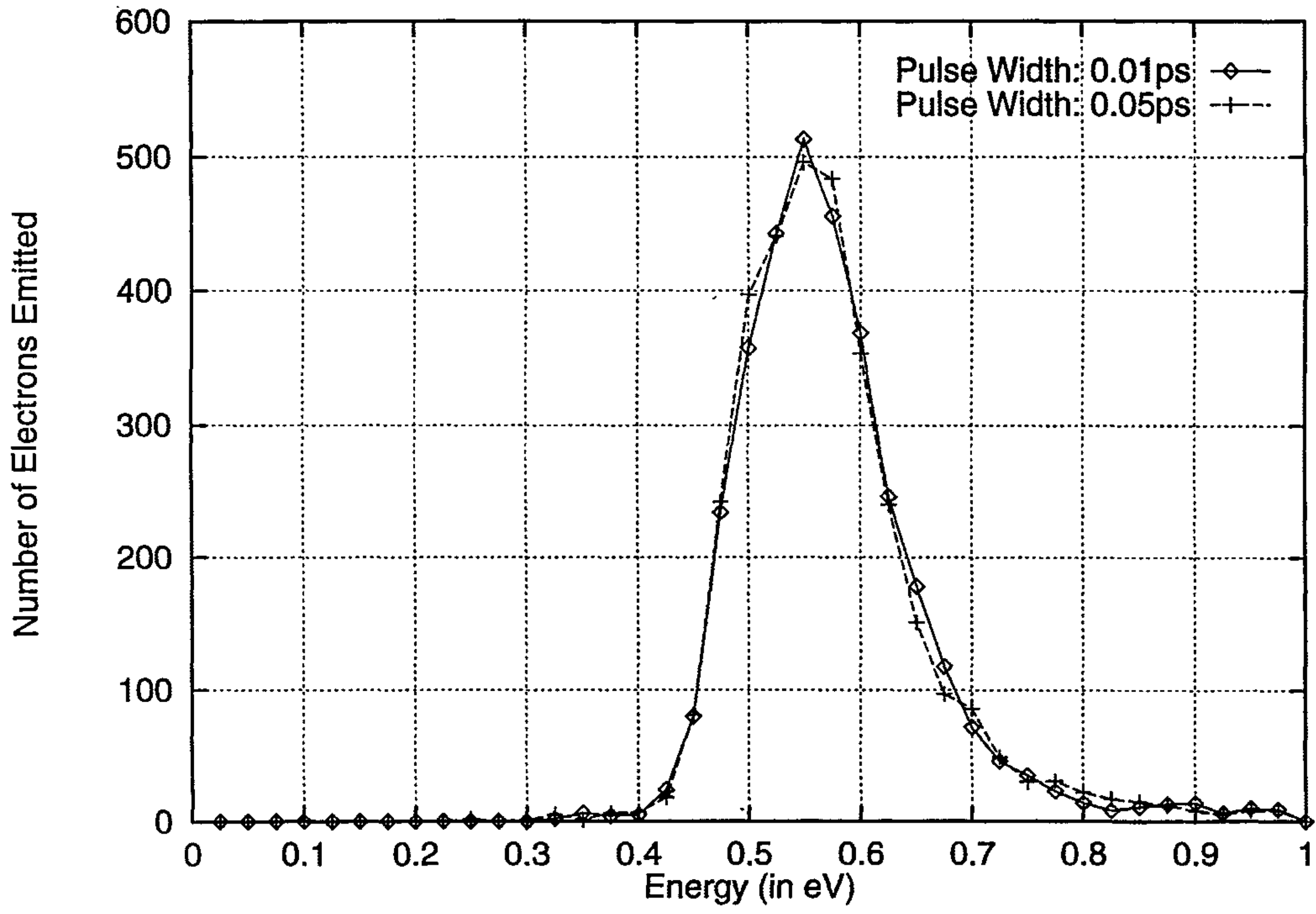

Fig. 4.6 ED for TM for sample thickness of 1μm

for both the reflection and transmission modes. The Monte Carlo numerical values of the peak energy and its spread, are very close to the experimental data that have been obtained for GaAs [29,33]. This close agreement between theory and measurements validates the present numerical model and simulation scheme.

4.2.2 TEMPORAL RESPONSE CHARACTERISTICS

The temporal response characteristics of the GaAs NEA photoemitter were examined next. Data was obtained from Monte Carlo simulations by recording the time to emission for each electron following initial photogeneration. The simulation was carried out for a sufficiently long time (10 ps or 20 ps) to establish a sufficiently large population of outcoming electrons. This was necessary to ensure that the information provided by the results was accurate and statistically meaningful. The entire time duration was divided into 40 equal time intervals with each slot being 0.25 ps or 0.5 ps (for the 10ps or 20 ps simulations.) The number of electrons emitted in each time interval was then plotted against time. The various temporal response curves shown next, reveal the effect of one or more input parameters on the output characteristics.

First we discuss the reflective mode NEA emission. Figure 4.7 shows the effect of doping on the temporal response for a 1.55 eV, 0.05 laser excitation on a 10 μm sample. The doping levels were 10^{18} cm^{-3} and 5 x 10^{18} cm^{-3}. Reasons for the reduced number of emitted electrons at the higher doping have already been discussed in the previous section. Most of the reductions appear to be during the initial times following photogeneration. This is to be expected, since emissions at the early times are due to electrons generated closest to the surface. Such electrons are most strongly influenced by details of the internal electric field,

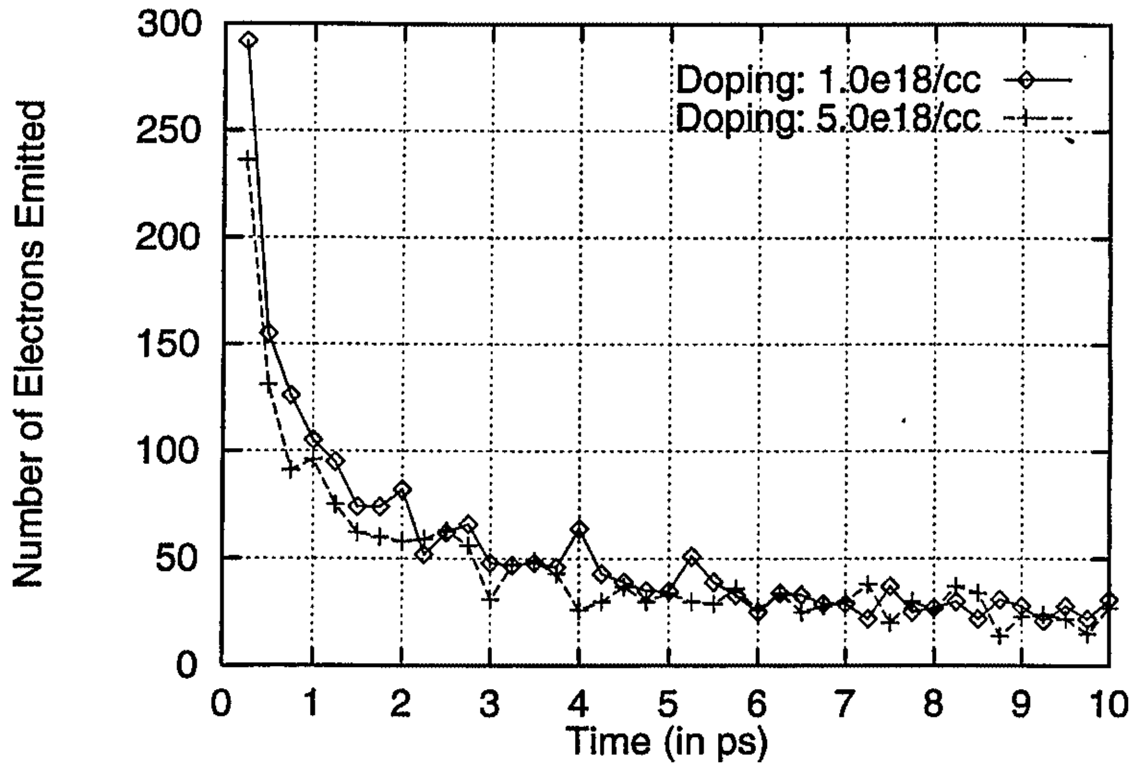

Fig 4.7 Effect of doping on temporal response (TR) for a 10μm thick sample in RM

which primarily exists near the surface. Consequently, variations in the electric field distribution, as brought about by changes in the doping concentration, strongly affect only those carriers that are closest to the surface. This translates into an observable density dependent change in the relative emission flux during the early times. Figure 4.8, obtained for a 1.55 eV, 0.05 ps laser pulse at 300 K shows that the response of the photoemitter becomes slower as the sample thickness is increased from 1 μm to 10 μm. Increasing the thickness causes the electrons to travel a larger distance as more carriers are photogenerated deeper into the device. Hence, it takes the electrons a longer time to reach the photoemission boundary. One expects this argument to hold as long as the sample thickness was smaller than or comparable to the characteristic absorption length of the incoming photons. The absorption length L_a for the 1.55 eV energy in GaAs is roughly 1.66 μm, and hence the transit times do increase substantially as the sample thickness increases from 1 μm to a value much longer than L_a.

Figure 4.9 shows that increasing pulse width from 0.01 ps to 0.05 ps does not substantially affect the temporal response for the reflection mode. This result is in keeping with the arguments given previously, and should hold as long as the pulse width was smaller than the average transit time. Figure 4.10 shows the impact of increasing the pulse energy from 1.55 eV to 2.1 eV, on the temporal response for reflection mode operation. The sample was taken to be 1 μm, with a doping of 10^{18} cm^{-3}. The results shown can be understood in terms of the energy-dependent absorption length. The characteristic absorption length L_a decreases with increasing photon energy, and roughly equals 1.66 μm at 1.55 eV and 0.6 μm at 2.1 eV. As a result, electrons generated by the 2.1 eV photons tend to be located nearer the surface, as compared to those created by the 1.55 eV photons. The transit time is therefore

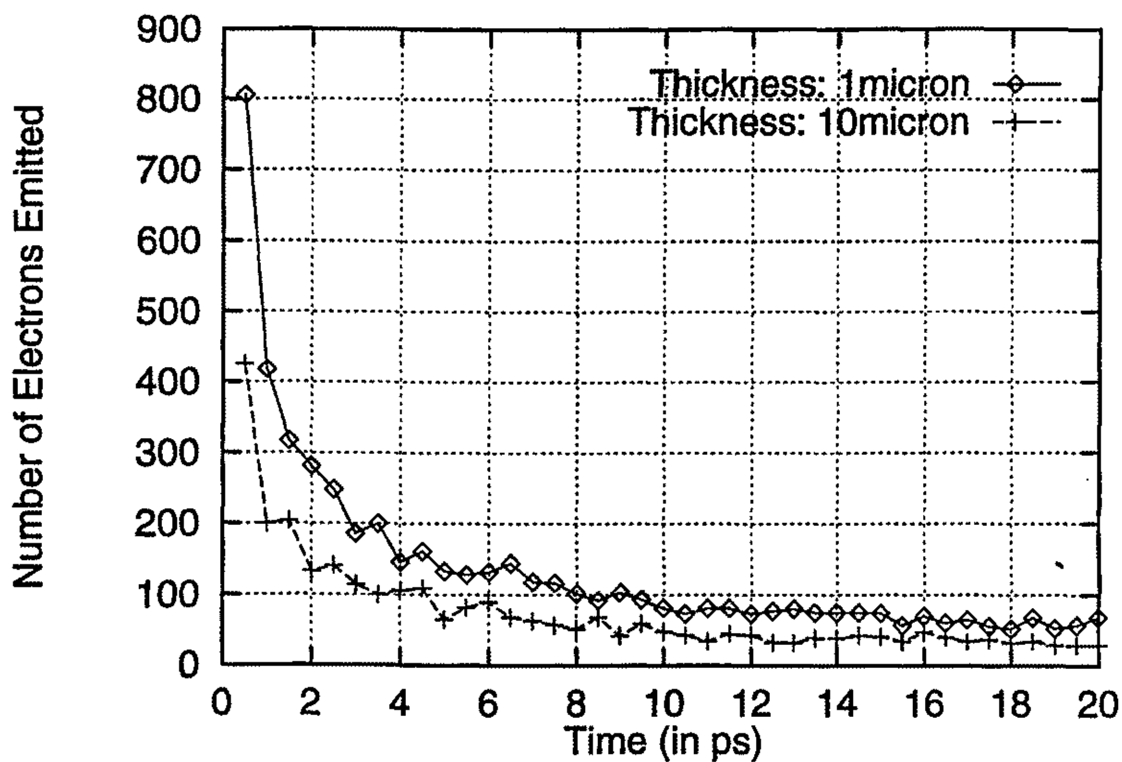

Fig. 4.8 Effect of sample thickness on TR for sample in RM

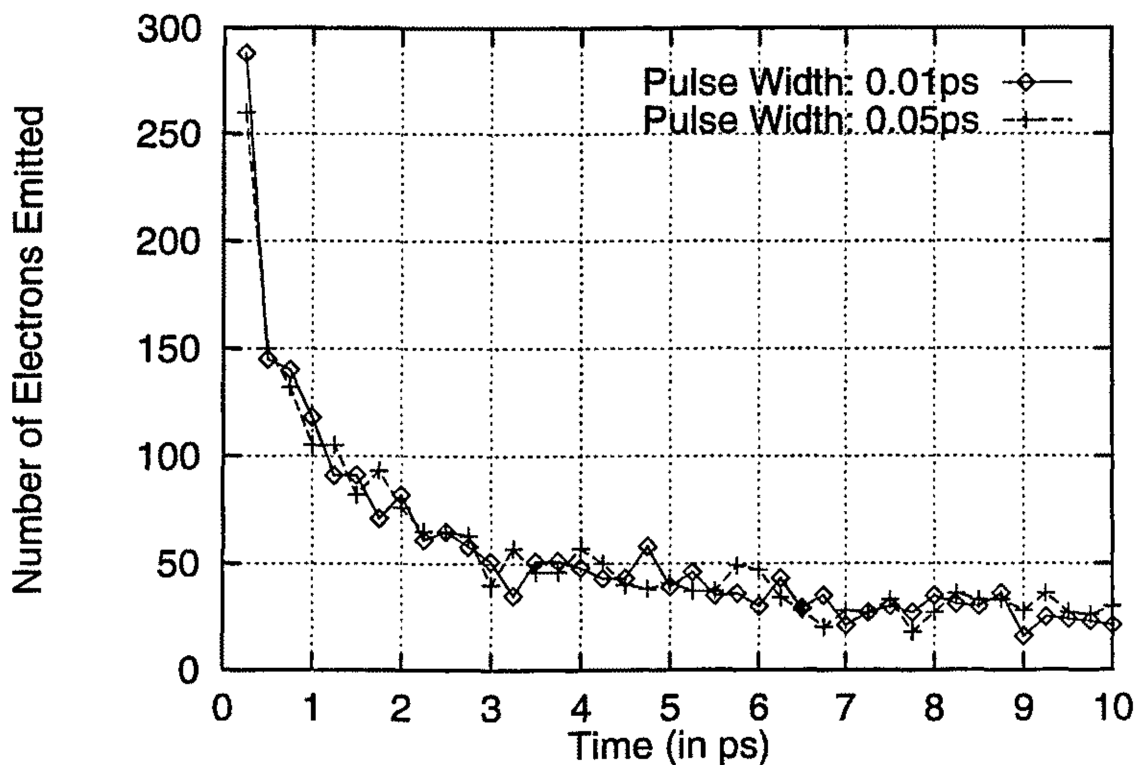

Fig. 4.9 Effect of pulse width on TR for 25μm sample in RM

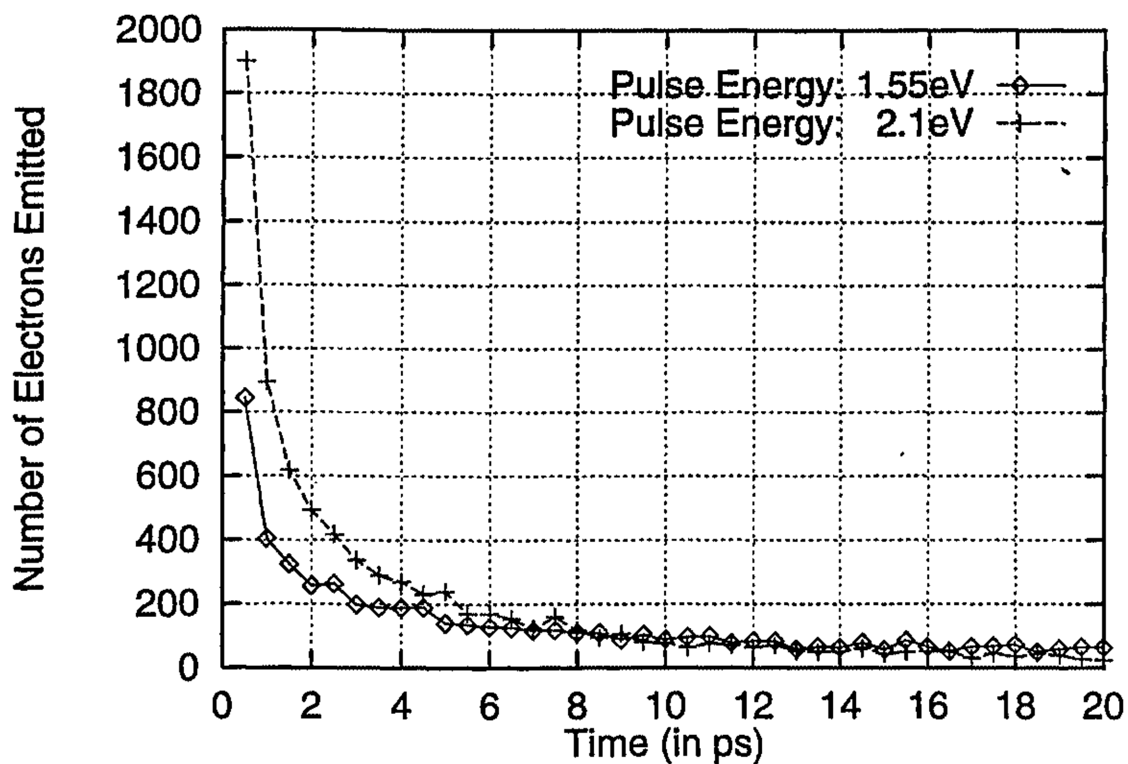

Fig. 4.10 Impact of increasing pulse energy on TR in reflective mode

less, and the average electric field experienced by electrons substantially greater for the 2.1 eV case. This results is a faster response at 2.1 eV with a larger number of emitted electrons. Furthermore, at 2.1 eV the carriers tend to have a higher energy than those generated by the 1.55 eV pulse. This increases the transmission probability over the potential barrier at the surface, and again works to enhance the flux of emitted electrons.

In case of the transmission mode, changes in the doping concentration also appear to produce changes in the temporal response, as shown in figure 4.11. The sample thickness was taken to be 1 μm, while the photon energy was 1.55 eV at a pulse width of 0.05 ps. As already noted, large sample dimensions are not appropriate for quick emission if the material is to be operated in the unbiased transmission mode. The absence of an electric field at the absorbing back-surface, delays the emission process and leads to low emission flux densities. For the 1 μm sample of figure 4.11, higher flux densities are seen to result at the higher doping. This, as previously discussed, is the result of higher electric fields and their larger spread into the device.

The effect of varying sample thickness for the transmission mode for 1.55 eV excitation is shown in figures 4.12 and 4.13. The reason, as mentioned previously, is the increased distance that the electrons must travel in order to reach the photoemission boundary. The pulse width was not seen to play an important role in dictating the temporal response, and hence the relevant plot has not been included here. The effect of pulse energy on the temporal response has been shown in figure 4.14 for a 10 μm device. As the pulse energy is increased, the absorption length is reduced. This causes more electrons to be generated near the non-emitting back-surface of the sample. These electrons take a much longer time to reach the photoemission surface. Hence, as seen in figure 4.14, the electronic

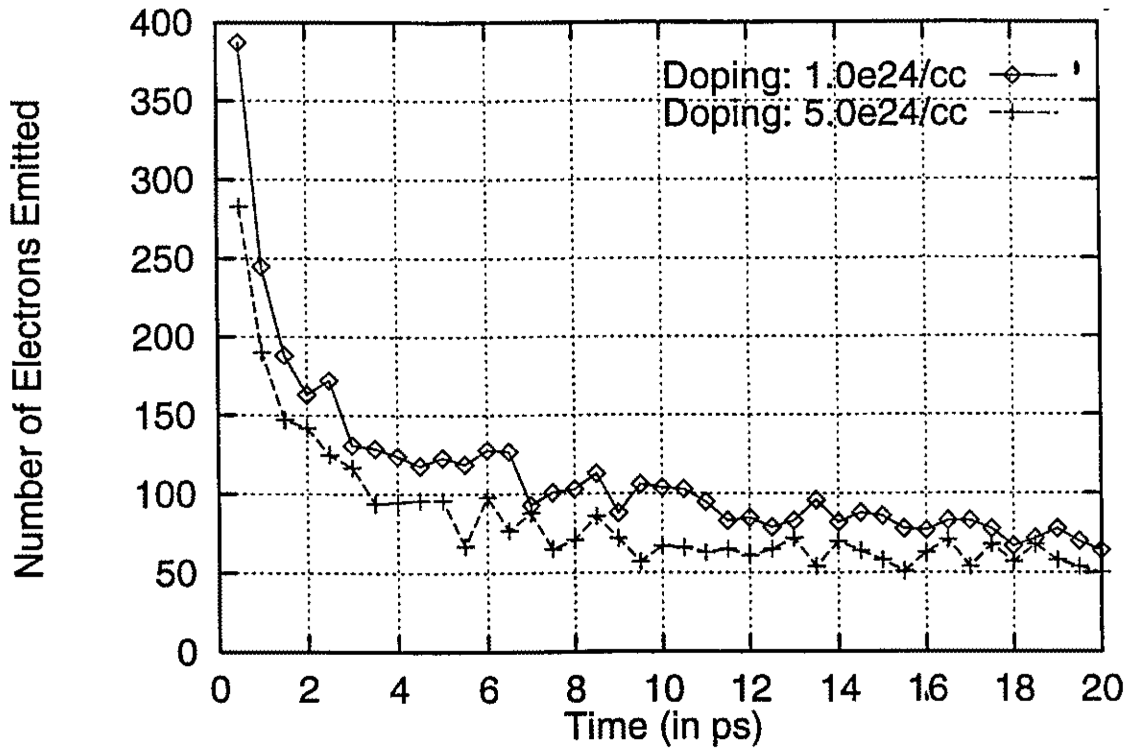

Fig. 4.11 Effect of doping on TR from a 1μm sample in TM .

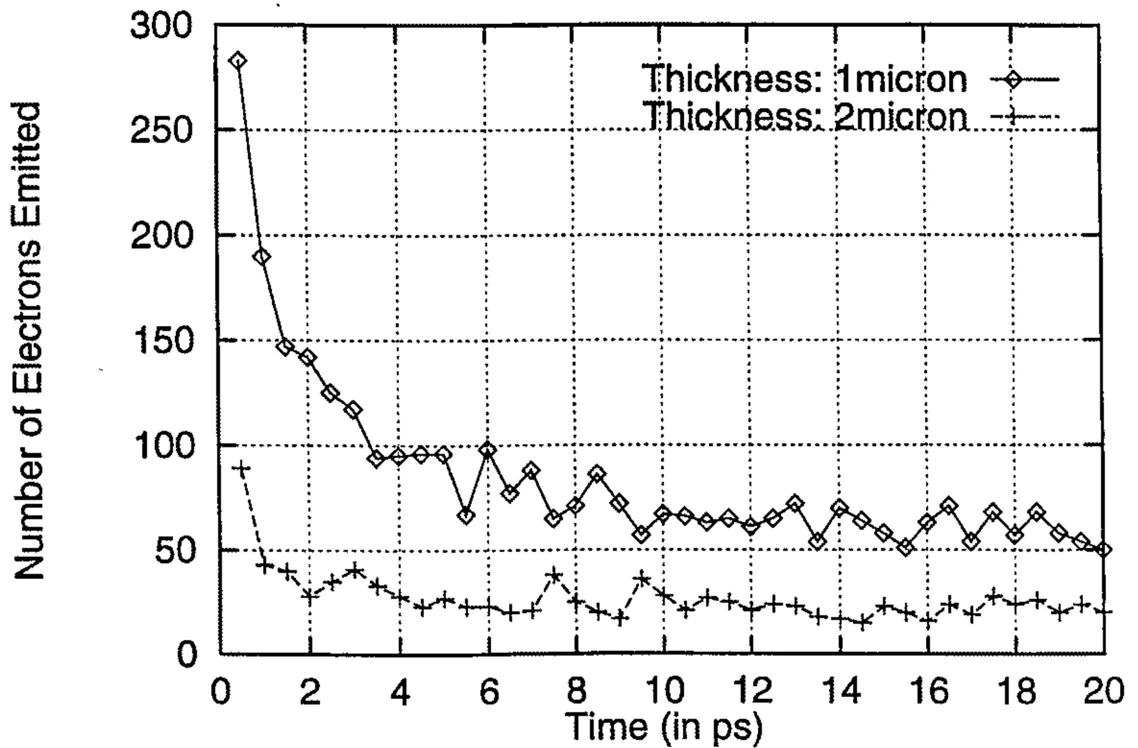

Fig. 4.12 Effect of varying sample thickness on TR in case of TM

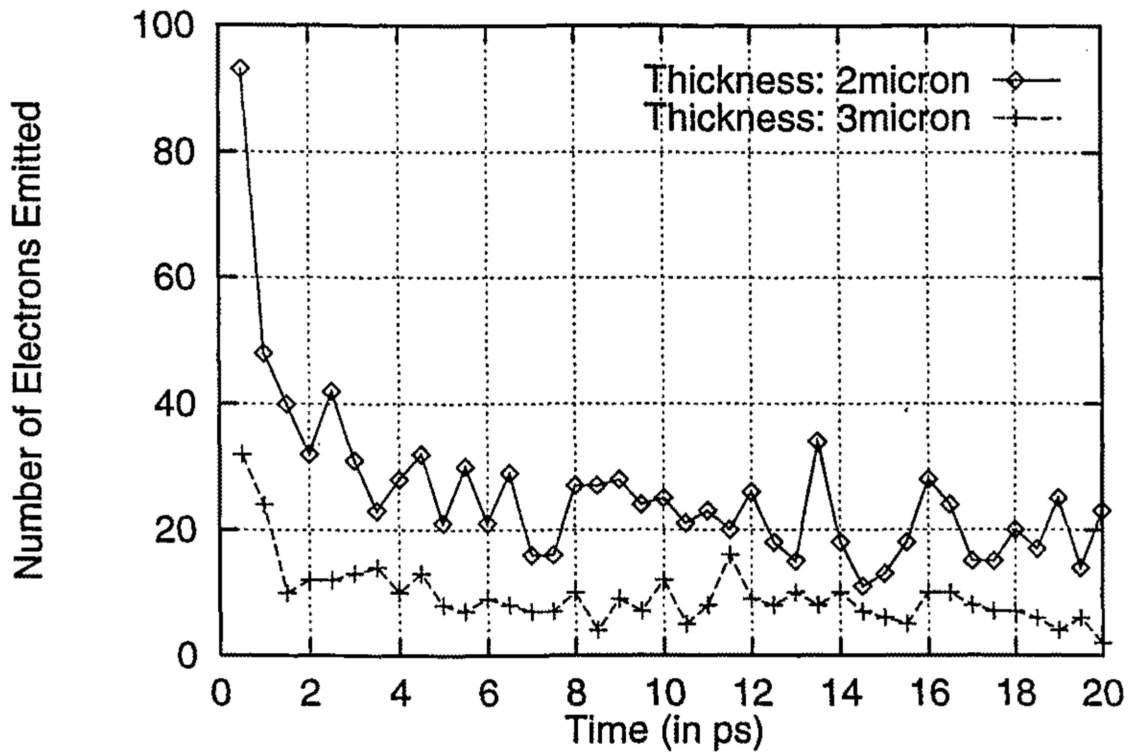

Fig. 4.13 Effect of varying sample thickness on TR in case of TM

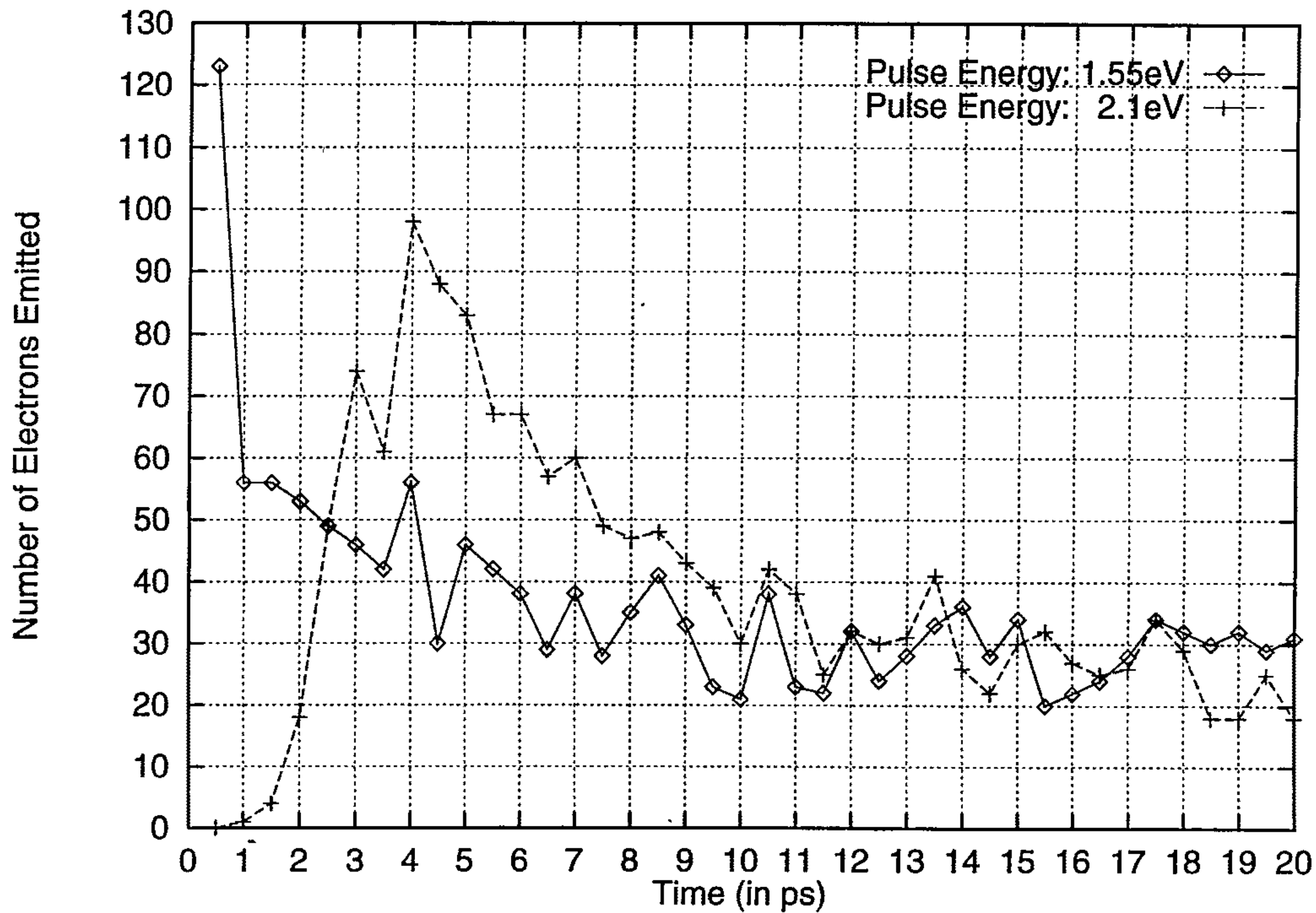

Fig. 4.14 Effect of pulse energy on TR for a 10 μm sample in TM

emission at the front surface does not begin for the 2.1 eV case, until about 1.5 ps after the initial laser pulse. Consequently, the emitted electron pulse gets "delayed" as the photon energy is increased from 1.55 eV to 2.1 eV. Also, at both photon energies, the emitted electron beams are seen to have a relatively long lived "tails" in their temporal distribution. This suggests that operating NEA photoemitters in the transmission mode is detrimental to the formation of narrow electron-beam pulses.

As evident from the plots for the various transmission mode cases presented, the temporal response consists of an initial rapid emission burst over the first 2-3 ps, followed by a long "tail" lasting well beyond 10 ps. The tail is due to quasi-thermalized electrons, while the initial burst corresponds to near-ballistic transport of carriers generated near the surface. Such "tails" would not only lower the frequency response of related electron beam devices, but would also be detrimental for mono-energetic distributions. Such mono-energetic electrons are necessary for a number of applications, including spectroscopy and free-electron lasers. Figure 4.15 compares the temporal response of reflective and transmission modes. Less number of electrons get emitted in case of transmission mode, as explained earlier.

4.2.3 ANGULAR RESPONSE

The angular distribution of the emitted electrons normal to the emitting surface was also recorded. For convenience, the z-axis was assumed to be the outward normal. The number of electrons emitted was plotted against the corresponding angle (in radians) they made with respect to the z-axis. Figures 4.16 and 4.17 show the angular distribution of the emitted electrons for reflective and transmission mode respectively. As we can see, the peak

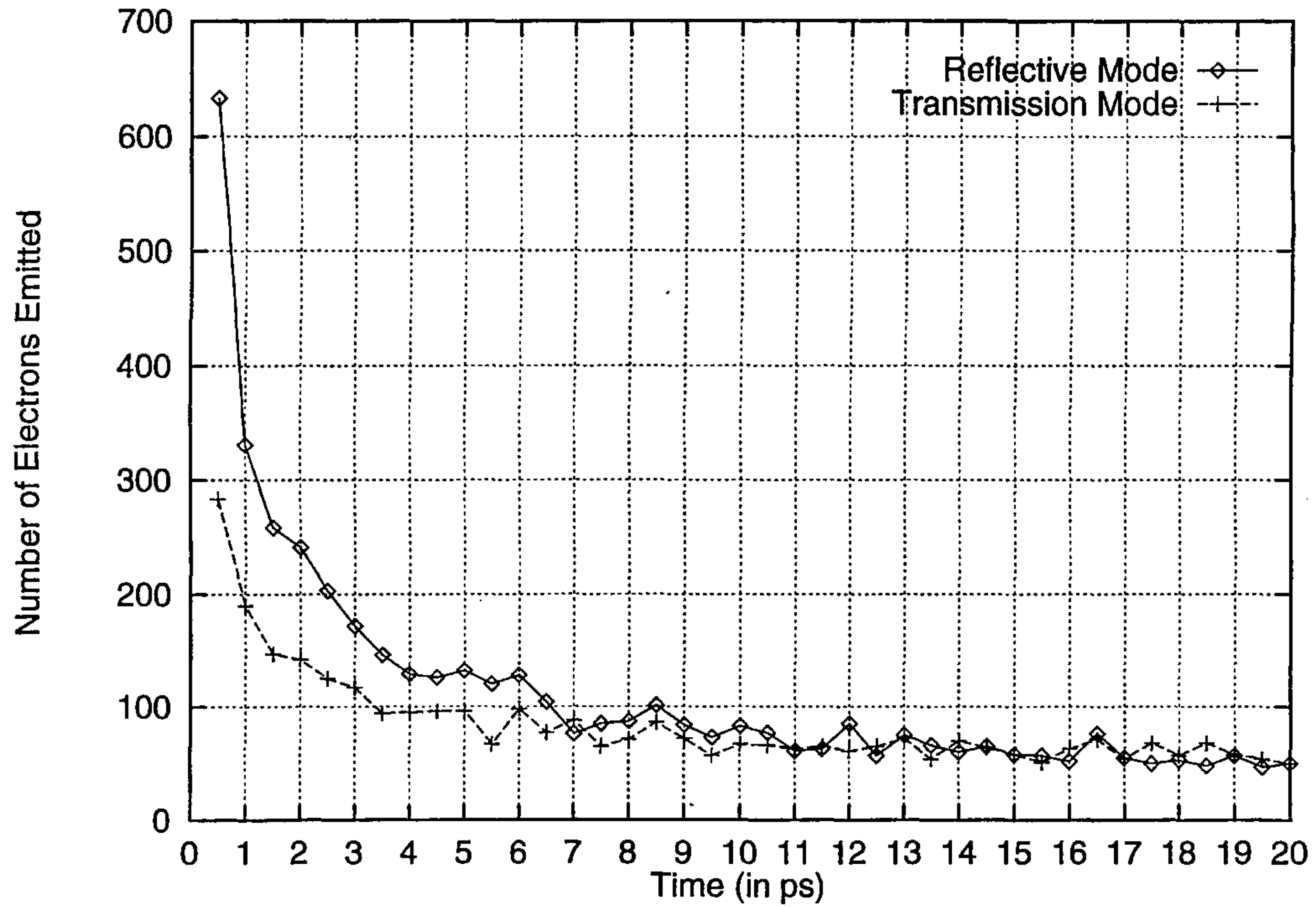

Fig. 4.15 Comparison of TR of a sample in RM and TM

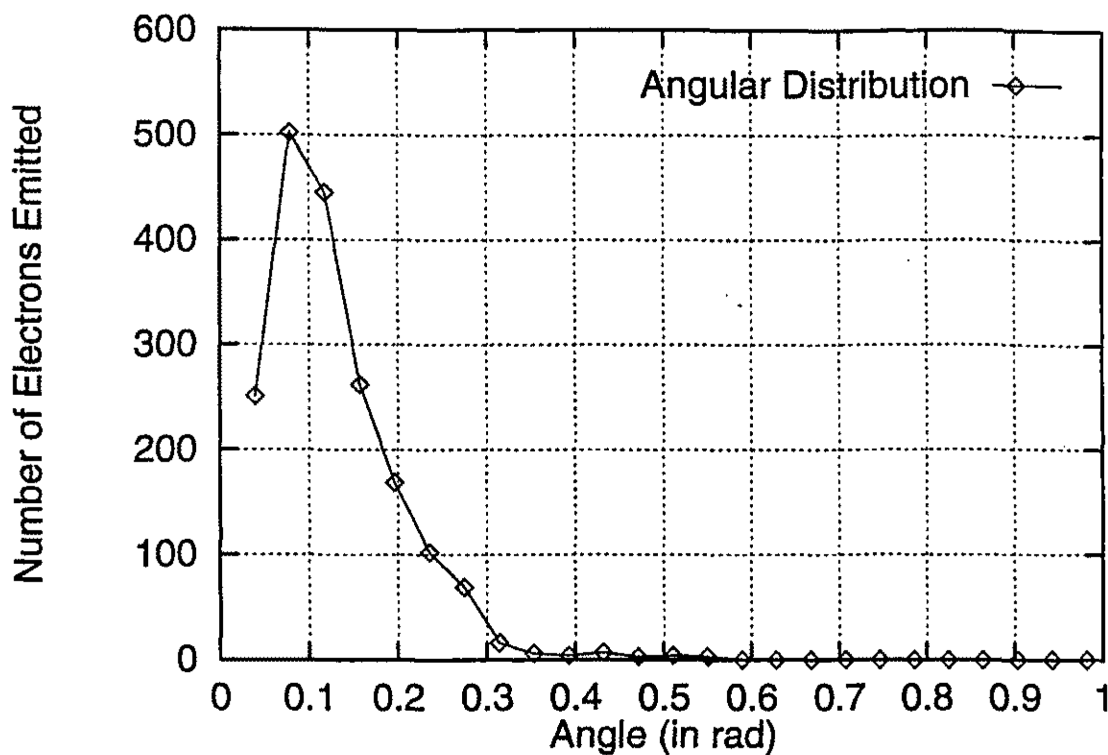

Fig. 4.16 Angular distribution for 10 µm sample in RM .

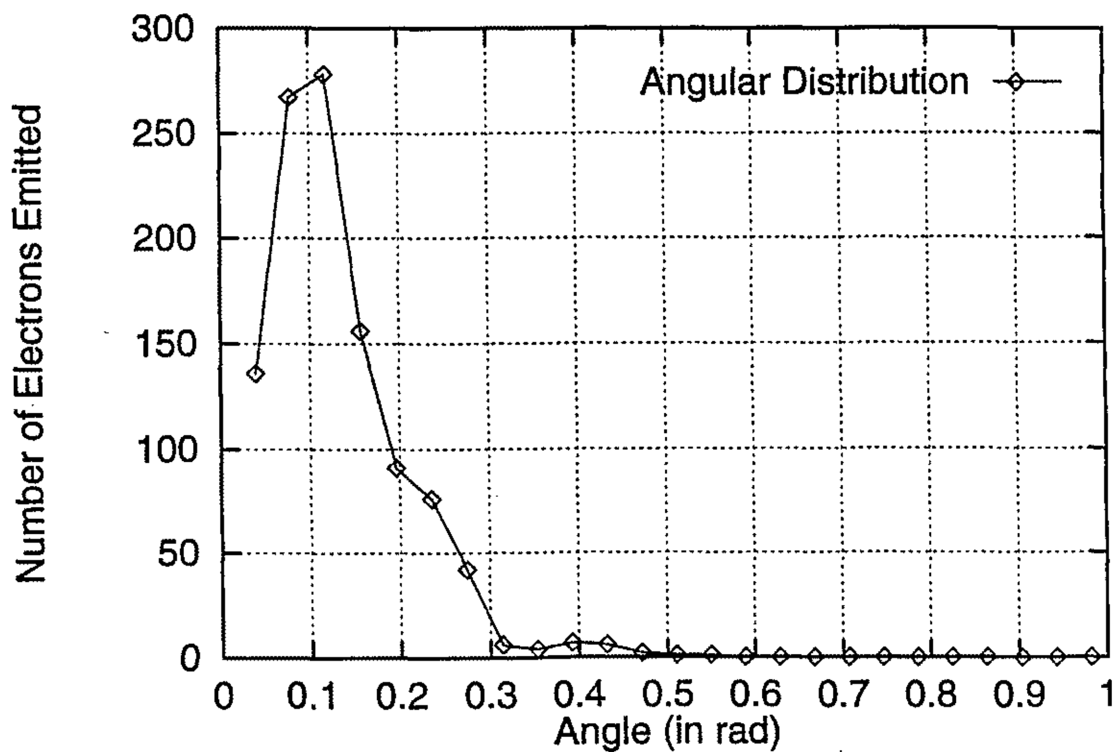

Fig. 4.17 Angular distribution for 2 µm sample in TM

in the angular distribution occurs around 5° and the spread is about 10°. This spread is due to internal scattering and requirement of conserving momentum parallel to the surface. The simulations therefore predict that the emergent beam would be quite narrow with a small angular divergence.

4.3 SIMULATION RESULTS FOR DIAMOND

4.3.1 GRAIN BOUNDARY EFFECTS IN POLYCRYSTALLINE DIAMOND

Recent improvements in the growth of synthetic diamond films have enhanced the practical utility of the material [56]. However, the films grown by Chemical Vapour Deposition (CVD) have been polycrystalline in nature. The measured electrical properties of the CVD films have generally been inferior to those of natural diamond [53], and have shown strong finite size effects. For example, free carrier mobilities were found to be lower in thin film diamond, and strongly dependent on the grain size and film thickness [27]. Experimental data has also shown that carrier mobility increases with temperature for operation below 300 Kelvin [59,60] at a rate greater than the $T^{1.5}$ dependence characteristic of ionized impurity scattering. This finding suggests that electronic transport in polycrystalline diamond is strongly influenced by scattering mechanisms other than those normally encountered in natural diamond not containing grain boundaries.

Since synthetic diamond is relatively inexpensive, it remains the only viable alternative for device fabrication. It will therefore be the only practical option for diamond photoemitters. Realistic evaluations of the characteristics of such polycrystalline diamond photoemitters, necessitate the inclusion of effects associated with the grain boundaries. The presence of such granular material is expected to influence the electron transport and modify

the high field drift velocity characteristics. Monte Carlo simulations were therefore performed to predict the high field transport behavior in such polycrystalline material. These characteristics were subsequently used while simulating the photoemission behavior of NEA diamond.

Analysis of the high field electron drift velocity at 300 K in polycrystalline diamond was based on a formulation discussed in chapter 3. Basically, an additional velocity dependent scattering mechanism was incorporated to account for the presence of grain boundaries. Results of the electron drift velocity for electric fields along the <111> direction, obtained from Monte Carlo simulations are shown in figure 4.18. The field dependent behavior of crystalline diamond was compared to that of polycrystalline material having an average grain size of 0.75 micron. The strength "S" of the grain boundary scattering potential was taken to be 30 eVÅ, and with a standard deviation σ of 0.1 μm. The results for bulk diamond match the values obtained previously by Nava et al. [61] and, as expected, are higher than those for the polycrystalline material. At the lowest field of 2 kV/cm, the simulation results predict a drift velocity reduction of about 20 per cent for polycrystalline material. However, this difference in the drift velocity is seen to reduce with increasing electric field. This behavior is due to reductions in grain boundary scattering with an increase in the quasi-particle momentum. Beyond 70 kV/cm, there does not appear to be any significant speed disadvantage for the synthetic diamond material.

Monte Carlo predictions of the temperature dependent velocity behavior are presented in figure 4.19 [62]. A fixed electric field of 10 kV/cm was assumed, again along the <111> direction. As expected, the velocity in the presence of grain boundaries is lower than crystalline diamond material. The difference, however, is larger at the low temperatures and

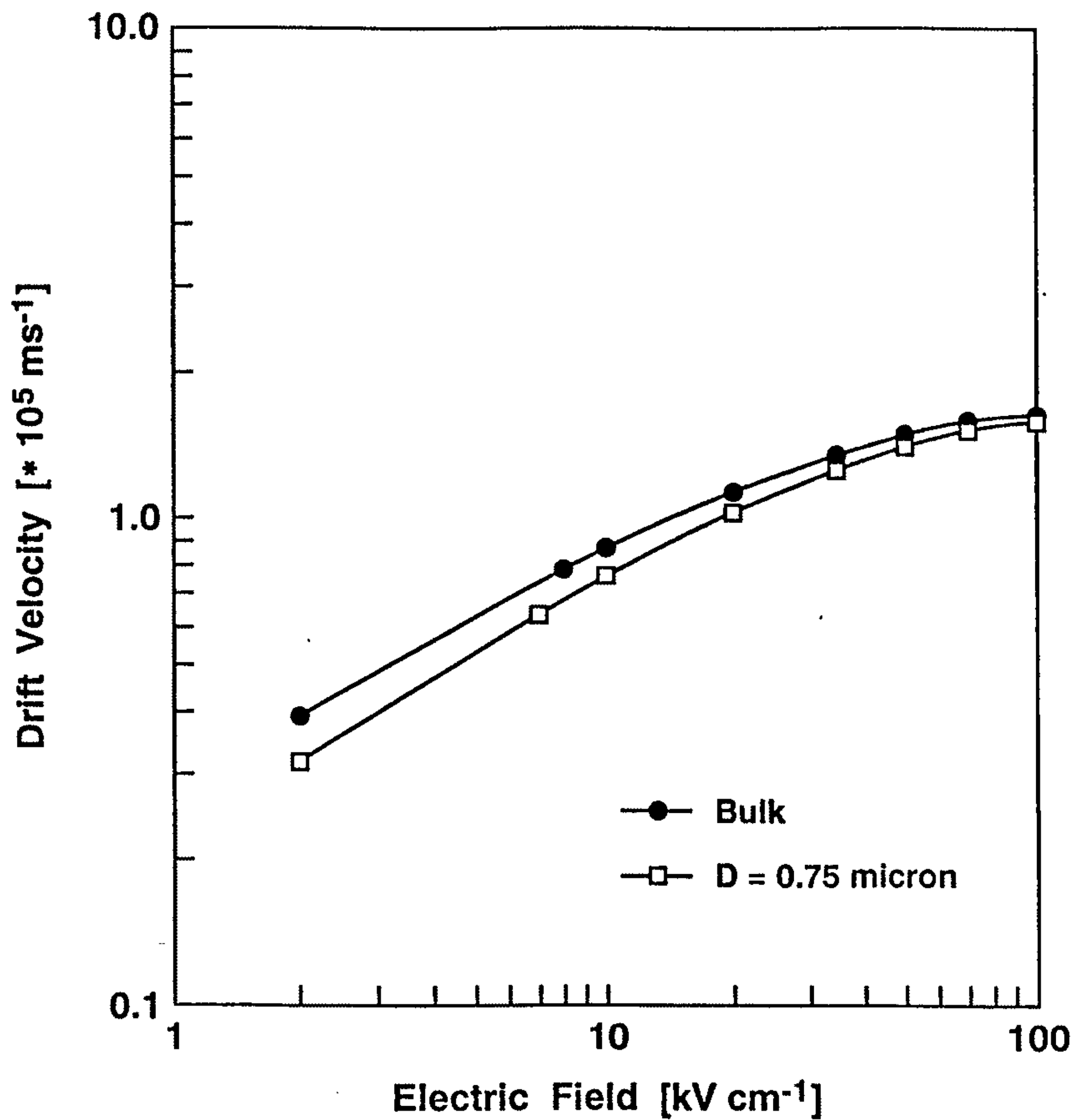

Fig. 4.18 Drift velocity variation with electric field

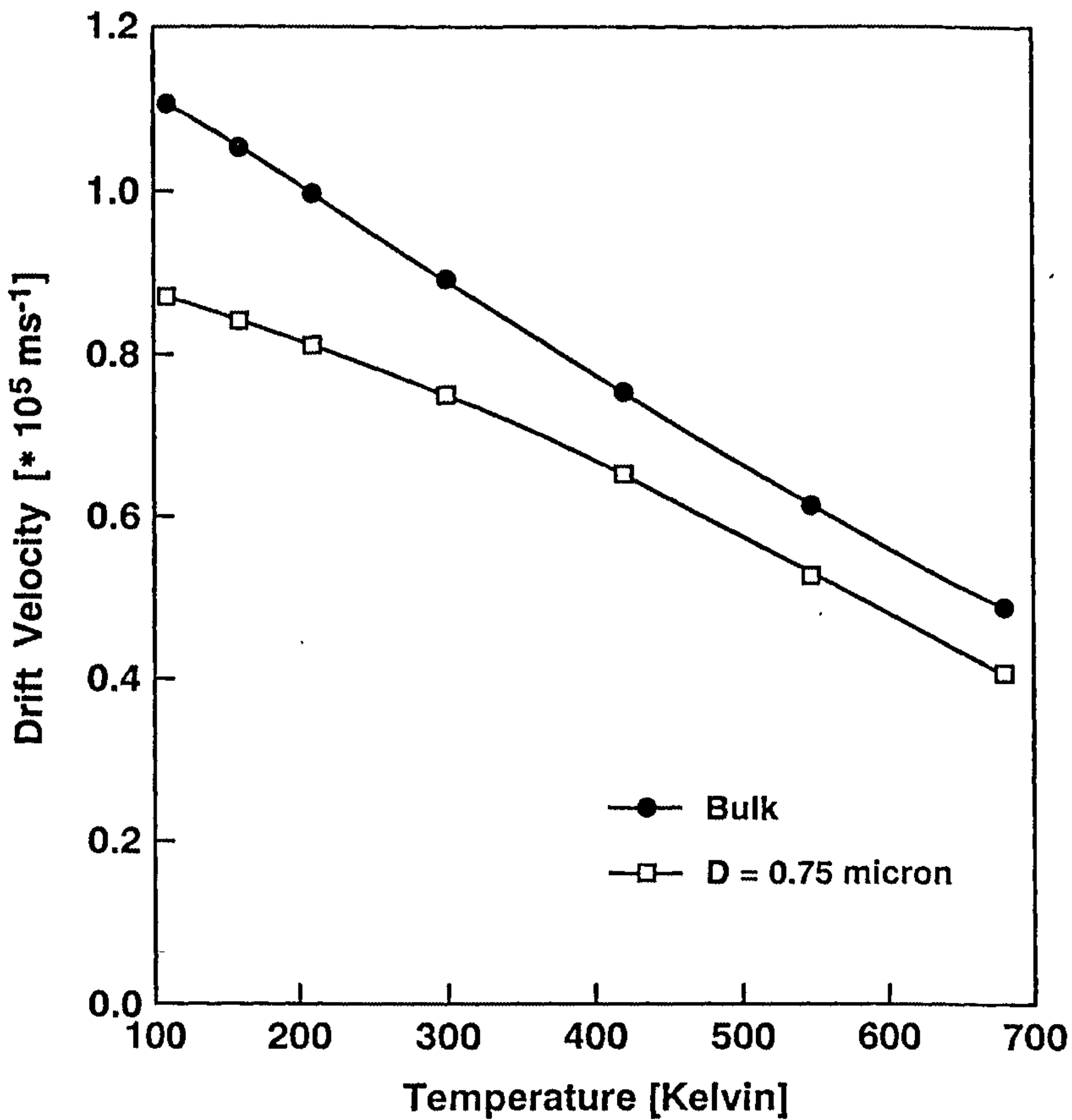

Fig. 4.19 Drift velocity variation with temperature

can be understood is terms of the temperature dependence of the scattering mechanisms. Both acoustic and optical phonon scattering reduce with decreases in the temperature. However, grain boundary scattering is marginally enhanced at the lower temperatures since a colder plasma furnishes a larger percentage of low energy carriers which leads to enhanced scattering. Grain boundary scattering thus begins to dominate over phonon scattering, and control the transport characteristics as the temperature is lowered. As a result, the drift velocities in polycrystalline material, are not expected to exhibit very strong increases with reductions in the temperature. Furthermore, this disparity in the drift velocity between bulk and polycrystalline diamond, is expected to become larger at lower values of the electric field.

Finally, Monte Carlo simulations were performed at 300 K for an electric field of 10 kV/cm along the <111> direction, to probe the transient response. The results of figure 4.20 [62] exhibit the characteristic overshoot behavior in both cases. Though the peak and steady state values are seen to be lowered by the grain boundary scattering, the ratio of these values is marginally enhanced. This is to be expected given that the overshoot phenomena is caused by a disparity in the momentum and energy relaxation rates. Since grain boundary scattering randomizes momentum while conserving energy, the influence of this mechanism works to enhance the overshoot effect. The overshoot ratio is therefore, expected to become more significant with reductions in temperature and a decrease in phonon scattering [62].

4.3.2 SIMULATION RESULTS FOR DIAMOND PHOTOEMISSION

Results obtained for the photoemission from diamond are discussed next. The formulation for polycrystalline diamond was incorporated in the numerical codes. However,

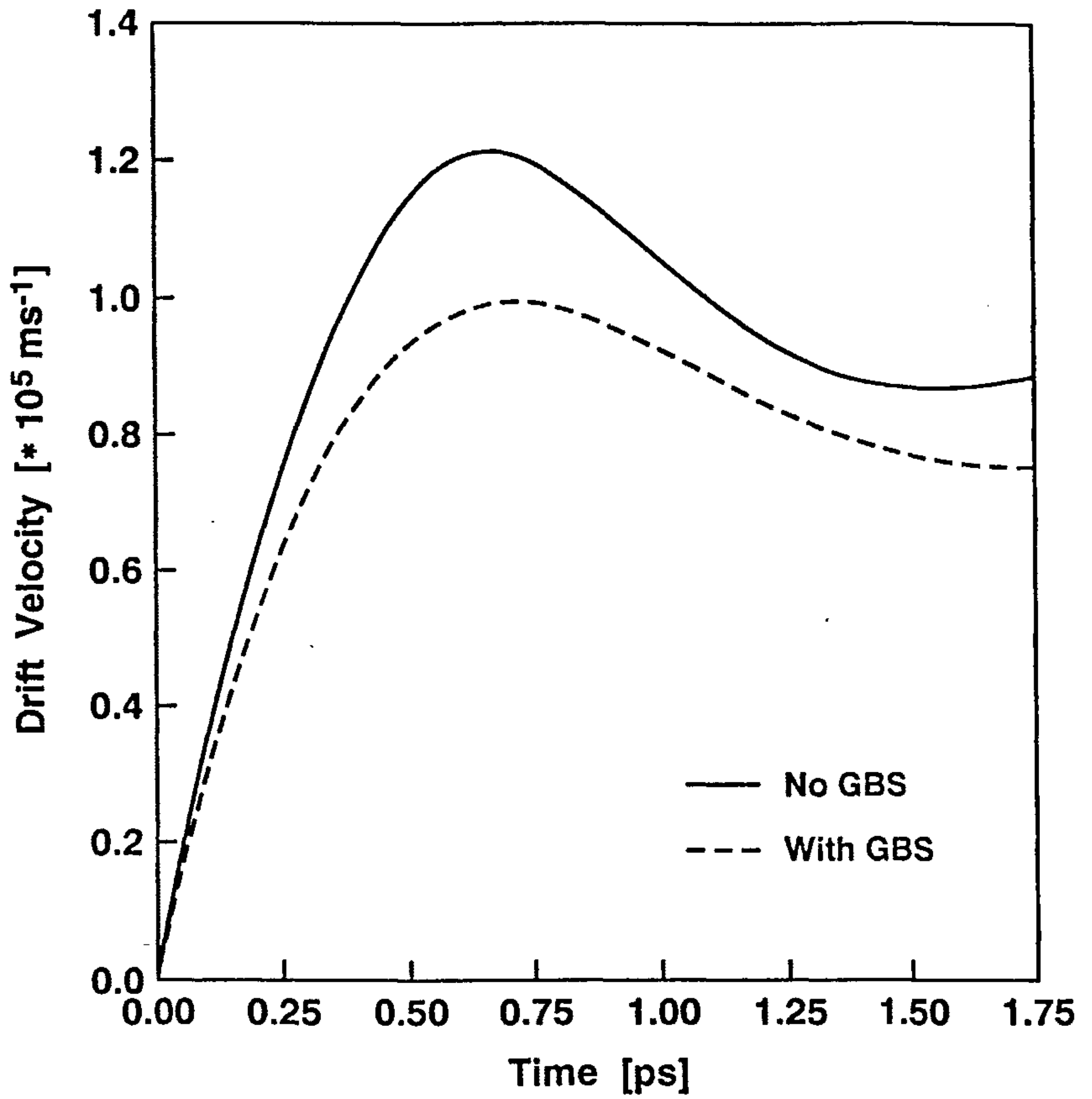

Fig. 4.20 Transient response of drift velocity

before describing the results, a few assumptions regarding the simulations for diamond are presented first for completeness and clarity. (i) The photogeneration of electrons was assumed to be uniform along the z-direction within the sample. This is based on the assumption that photogeneration in the indirect band material occurs via a phonon assisted process. As a result, the absorption rates are likely to be much lower than in GaAs, and the incoming photon flux would have negligible attenuation. (ii) It was also assumed that the photoexcited electrons quickly thermalize to the bottom of the conduction band. The electrons were therefore assigned energies from a Maxwellian distribution at the start of simulation. (iii) The amount of band bending was taken to be the same as that used for GaAs, so that a direct comparison of the results could be done. The simulation was performed for two different values of the energy barrier at the boundary.

As in the case of GaAs, a 0.0-1.0 eV energy range was divided into 40 boxes. The distribution function was obtained by plotting the number of electrons in each box against the energy. Figure 4.21 (a) shows the energy distribution of emitted electrons for a sample thickness of 1μm and doping density of 10^{18} cm^{-3}. Figure 4.21 (b) shows the energy distribution when the doping density is increased to 5 x 10^{18} cm^{-3}. The energy barrier at the emission boundary was taken to be 0.1 eV for both the cases. A number of important features are immediately evident from the plots. (i) First, the number of electrons that emerged from the sample within 10 ps following the initial laser excitation was much lower than GaAs. As a result of the low electron numbers, the statistical variations are quite apparent. (ii) Next, the area under the higher doping curve of figure 4.21 (b) is much lower. This signifies a relative decrease in the electronic emission at the higher density, in keeping with the results obtained previously for GaAs. This results from a smaller depletion length and internal

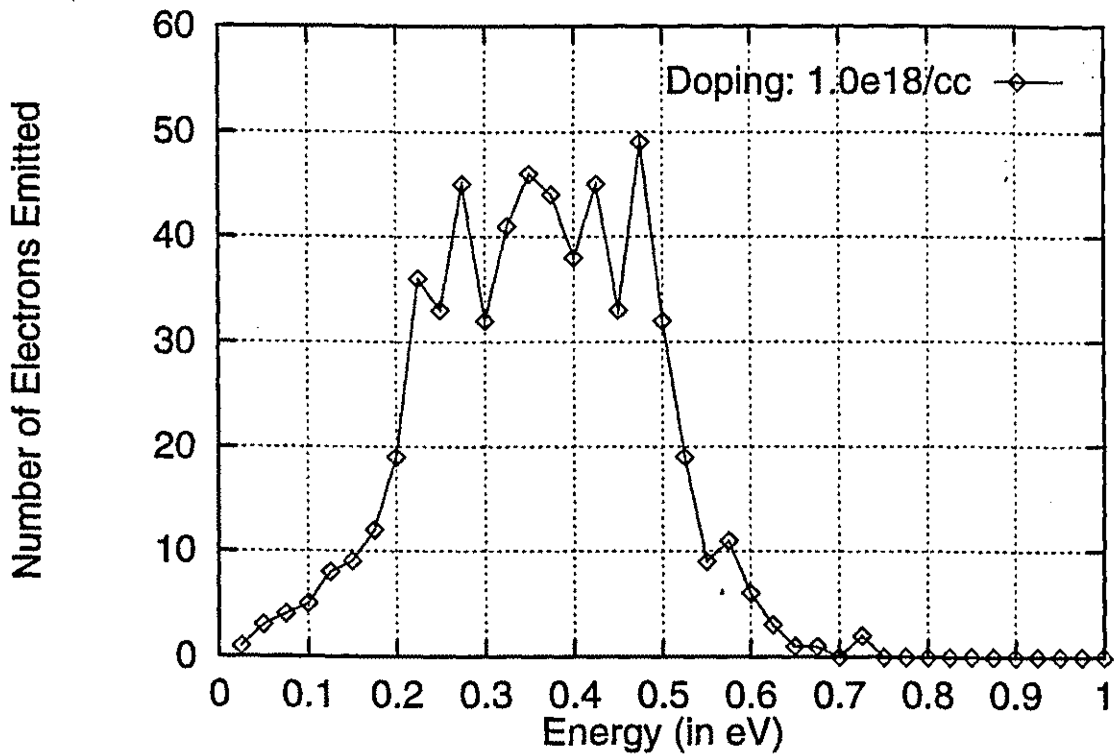

Fig. 4.21(a) ED from diamond for sample thickness of 1 μm and 0.1eV energy barrier

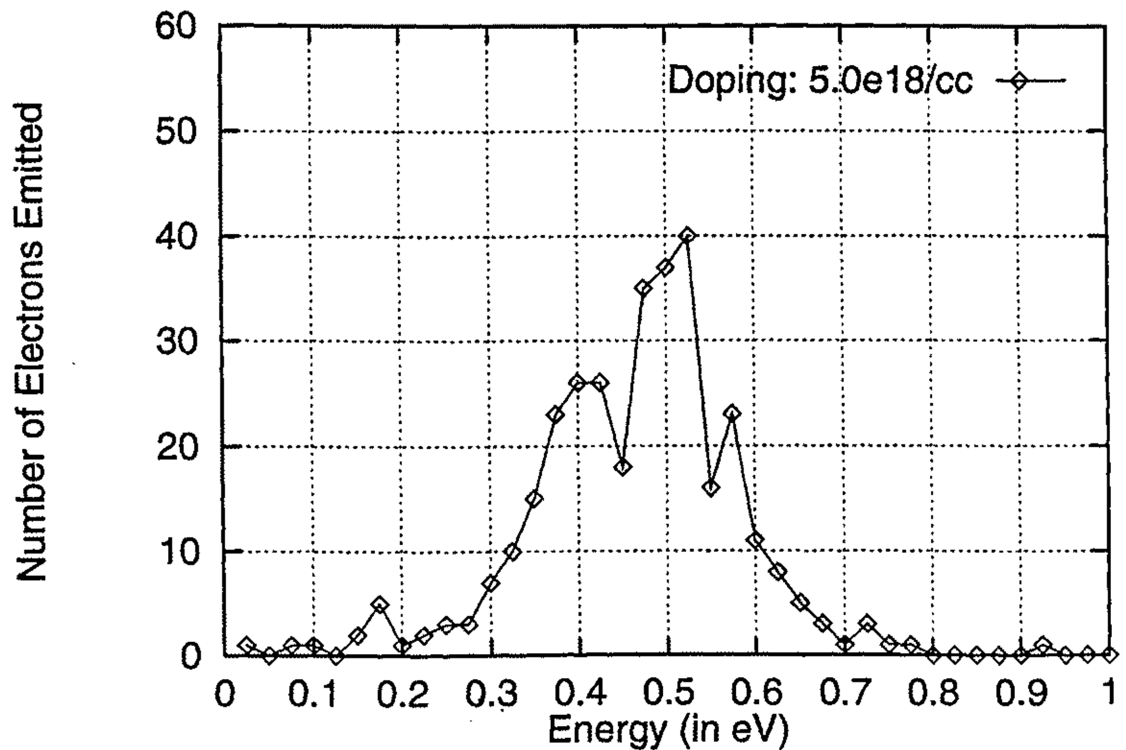

Fig. 4.21(b) ED for sample thickness of 1 μm and 0.1eV energy barrier

space-charge region within diamond at 5 x 10^{18} cm^{-3}. (iii) Finally, there appears to be a much lower spread at the higher doping density of 5 x 10^{18} cm^{-3}. Physically, this occurs due to the smaller electric field region at the higher doping. Due to the smaller penetration, only the photogenerated electrons that are nearest the surface are ejected into the vacuum. This group undergoes relative less scattering since the traversal path is not very long. Consequently, the energy and momentum distributions do not relax very strongly, and are not smeared very much.

A similar behavior resulted from simulations performed at a barrier of 0.0 eV. This situation corresponds to a near NEA situation. Figures 4.22 (a) and (b) show the energy distribution of electrons emitted from diamond within the first 10 ps for doping densities of 10^{18} cm^{-3} and 5 x 10^{3} cm^{3} . As in the previous set of curves, the emission throughput is reduced with doping. The energy spread, however, is seen to be much less at the higher doping. Finally, simulation were also carried out for sample thickness of 5μm. However, the number of electrons emitted were extremely low over a 20 ns time interval. Hence, the simulation results have not been included here. The obvious implication is that moderate to thick diamond films would not be suitable for the photoemission of narrow electron pulses.

The temporal response for energy barrier of 0.1 eV and doping densities of $1.0\times10^{18}/\text{cm}^3$ and $5.0\times10^{18}/\text{cm}^3$ have been shown in figures 4.23 (a) and (b), respectively over a 10 ps time interval. The corresponding results for a zero energy barrier have been shown in figures 4.24 (a) and (b). The plots quantitatively confirm the low rate of emission from diamond, and reveal a long "tail" in the temporal response. The occurrence of a tail suggests that diamond would not be suited for producing short electron pulses. The

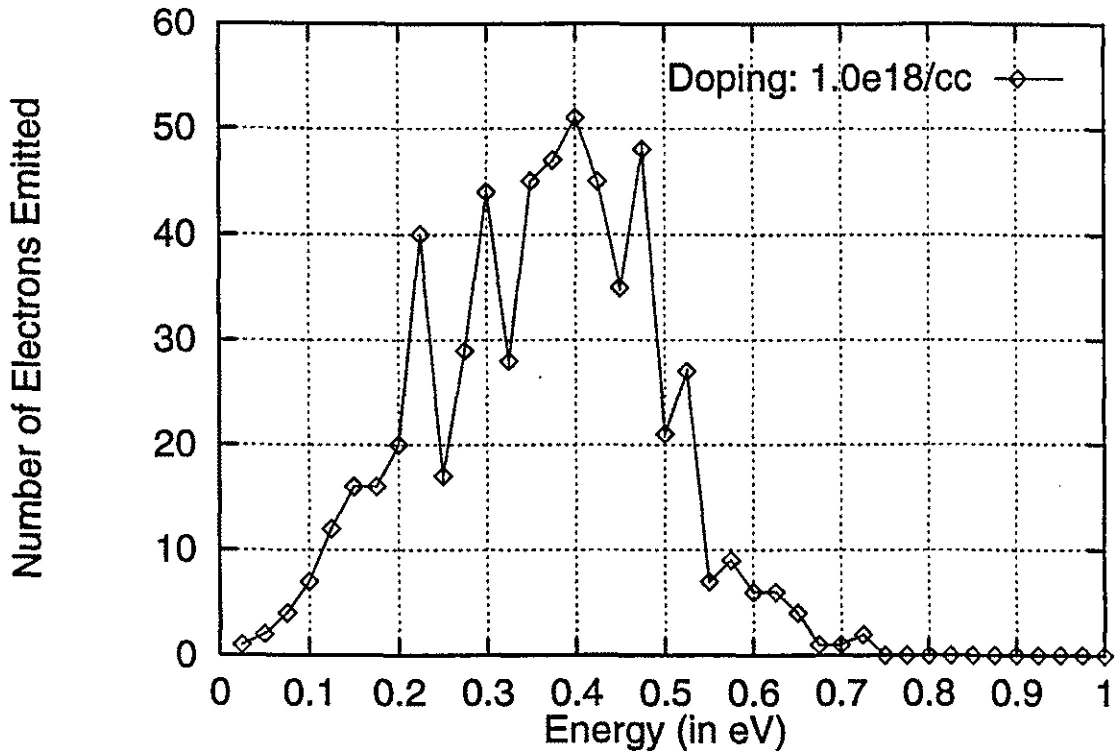

Fig. 4.22(a) ED for sample thickness of 1 μm and zero energy barrier

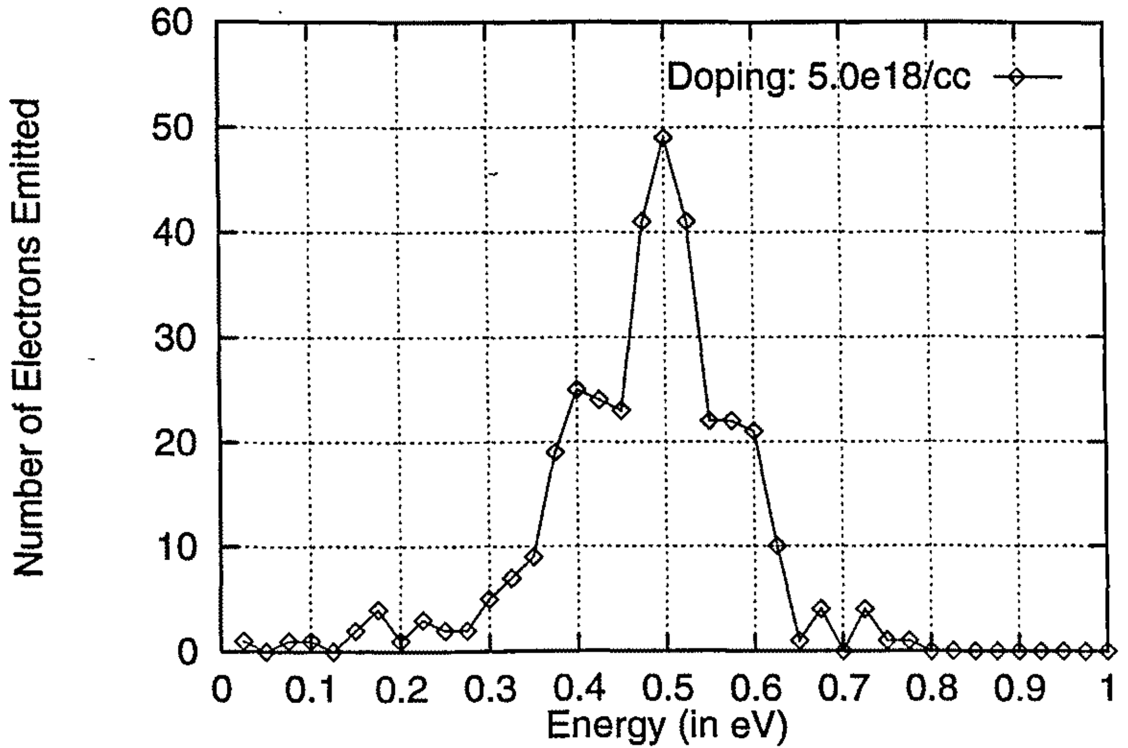

Fig. 4.22(b) ED for sample thickness of 1 μm and zero energy barrier

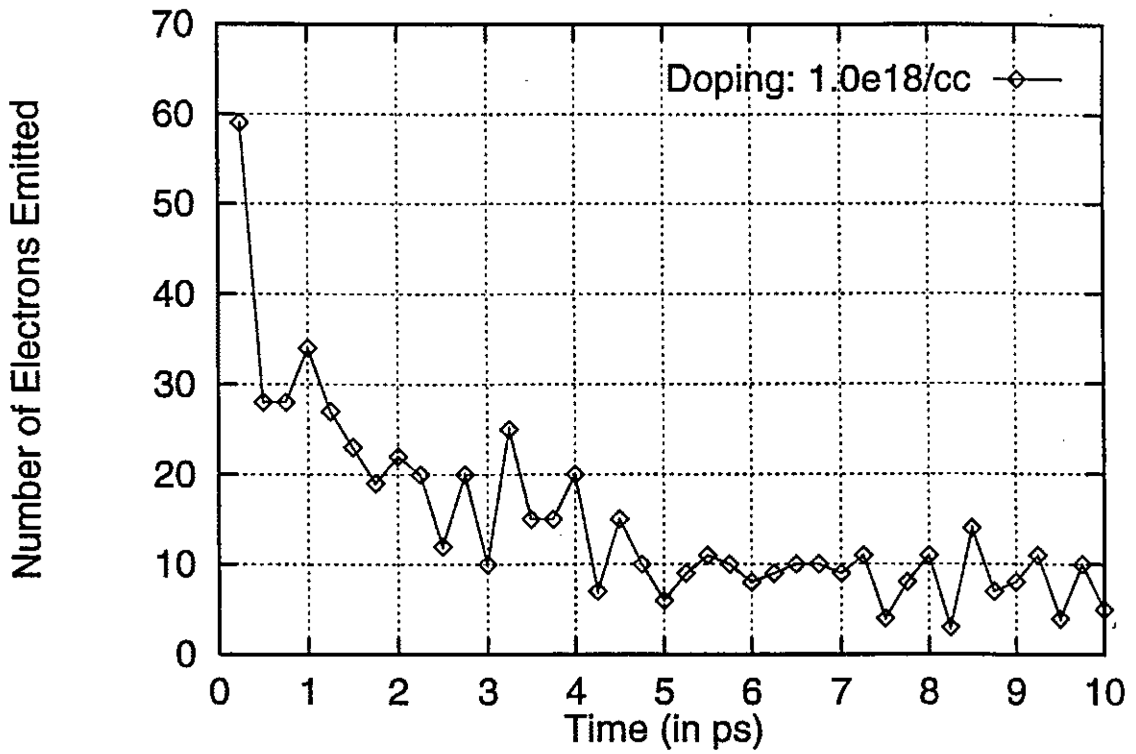

Fig. 4.23(a) Temporal response (TR) for energy barrier of 0.1 eV

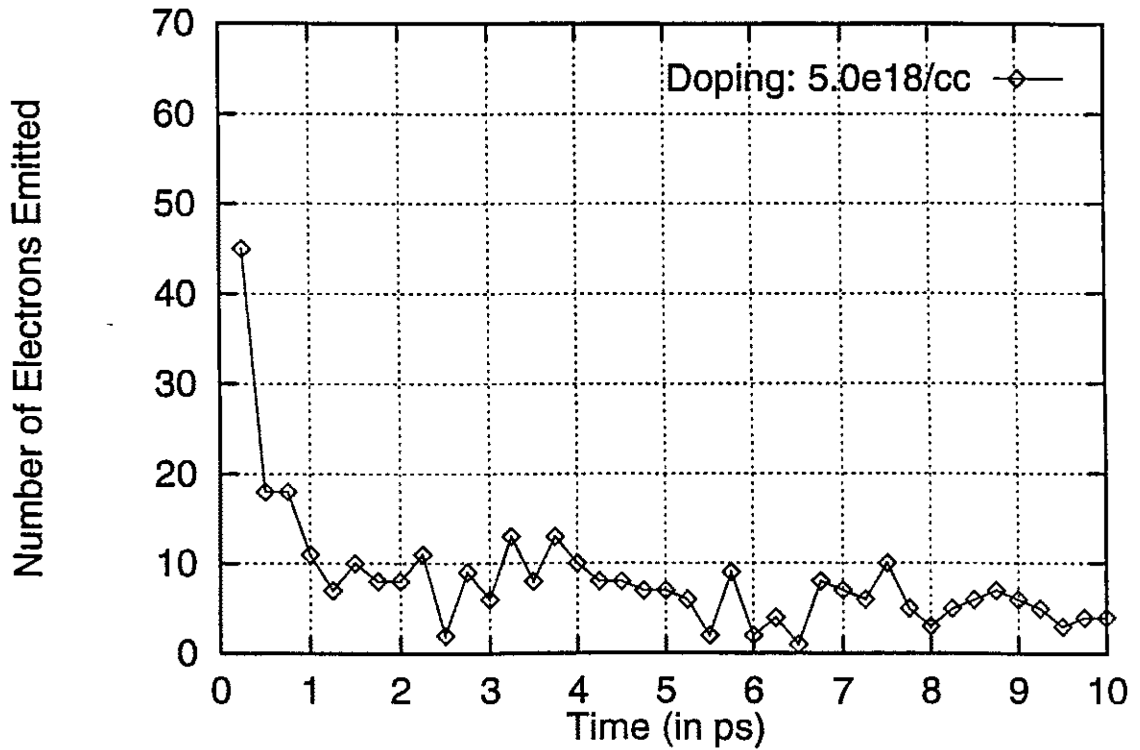

Fig. 4.23(b) TR for energy barrier of 0.1 eV

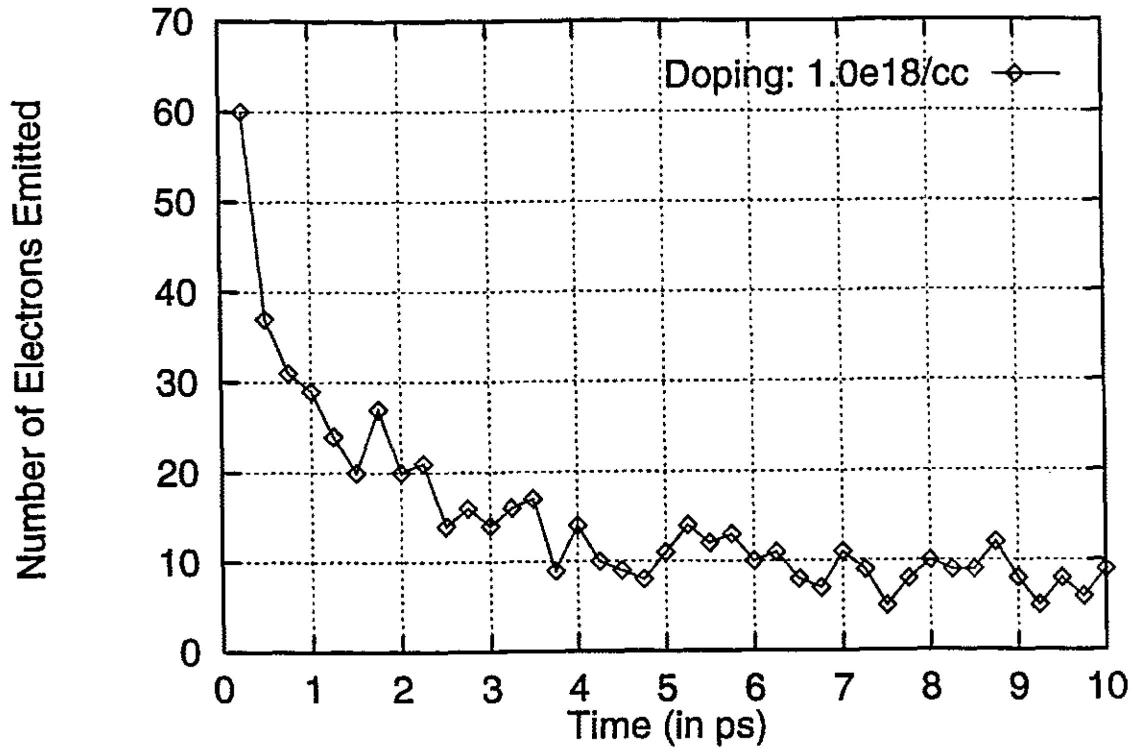

Fig. 4.24(a) TR for zero energy barrier

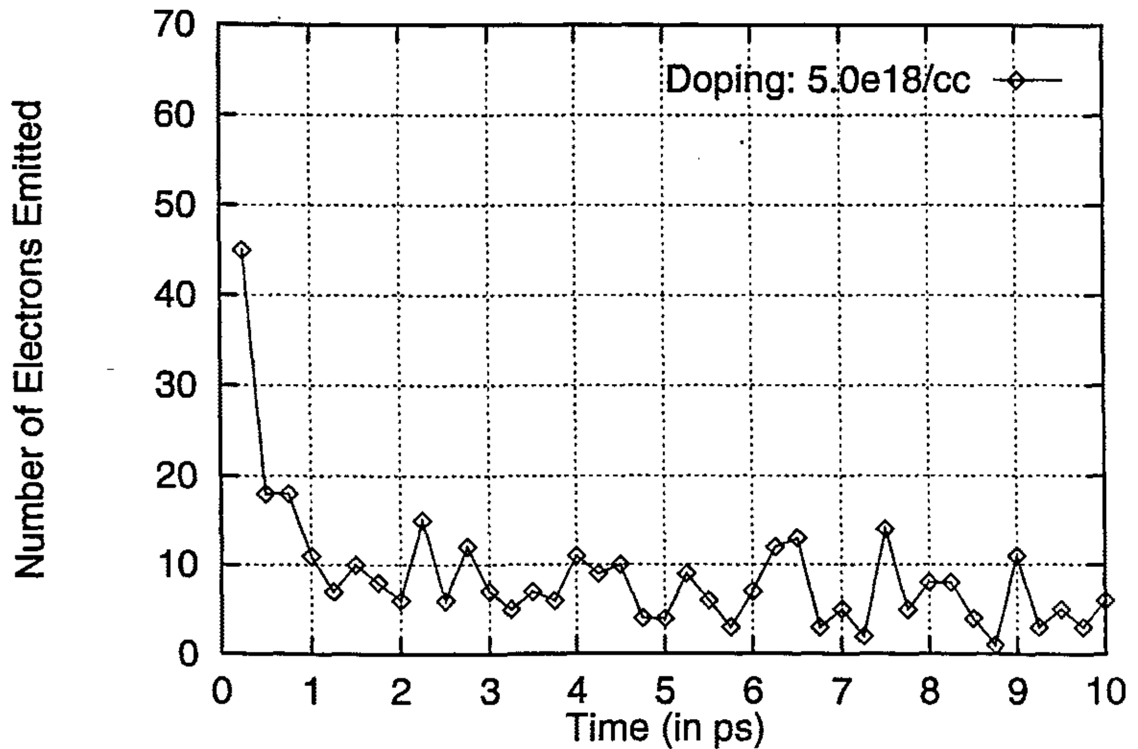

Fig. 4.24(b) TR for zero energy barrier

presence of the "tail" is partially due to the long absorption length which produces throughout the material. In the absence of an external field, the mechanism of carrier transport and subsequent emission is quite low. Furthermore, the occurrence of indirect conduction band minima, work to dramatically reduce the probability of emission into the vacuum. For example, unlike GaAs, four of the six equivalent valleys would have large values of transverse momentum associated with the electrons. This aspect has been discussed in detail in the appendix. The emission coefficient for these four valleys is therefore very low, and arises from the requirement of conserving transverse momentum during a tunnelling process. The overall effect is a reduction in the electronic throughput in diamond. The same pattern is expected for all indirect band semiconductors.

4.4 DISCUSSION AND RESULT SUMMARY

Results for the Cesium coated GaAs were compared with available experimental data. There was very good agreement between simulation results and experimental data on the energy distribution of emitted electrons. This confirmed the validity of the Monte Carlo model and simulation scheme used here.

The salient features obtained from the present simulations for GaAs can be summarized as follows: (i) The spread (FWHM) in the electron kinetic energies for 1.55 eV and 2.1 eV photoexcitation was roughly 150 meV in the reflective mode. (ii) The peak kinetic energies of the out-coming electrons were approximately at 0.55 eV. (iii) The electron energy distribution broadened slightly and the peak decreased by about 20 % as the p-doping in the GaAs was increased from 10^{18} cm^{-3} to 5 x 10^{18} cm^{3}. This was a result of increased impurity scattering. Increasing the "effective NEA" through enhanced doping therefore is

detrimental if a sharp mono-energetic beam is required. (iv) The temporal response to a fast (100 ps laser pulse) in the reflective mode had a two-component characteristics. An initial rapid emission burst over the first 2-3 ps, was followed by a long "tail" lasting well beyond 15 ps. The tail is due to "quasi-thermalized" electrons, while the initial burst corresponds to near-ballistic transport of carrier generated near the surface. (v) Due to internal scattering and the requirement of conserving momentum parallel to the surface, the emitted electrons did not emerge exactly in a perpendicular direction. Instead, there was a small 10 degree spread of the beam. (vi) In the "transmission mode" of operation the Cesium-GaAs system showed a much longer lived temporal response and had a strong dependence on the sample thickness. For example, emission was almost negligible over the first 30 ps for GaAs thicknesses exceeding 15 μm. This is expected since most of the carrier generation occurs near the non-emitting surface. (vii) Finally, increasing the doping density resulted in a reduced electronic throughput, for both the reflective and transmission modes. This was the result of a smaller electric field region near the surface, which reduced the fraction of photogenerated carriers that could be swept out.

Simulation results for diamond revealed the emission flux to be substantially lower than in GaAs. This clearly suggests that diamond is a poor candidate for applications requiring the production of short electron pulses. The reduced electronic emission and throughput was primarily due to the low transmission probability at the surface and the energy-independent long absorption lengths. Physically, the former effect is linked to the indirect nature of the bandgap which constraints the electrons to occupy the six equivalent minimas along the [100] direction. As a result, a large transverse momentum component is associated with electrons that are incident at the surface. Since transverse momentum has to

be conserved, this leads to a high probability of evanescent electron modes. The [100] surface is clearly the best candidate for emission, since two of the six valleys then have a low transverse component. However, the work function for this surface is not as low as that of the [111].

CHAPTER 5

CONCLUSIONS

5.1 RESEARCH SUMMARY

Monte Carlo based numerical simulations were carried out to study photoemission from GaAs and diamond. The central goal was to assess the potential for NEA photoemission from diamond, and to predict its characteristics. To facilitate meaningful comparisons, similar simulations were carried out for both diamond and Cesium-GaAs system. Inclusion of the GaAs system had a two-fold purpose: (i) The calibration and validation of the present simulations by comparing the predictions with experimental data that is readily available for GaAs, and (ii) A comparison of the response characteristics of diamond with the better known GaAs system.

Diamond has been studied as a potential material for NEA photoemission applications because it has a number of well known desirable properties. For example, it can be doped p-type and grown with low trap densities making it a useful semiconductor. The saturation carrier drift velocities are very high. Attributes like hardness, high thermal conductivity, high band gap and radiation hardness can make diamond NEA devices extremely robust and stable. In this thesis, a literature survey was carried out to study the previous research carried out in the field of NEA photoemission from GaAs and diamond. Results of some of the experimental work done in this field were presented and analysed. Earlier simulation work done on GaAs and diamond photoemitter was also studied. Shortcomings of the previous simulation studies were identified and a more comprehensive model developed for the current calculations.

The simulation of photoemission was carried out using the Monte Carlo technique. The usual three-step model was used as the basis for simulating the overall photo-emission process. This model includes: (i) Initial generation of carrier in phase-space, (ii) subsequent transport which results in energy and momentum redistribution, towards the emitting surface, and (iii) the eventual quantum mechanical emission at the surface itself. The Beer-Lampert law was used with appropriate wavelength-dependent absorption coefficients for the initial generation process. The incident photon flux was assumed to be unpolarized. Monte Carlo procedures were used for the transport which included all the relevant scattering mechanisms and details of the electronic band-structure. Though transport calculations for GaAs are quite straightforward and well known, the treatment for diamond is less clear. For example, it is very difficult to grow large single-crystal diamond, and the material is known to exhibit internal grain boundaries. Such grain boundaries are known to decrease the carrier mobility by creating internal localized potential barriers, and may lead to the formation of internal trapping centers. This effect of grain boundaries was therefore included in the calculations of transport in diamond through a statistical scattering formulation. Finally, the energy dependent coefficients for quantum mechanical reflection at the emitting surface were calculated based on a solution of the Schrodinger wave equation in the effective mass approximation. In case of GaAs, an energy barrier at the boundary due to the Cesium layer was assumed. For diamond, Airy functions were used as the basis for the electron waves, and image lowering effects were ignored. However, the formulation included satellite valley occupancy and the effect of a large momentum associated with carriers occupying indirect minimas.

Monte Carlo simulations were performed to study the energy distribution, temporal response and angular distribution of the emitted electrons. Effects of various parameters, like sample doping, sample thickness, pulse width and excitation energy on the characteristics of the emitted electron beam were simulated. The results for Cesium coated GaAs were in good agreement with the available experimental data. The energy distribution showed marked changes with variations in sample doping and thickness. Decrease in the peak energy distribution with increase in doping was due to increased impurity scattering. The effect was more pronounced in transmission mode since the electrons were generated close to the non-emitting surface, and had to travel a longer way to reach the emission boundary, resulting in more momentum randomization. Increase in sample width also caused the electrons to travel a longer distance to reach the emission surface, thereby reducing the number of emitted particles and the peak energy distribution. The peak kinetic energies of the emitted electrons was approximately 0.55 eV and the spread (FWHM) in energies was roughly 150 meV. These results were found to be in excellent agreement with experimental results obtained previously.

The temporal response also showed similar variation with sample doping and thickness. An increase in doping lead to a slower response of the photoemitter. This resulted from two factors. First, increased impurity scattering reduced the "streaming flow" and leading to lower flux of electrons incident on the emitting surface during a given time interval. Secondly, increased doping also reduced the width of the band-bending region, leading to lower fraction of electrons that could experience an electric field and be swept towards the emitting surface. Increased device thickness caused electrons to travel a longer distance, taking them longer to get emitted. This was seen to make the temporal response

"slower". For transmission mode, the emission became negligible as the thickness is increased beyond 5 μm. Higher pulse energies led to larger electronic emission. This was related to an energy (and wavelength) dependent decrease in the characteristic absorption coefficient. At higher energies the photogenerated electrons were generated closer to the surface, forcing a larger percentage of the population to be swept towards the surface by the internal electric field. The temporal response in most of the cases consisted of initial rapid emission burst over the first 2-3 ps, followed by a long "tail" lasting well over 10 ps due to the quasi-thermalized electrons. The angular distribution showed a spread of 10° in the beam, because of internal scattering and requirement of conserving momentum parallel to the surface while crossing the boundary.

The emission flux in case of diamond was found to be substantially lower than in GaAs. Increase in doping led to small decrease in the number of electrons emitted. This was due to reductions in the thickness of the band-bending region. Decreasing barrier at the sample-vacuum boundary caused only a marginal enhancement in electronic emission due to improved transmission probability at the boundary. The temporal response showed a long tail extending well beyond 10 ps due to the quasi-thermalized electrons.

The simulation results suggest that diamond will be a poor candidate for applications requiring the production of short electron pulses. The reduced electronic emission and throughput would primarily be due to the low transmission probability at the surface. The indirect nature of the bandgap in diamond constraints the electrons to occupy the six equivalent minimas along the [100] direction. This results in a large transverse momentum component associated with electrons. The [100] surface would be the best candidate for emission, since electrons in two of the six valleys would then have a low transverse

component. Only these two valleys would have substantial non-zero transmission probability as described in the Appendix. However, the work function for this surface is not as low as that of the [111]. Furthermore, the absorption coefficient in diamond would have a weak dependence on the incident wavelength. As a result, it would not be possible to tailor the absorption characteristics and produce large photogeneration near the surface for subsequent emission.

Though diamond does not appear to be a suitable material for high-efficiency, ultra-short electron pulse generation based on the present research, it has potential as a field-emitter for producing long pulses. The application of an external electric field would dramatically increase the electronic population that could be driven towards the surface. The electronic emission in such a situation would probably arise by electronic tunneling from the valance band. Such valence band emission has recently been observed in energy resolved experiments on cold-diamond emitters [63]. Some contributions from filled surface states can also be expected. The transmission coefficients for valence band emission, would be much higher given the absence of large transverse momentum components. All the valleys would potentially contribute to emission. Furthermore, the presence of graphitic clusters and internal defects might work to enhance the emission efficiency of the system in the two following ways: (i) First, the clusters would function as a localized source of electrons. (ii) Next, the local fields would be enhanced due to the trapped charge associated with the graphitic clusters. Such field enhancements would drive larger currents.

5.2 SCOPE FOR FUTURE WORK

The basic framework developed in this thesis could be extended and used for a number of other research tasks. Some potential areas of future work are listed below.

(i) Extension of the Monte Carlo simulations to systematically predict and evaluate electron emission from various surface orientations. In the present research, only the [100] surface was used. The [111] and [110] surfaces may be of interest.

(ii) Evaluating the role of grain boundary orientations and physical locations within the diamond film on the output electron characteristics. Specular reflection at grain boundaries close to the surface might change the component of the transverse electron momentum and hence the emission probability.

(iii) Assess the response of biased diamond photoemiters. An externally applied voltage would force a greater electron flux towards the surface leading to higher currents.

(iv) Inclusion of a self-consistent Poisson solver to study both photo- and cold-cathode emission from diamond. The Poisson solver would become important to correctly analyze material containing internal traps and defects which could acquire a net negative charge. The Poisson solver would also be necessary for self-consistent calculations of the internal fields in the presence of high currents. One would expect the material to have a large electron-hole plasma under such a situation.

REFERENCES

1. J. Escher, in *Semiconductors and Semimetals*, edited by R. K. Willardson and A. C. Beer (Academic Press, New York, 1975), Chap. 3.
2. W. E. Spicer, Phys. Rev. **112**, 114 (1958).
3. D. E. Eastman and W. D. Grobman, Phys. Rev. Lett. **28**, 1378 (1972).
4. A. H. Sommer, J. Appl. Phys. **29**, 1568 (1958).
5. N. D. Lang, Phys. Rev. B **4**, 4234 (1971).
6. K. H. Kingdon, Phys. Rev. **24**, 510 (1924).
7. A. A. Turnbull and G. B. Evans, J. Phys. D: Appl. Phys. **2**, 155 (1968).
8. A. H. Sommer, H. H. Whitaker, and B. F. Williams, Appl. Phys. Lett. **17**, 273 (1970).
9. H. Sonnenberg, Appl. Phys. Lett. **14**, 289 (1969).
10. D. G. Fisher, R. E. Enstrom, J. S. Escher, and B. F. Williams, J. Appl. Phys. **43**, 3815 (1972).
11. H. Sonnenberg, IEEE J. Solid-State Circuits **5**, 272 (1970).
12. R. L. Bell and W. E. Spicer, Proc. IEEE **58**, 1788 (1970).
13. B. F. Williams and J. J. Tietjen, Proc IEEE **59**, 1489 (1971).
14. R. U. Martinelli and D. G. Fisher, Proc. IEEE **62**, 1339 (1974).
15. W. E. Spicer, Appl. Phys **12**, 115 (1977).
16. J. A. Burton, Phys. Rev. **72**, 531 A (1947).
17. A. H. Sommer, J. Phys. (Paris) **34**, C6-51 (1974).

18. R. L. Bell, in *Negative Electron Affinity Devices* (Oxford University Press, Clarendon, London, 1974).

19. M. W. Geis, J. C. Angus, Scientific American, 84 (1992).

20. K. Okano, Appl. Phys. A **51**, 1731 (1991).

21. K. Shenai, R. S. Scott, and J. Baliga, IEEE Trans. Elec. Dev. **ED-36**, 1811 (1989).

22. B. V. Spitsyn, L. L. Bouilov, and B. V. Derjaguin, J. Cryst. Growth **52**, 219 (1981).

23. M. Kamo, Y. Sato, S. Matsumoto, and N. Setaka, J. Cryst. Growth **62**, 642 (1983).

24. S. Matsumoto, J. Mater. Sci. Lett. **4**, 600 (1985).

25. W. Zhu, B. R. Stoner, B. E. Williams, and J. T. Glass, Proc. IEEE **79**, 621 (1991).

26. D. M. Malta, J. A. von Windheim, H. A. Wynands, and B. A. Fox, J. Appl. Phys. **77**, 1536 (1995).

27. M. Plano, S. Zhao, C. Gardinier, M. Landstrass, D. Kania, H. Kagan, K. Gan, R. Kass, L. Pan, S. Han, S. Schnetzer, and R. Stone, App. Phys. Lett. **64**, 193 (1994).

28. W. A. Yarbrough and R. Messeir, Science **247**, 688 (1990).

29. L. W. James, R. Eden, J. L. Moll, and W. E. Spicer, Phys. Rev. **174**, 909 (1968); L. W. James and J. L. Moll, Phys. Rev. **183**, 740 (1969).

30. G. Lampel and C. Weisbuch, Solid St. Comm. **16**, 877 (1975).

31. B. Reihl, M. Erbudak, and D. Campbell, Phys. Rev. B **19**, 6358 (1979).

32. C. C. Phillips, A. Hughes, and W. Sibbett, J. Phys. D **17**, 1713 (1984).

33. H. J. Drouhin, C. Hermann, and G. Lampel, Phys. Rev. B **31**, 3859 (1985); H. J. Drouhin, C. Hermann, and G. Lampel, Phys. Rev. B **31**, 3872 (1985).

34. F. J. Himpsel, J. A. Knapp, J. A. VanVechten, and D. E. Eastman, Phys. Rev. B **20,** 624 (1979).

35. M. W. Geis, N. Efremow, J. Woodhouse, M. D. McAleese, M. Marchywka, D. G. Socker, and J. F. Hochedez, IEEE Elec. Dev. Lett. **EDL-12,** 456 (1991).

36. C. Bandis and B. B. Pate, Phys. Rev. B **52,** 12056 (1995).

37. J. S. Escher and H. Schade, J. Appl. Phys. **44,** 5309 (1973).

38. B. Yang, X. Hou, and Y. L. Xu, Phys. Lett. A **142**, 155 (1989); B. Yang and Y. L. Xu, J. Phys. D: Appl. Phys. **23**, 455 (1990).

39. B. Yang, G. Ciullo, V. Guidi, and L. Tecchio, J. Appl. Phys. **25**, 1834 (1992).

40. C. Jacoboni and L. Reggiani, Rev. Mod. Phys. **55**, 645 (1983).

41. E. M. Conwell, Solid State Phys. **9**, (1967).

42. H. G. Reik and H. Risken, Phys. Rev. **126**, 1737 (1962).

43. H. Budd, J. Phys. Soc. Japan **21**, 420 (1966).

44. T. Kurosawa, J. Phys. Soc. Japan **21**, 424 (1966).

45. W. Fawcett, in *Electron in Crystalline Solids* (International Atomic Energy Agency, Vienna, 1973).

46. A. D. Broadman, in *Physics Programs*, edited by A. D. Broadman (Wiley, New York, 1980).

47. A. D. Broadman, W. Fawcett, and H. D. Rees, Solid State Commun. **6**, 305 (1968), Chap. 11.

48. W. Fawcett, A. D. Broadman, and S. Swain, J. Phys. Chem. Sol. **31**, 1963 (1970).

49. G. L. Bir and G. E. Pikus, in *Symmetry and Strain-Induced Effects in Semiconductors*, edited by D. Louvish (Wiley, New York, 1974).

50. B. K. Ridley, in *Quantum Processes in Semiconductors* (Oxford University Press, 1982).

51. E. M. Conwell and V. F. Weisskopf, Phys. Rev. **77**, 388 (1950).

52. H. Brooks and C. Herring, Phys. Rev. **83**, 879 (1951).

53. L. S. Pan, D. Kania, S. Han, J. W. Ager III, M. Landstrass, O. Landen, and P. Pianetta, Science **255**, 830 (1992).

54. L. L. Kazmerski, in *Polycrystalline and Amorphous Thin Films and Devices*, edited by L. L. Kazmerski (Academic Press, New York, 1980), Chap. 3.

55. S. Han and R. S. Wagner, Appl. Phys. Lett. **68**, 3016 (1996); S. Han, R. S. Wagner, J. Joseph, M. A. Plano, and M. Moyer, Rev. Sci. Inst. **66**, 5516 (1995).

56. For example, B. A. Fox, B. R. Stoner, D. Malta, P. Ellis, R. C. Glass, and F. R. Sivazlian, Diamd. Related Materials **3**, 382 (1994); D. Malta, J. A. von Windheim, H. A. Wynands, and B. A. Fox, J. Appl. Phys. **77**, 1536 (1995).

57. M. A. Plano, M. Landstrass, L. S. Pan, S. Han, D. Kania, S. McWilliams and J. Ager III, Science **260**, 1310 (1993).

58. I. S. Gradshteyn and I. M. Ryzhik, in *Table of Integrals, Series, and Products*, edited by A. Jeffrey (Academic Press, Orlando, 1980), pg. 40.

59. L. S. Pan, D. Kania, P. Pianetta, J. W. Ager III, M. Landstrass, and S. Han, J. Appl. Phys. **73**, 2888 (1993).

60. N. Fujimori, H. Nakahata, and T. Imai, Jpn. J. Appl. Phys. **29**, 824 (1990).

61. F. Nava, C. Canali, C. Jacoboni, L. Reggiani, and S. Kozlov, Solid St. Comm. **33**, 475 (1980); L. Reggiani, S. Bosi, C. Canali, F. Nava, and S. Kozlov, Phys. Rev. B **23**, 3050 (1981).

62. R. P. Joshi and A. Srivastava, Appl. Phys. Lett., to appear Sept. 1996.

63. C. Bandis and B. B. Pate, Appl. Phys. Lett. **69**, 366 (1996).

APPENDIX A

TRANSMISSION OF ELECTRONS AT THE SURFACE

This appendix contains a quantum mechanical treatment of the problem of transmission of electrons at the sample surface. The transmission probability is calculated using electron wave functions across the boundary region based on the effective mass approximation.

A.1 DIRECT BAND GaAs MATERIAL

Consider the electron wave functions in the three regions - GaAs (region 1), Cs layer (region 2) and vacuum (region 3):

$$\Psi_1 = \left[Ae^{i\alpha z} + Be^{-i\alpha z}\right] e^{i(k_x+K_x)x} . e^{i(k_y+K_y)y} \quad , \qquad \text{(A.1)}$$

$$\Psi_2 = \left[Ce^{ik_2z} + De^{-ik_2z}\right] e^{i(k_x+K_x)x} . e^{i(k_y+K_y)y} \quad , \qquad \text{(A.2)}$$

$$\Psi_1 = \left[Ae^{i\alpha z} + Be^{-i\alpha z}\right] e^{i(k_x+K_x)x} . e^{i(k_y+K_y)y} \quad , \qquad \text{(A.3)}$$

Substituting in the Schrodinger wave equation:

$$-\frac{\hbar^2}{2m_1^*}\nabla^2\Psi + \Delta_v\Psi = E\Psi \quad , \qquad \text{(A.4)}$$

we get:

$$\frac{\hbar^2}{2m_1^*}\left[(k_x+K_x)^2+(k_y+K_y)^2\right]\Psi_1 + \frac{\hbar^2}{2m_1^*}\alpha^2\Psi_1 + \Delta_v\Psi_1 = E\Psi_1 \quad . \tag{A.5}$$

This gives:

$$\alpha = \sqrt{\frac{2m_1^*}{\hbar^2}(E-\Delta_v) - (k_x+K_x)^2 - (k_y+K_y)^2} \quad , \tag{A.6}$$

where $\Delta_v = 0$ for Γ-electrons, $\Delta_v = \Delta E_{\Gamma\text{-}L}$ for L-valley electrons, and $\Delta_v = \Delta E_{\Gamma\text{-}X}$ for X-valley electrons. The effective mass m_1^* equals either m_Γ, m_L or m_X. Similarly,

$$k_2 = \sqrt{\frac{2m_2^*}{\hbar^2}(E-V_0) - (k_x+K_x)^2 - (k_y+K_y)^2} \quad , \tag{A.7}$$

where $m_2^* = m_{Cs}$. Finally,

$$k_3 = \sqrt{\frac{2m_3^*}{\hbar^2}(E-V_B) - (k_x+K_x)^2 - (k_y+K_y)^2} \quad , \tag{A.8}$$

where $m_3^* = m_o$, the free electron mass.

For eventual transmission, $k_3 > 0$ is required. Therefore:

$$E > V_B + \frac{\hbar^2}{2m_3^*}[(k_x+K_x)^2+(k_y+K_y)^2] \quad . \tag{A.9}$$

Also, since α must be real, one obtains the following inequality:

$$E > \Delta_v + \frac{\hbar^2}{2m_1^*}[(k_x+K_x)^2+(k_y+K_y)^2] \quad . \tag{A.10}$$

The A, B, C, D coefficients given above can be evaluate by matching the wavefunction and its derivatives at the boundaries between the three regions. This yields the following set of equations:

$$A + B = C + D \, , \tag{A.11}$$

$$\frac{\alpha}{m_1^*}(A-B) = \frac{k_2}{m_2^*}(C-D) \quad . \tag{A.12}$$

From eqns. (A.11) and (A.12), we get:

$$C = \frac{A}{2}\left(1+\frac{m_2^*}{m_1^*}\frac{\alpha}{k_2}\right)+\frac{B}{2}\left(1-\frac{m_2^*}{m_1^*}\frac{\alpha}{k_2}\right) \quad , \tag{A.13}$$

$$D = \frac{A}{2}\left(1-\frac{m_2^*}{m_1^*}\frac{\alpha}{k_2}\right)+\frac{B}{2}\left(1+\frac{m_2^*}{m_1^*}\frac{\alpha}{k_2}\right) \quad , \tag{A.14}$$

$$Ce^{ik_2L}+De^{-ik_2L} = Ee^{ik_3L} \quad , \tag{A.15}$$

$$\left(\frac{m_3^*}{m_2^*}\frac{k_2}{k_3}\right)\left(Ce^{ik_2L}-De^{-ik_2L}\right) = Ee^{ik_3L} \quad . \tag{A.16}$$

Eliminating "E" from eq.(A.15) and (A.16), and solving for C gives:

$$C = D\left(\frac{1+\frac{m_3^*}{m_2^*}\frac{k_2}{k_3}}{\frac{m_3^*}{m_2^*}\frac{k_2}{k_3}-1}\right)e^{-2ik_2L} \quad . \tag{A.17}$$

Substituting the value of C and D from eq.(A.13) and (A.14) into eq.(A.17), and solving for B gives:

$$B = A\left[\frac{\left(1+\frac{m_2^*}{m_1^*}\frac{\alpha}{k_2}\right)-\left(\frac{\frac{m_3^*}{m_2^*}\frac{k_2}{k_3}+1}{\frac{m_3^*}{m_2^*}\frac{k_2}{k_3}-1}\right)e^{-2ik_2L}\left(1-\frac{m_2^*}{m_1^*}\frac{\alpha}{k_2}\right)}{\left(1+\frac{m_2^*}{m_1^*}\frac{\alpha}{k_2}\right)\left(\frac{\frac{m_3^*}{m_2^*}\frac{k_2}{k_3}+1}{\frac{m_3^*}{m_2^*}\frac{k_2}{k_3}-1}\right)e^{-2ik_2L}+\left(\frac{m_2^*}{m_1^*}\frac{\alpha}{k_2}-1\right)}\right] \quad . \tag{A.18}$$

Eqn. (A.18) can be rewritten as B = A.P for convenience, where "P" is the term within the brackets on the right hand side in eqn. (A.18). From eqn. (A.15), one obtains:

$$E = Ce^{ik_2L}e^{-ik_3L}+De^{-ik_2L}e^{-ik_3L} \quad . \tag{A.19}$$

Value of coefficients "C" and "D" from eqn .(A.13) and (A.14) can then be substituted into eqn. (A.19). This gives an expression for "E" in terms of "A" and "B". Substituting the expression for "B" in terms of "A" from eqn. (A.18), eventually yields "E" in terms of "A" as:

$$E = \frac{e^{-ik_3L}}{2} A \left[\begin{array}{c} e^{ik_2L}\left(1+\frac{m_2^*}{m_1^*}\frac{\alpha}{k_2}\right) + e^{ik_2L}\left(1-\frac{m_2^*}{m_1^*}\frac{\alpha}{k_2}\right)P \\ + \\ e^{-ik_2L}\left(1-\frac{m_2^*}{m_1^*}\frac{\alpha}{k_2}\right) + e^{-ik_2L}\left(1+\frac{m_2^*}{m_1^*}\frac{\alpha}{k_2}\right)P \end{array} \right] . \tag{A.20}$$

Now, the transmission coefficient T can be given by:

$$T = \frac{\frac{1}{m_3^*}\left(\Psi_3^* \frac{\partial \Psi_3}{\partial z} - \Psi_3 \frac{\partial \Psi_3^*}{\partial z}\right)}{\frac{1}{m_1^*}\left(\Psi_1^* \frac{\partial \Psi_1}{\partial z} - \Psi_1 \frac{\partial \Psi_1^*}{\partial z}\right)} = \frac{m_1^* \; k_3}{m_3^* \; \alpha} \frac{|E|^2}{|A|^2} . \tag{A.21}$$

Substituting eqn. (A.20) into eqn.(A.21) yields:

$$T = \left(\frac{m_1^*}{4m_3^*}\frac{k_3}{\alpha}\right) \left| \begin{array}{c} e^{ik_2L}\left(1+\frac{m_2^*}{m_1^*}\frac{\alpha}{k_2}\right) + e^{ik_2L}\left(1-\frac{m_2^*}{m_1^*}\frac{\alpha}{k_2}\right)P \\ + \\ e^{-ik_2L}\left(1-\frac{m_2^*}{m_1^*}\frac{\alpha}{k_2}\right) + e^{-ik_2L}\left(1+\frac{m_2^*}{m_1^*}\frac{\alpha}{k_2}\right)P \end{array} \right|^2 . \tag{A.22}$$

Depending on the valley in which an electron resides, correspondingly appropriate values of K_x, K_y, and K_z need to be used. Thus, for example, $K_x = 0$, $K_y = 0$, $K_z = 0$ for Γ-valley electrons. For X-valley electrons there are three possible pairings: [$K_x = \pm \pi/a$, $K_y = 0$, $K_z = 0$], [$K_x = 0$, $K_y = \pm \pi/a$, $K_z = 0$], and [$K_x = 0$, $K_y = 0$, $K_z = \pm \pi/a$].

Finally, for electrons in the L-valley, the values of $K_{x,y,z}$ would be as: $K_x = K_y = K_z = (3)^{1/2}\, \pi/(3a)$.

A plot of the transmission coefficient versus electron energy has been shown in Fig. A.1 based on the above formulae.

A.2 INDIRECT BAND DIAMOND MATERIAL

Diamond is a near-true NEA material, and does not require a Cs layer on the surface. Hence, in a diamond photoemitter there would be only two regions of interest. Considering the electron wave function inside (region 1) and outside (region 2) the sample in the vicinity of the boundary, one has:

$$\Psi_1 = F(z)\ e^{i(k_x+K_x)x} . e^{i(k_y+K_y)y} \quad , \tag{A.23}$$

$$\Psi_2 = G(z)\ e^{i(k_x+K_x)x} . e^{i(k_y+K_y)y} \quad . \tag{A.24}$$

Substituting eqn. (A.23) into the Schrodinger wave equation in region 1 gives:

$$-\frac{\hbar^2}{2m_x}\frac{\partial^2\Psi_1}{\partial x^2} - \frac{\hbar^2}{2m_y}\frac{\partial^2\Psi_1}{\partial y^2} - \frac{\hbar^2}{2m_z}\frac{\partial^2\Psi_1}{\partial z^2} = E\Psi_1 \quad , \tag{A.25}$$

which can be simplified to:

$$\frac{\hbar^2}{2}\left(F\frac{(k_x+K_x)^2}{m_x} + F\frac{(k_y+K_y)^2}{m_y} - \frac{1}{m_z}\frac{d^2F}{dz^2}\right) = EF \quad . \tag{A.26}$$

This yields a differential equation for F(z) as:

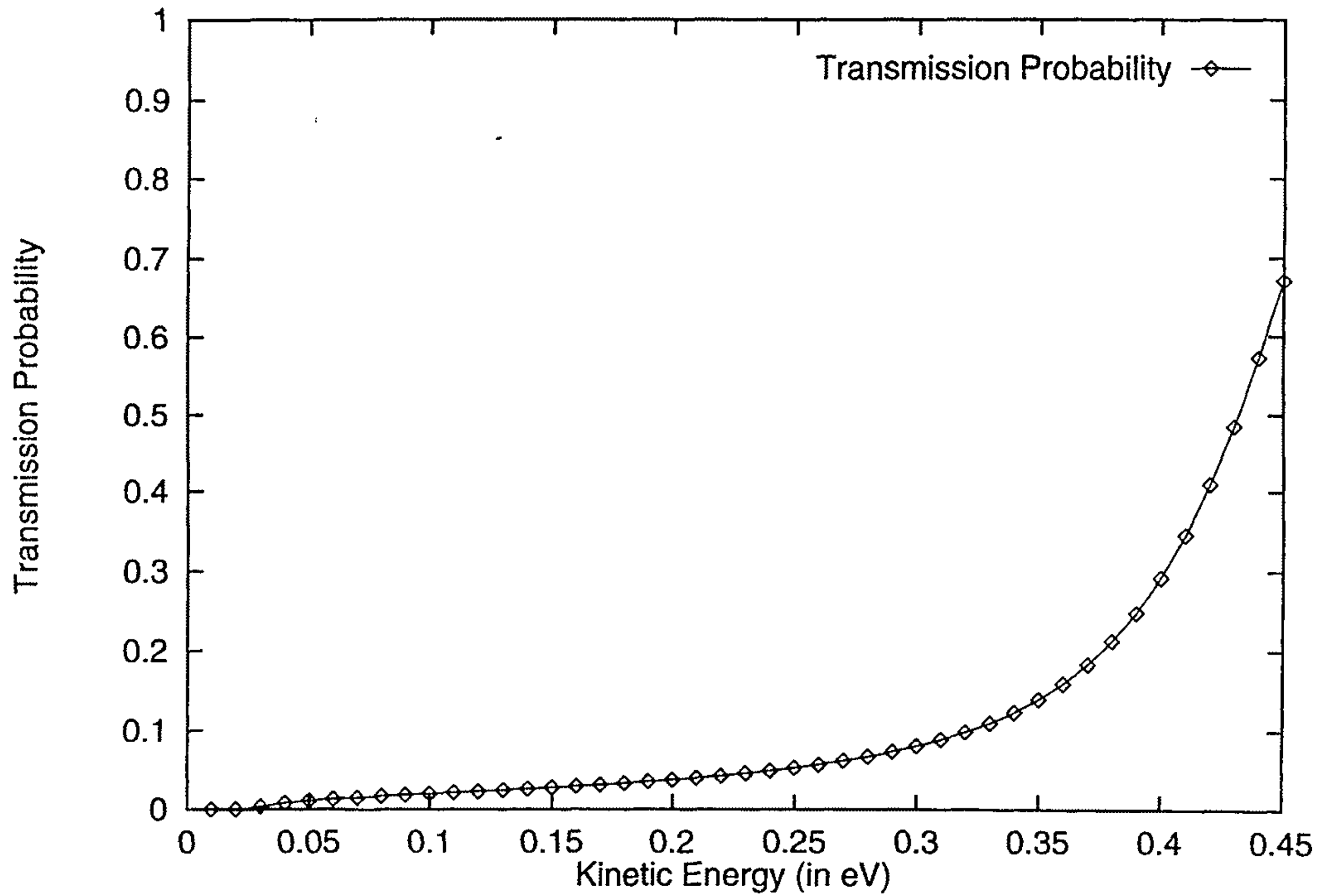

Fig. A.1 Transmission probability as a function of electron energy

$$\frac{d^2F}{dz^2} = -F\left(\frac{2E}{\hbar^2}m_z - \frac{m_z}{m_x}(k_x+K_x)^2 - \frac{m_z}{m_y}(k_y+K_y)^2\right) \quad . \tag{A.27}$$

The solution for F(z) is of the form:

$$F(z) = Ae^{i\alpha z} + Be^{-i\alpha z} \quad , \tag{A.28}$$

where:

$$\alpha = \sqrt{\left(\frac{2E}{\hbar^2}m_z - \frac{m_z}{m_x}(k_x+K_x)^2 - \frac{m_z}{m_y}(k_y+K_y)^2\right)} \quad . \tag{A.29}$$

In region 2, the Schrodinger equation is given by:

$$-\frac{\hbar^2}{2m_0}\frac{\partial^2\Psi_2}{\partial x^2} - \frac{\hbar^2}{2m_0}\frac{\partial^2\Psi_2}{\partial y^2} - \frac{\hbar^2}{2m_0}\frac{\partial^2\Psi_2}{\partial z^2} + (V_0 - qF_z z) = E\Psi_2 \quad , \tag{A.30}$$

where F_z is the uniform field outside the sample boundary. Using (A.24), eqn. (A.30) can be reduced to:

$$\frac{d^2G}{dz^2} = -\left[\frac{2m_0}{\hbar^2}(E - V_0 + qF_z z) - (k_x+K_x)^2 - (k_y+K_y)^2\right] G \quad . \tag{A.31}$$

Let us define ω as:

$$\omega = \frac{\frac{1}{qF_z}\left(\frac{\hbar^2}{2m_0}\left[(k_x+K_y)^2 + (k_y+K_y)^2\right] + (V_0 - E)\right) - z}{\left(\frac{\hbar^2}{2m_0 qF_z}\right)^{\frac{1}{3}}} \tag{A.32}$$

Then eqn. (A.31) becomes:

The solution is given by the Airy functions:

$$\frac{d^2G(\omega)}{d^2\omega} - \omega G(\omega) = 0 \quad . \tag{A.33}$$

$$G(\omega) = C \;[B_i(\omega) + iA_i(\omega)] \quad . \tag{A.34}$$

Matching boundary conditions (wave function and its derivative) at z = 0 gives:

$$A + B = C \;[B_i(\omega_0) + iA_i(\omega_0)] \quad , \tag{A.35}$$

where:

$$\omega_0 = \frac{\frac{1}{qF_z}\left(\frac{\hbar^2}{2m_0}\left[(k_x + K_y)^2 + (k_y + K_y)^2\right] + (V_0 - E)\right)}{\left(\frac{\hbar^2}{2m_0 qF_z}\right)^{\frac{1}{3}}} \quad , \tag{A.36}$$

and

$$\frac{i\alpha}{m_z}(A - B) = -\frac{1}{m_0}\,\frac{C\left[B_i'(\omega_0) + iA_i'(\omega_0)\right]}{\left(\frac{\hbar^2}{2m_0 qF_z}\right)^{\frac{1}{3}}} \quad . \tag{A.37}$$

Solving eqn. (A.35) and eqn. (A.37), we get:

$$\frac{C}{A} = \frac{2i}{iB_i(\omega_0) - A_i(\omega_0) - \frac{m_z}{m_0}\,\frac{\left[B_i'(\omega_0) + iA_i'(\omega_0)\right]}{\alpha\left(\frac{\hbar^2}{2m_0 qF_z}\right)^{\frac{1}{3}}}} \quad . \tag{A.38}$$

Now, the transmission coefficient T is given by:

$$T = \frac{J_{OUT}}{J_{IN}} = \frac{m_z}{m_0}\left|\frac{C}{A}\right|^2 \frac{\left|A_i(\omega_0)B_i'(\omega_0) - A_i'(\omega_0)B_i(\omega_0)\right|}{\alpha\left(\frac{\hbar^2}{2m_0 qF_z}\right)^{\frac{1}{3}}} \quad . \tag{A.39}$$

Using eqn. (A.38) and (A.39), we get:

$$T = \frac{m_z}{m_0} \frac{4\left[A_i(\omega_0)B_i'(\omega_0) - A_i'(\omega_0)B_i(\omega_0)\right]}{\alpha\left(\frac{\hbar^2}{2m_0qF_z}\right)^{\frac{1}{3}}\left|iB_i(\omega_0) - A_i(\omega_0) - \frac{m_z}{m_0}\frac{\left[B_i'(\omega_0) + iA_i'(\omega_0)\right]}{\alpha\left(\frac{\hbar^2}{2m_0qF_z}\right)^{\frac{1}{3}}}\right|^2} \quad \text{(A.40)}$$

In this case, the values of K_x, K_y, and K_z to be used would be as follows :

$K_x = \pm\ \pi/a$, $K_y = 0$, $K_z = 0$ for the two equivalent [100] directions; $K_x = 0$, $K_y = \pm\ \pi/a$, $K_z = 0$ for the [010] directions, and $K_x = 0$, $K_y = 0$, $K_z = \pm\ \pi/a$ for the [001] directions.

DATE DUE

MAY 1 0 2002

MAY 1 1 2004

JAN 2 0

HIGHSMITH #45230

Printed in USA